LBL-23570 c.2

Lawrence Berkeley Laboratory
UNIVERSITY OF CALIFORNIA

RECEIVED
LIBRARY
JUL 14 1987
LIBRARY AND
DOCUMENTS SECTION

PROBING THE DIRECT STEP OF RELATIVISTIC HEAVY ION FRAGMENTATION–(^{12}C,^{11}B+p) AT 2.1 GeV/NUCLEON WITH C AND CH_2 TARGETS

M.L. Webb
(Ph.D. Thesis)

June 1987

TWO-WEEK LOAN COPY
This is a Library Circulating Copy which may be borrowed for two weeks.

NUCLEAR SCIENCE DIVISION

LBL-23570 c.2

Prepared for the U.S. Department of Energy under Contract DE-AC03-76SF00098

DISCLAIMER

This document was prepared as an account of work sponsored by the United States Government. While this document is believed to contain correct information, neither the United States Government nor any agency thereof, nor the Regents of the University of California, nor any of their employees, makes any warranty, express or implied, or assumes any legal responsibility for the accuracy, completeness, or usefulness of any information, apparatus, product, or process disclosed, or represents that its use would not infringe privately owned rights. Reference herein to any specific commercial product, process, or service by its trade name, trademark, manufacturer, or otherwise, does not necessarily constitute or imply its endorsement, recommendation, or favoring by the United States Government or any agency thereof, or the Regents of the University of California. The views and opinions of authors expressed herein do not necessarily state or reflect those of the United States Government or any agency thereof or the Regents of the University of California.

LBL-23570

Probing the Direct Step of Relativistic Heavy Ion Fragmentation --(^{12}C,^{11}B+p) at 2.1 GeV/Nucleon with C and CH_2 Targets

M.L. Webb

Nuclear Science Division
Lawrence Berkeley Laboratory
University of California
Berkeley, California 94720

June 1987

This work was supported by the Director, Office of Energy Research, Division of Nuclear Physics of the Office of High Energy and Nuclear Physics of the U.S. Department of Energy under Contract DE-AC03-76SF00098.

Contents

List of Tables vi

List of Figures vii

Dedication x

Acknowledgments xi

1 Introduction 1

1.1 History 1

1.2 Motivation 5

1.3 Outline 6

2 Theoretical Models 8

2.1 Overview 8

2.2 Central Collisions 9

2.3 Peripheral Collisions 11

2.3.1 Overview 11

2.3.2 Cugnon Monte Carlo Cascade Code 13

2.4 Grazing Collisions 16

3 Experimental Setup **19**

3.1 The Bevalac 19

3.2 The Magnet 21

3.3 Detector System 24

3.3.1 Beam Definition Scintillators and Start Logic 24

3.3.2 Drift Chambers 28

3.3.3 Time of Flight (TOF) Scintillation Array 31

3.4 Computing Facilities 32

4 Detector Calibration and Resolution **36**

4.1 TOF Array Calibration and Resolution 36

4.2 Drift Chamber Calibration and Resolution 40

4.2.1 Upstream Drift Chambers 40

4.2.2 Downstream Drift Chambers 46

4.3 Overall Position Resolution 55

5 Data Reduction **57**

5.1 Momentum and Mass Reconstruction 57

5.2 Aperture of the HISS Spectrometer 59

6 Data Analysis and Results **63**

6.1 Introduction 63

6.2 Monte Carlo Cascade Model 68

6.3 ^{11}B Inclusive Spectra 71

6.4 Proton Exclusive Spectra 74

6.5 Residual Peak and Inelastic Cross Section 80

7 Conclusion **88**

A Relativistic Kinematics **91**

B Isospin Corrections **96**

Bibliography **99**

List of Tables

3.1 The physical parameters of the HISS dipole. 22

4.1 Event selection criteria for the upstream drift chambers. 42

4.2 Charge $Z = 1$ multiplicity in the TOF wall. 54

5.1 Measured and Computed Quantities. 60

6.1 Monte Carlo cascade model cross section predictions 70

6.2 Comparison of the cascade model and the data in the proton aperture. 78

6.3 Aperture corrected cross section 79

B.1 Isobar model cross sections. 98

List of Figures

1.1 Central collision in emulsion. 2

1.2 Peripheral collision in emulsion. 3

2.1 Hydrodynamic model central collisions. 12

2.2 Possible (^{12}C,^{11}B+p) reaction mechanisms. 17

3.1 The HISS experimental area. 20

3.2 The HISS dipole and vacuum chamber. 23

3.3 The HISS computer system. 25

3.4 Experimental setup. 26

3.5 Event trigger electronics diagram. 27

3.6 Common start electronics. 29

3.7 HISS drift chamber construction diagram. 30

3.8 Time to digital converters (TDC) start electronics. 33

3.9 HISS data acquisition hardware. 34

3.10 Data aquisition software flow chart. 35

4.1 ADC product versus charge for scintillator 16. 38

4.2 Charge distribution in the TOF wall for protons and ^{11}B's. . . . 39

4.3 Timing resolution in the TOF wall for protons and ^{11}B's. 41

4.4 Angular correlation of the beam in the upstream drift chambers. 44

4.5 Effect of the beam collimator. 45

4.6 Drift distance versus TDC channel number for the S plane of $DC1$. 48

4.7 The single cell spatial resolution for beam particles in the S planes of $DC1$. 49

4.8 Response of drift chambers to ^{12}C projectile. 51

5.1 Mass distribution for protons and ^{11}B's. 61

5.2 Experimental aperture. 62

6.1 Excitation energy spectra. 64

6.2 Proton spectra for the H and C targets 65

6.3 Boron spectra for the H and C targets 67

6.4 Boron spectrum from the Monte Carlo cascade model 72

6.5 Proton spectra from the Monte Carlo cascade model 75

6.6 Fit to $-t$ for (a) H and (b) C targets 77

6.7 Proton spectra from the data with the Monte Carlo cascade model subtracted 81

6.8 C(p,p)X cross section 82

6.9 Data cross section versus modified $-t$ for (a) C and (b) H targets. 84

6.10 Perpendicular momenta ^{11}B versus proton for the (a) Nuclear Weiszäcker-Williams model and (b) Carbon target. 86

A.1 Two body scattering. 93

Dedication

I dedicate this manuscript to all those who supported me through this interminable process, and especially to my wife, Laurie Ann. With her fire and determination inspiring me, I could not fail. Thank you all.

Acknowledgments

I thank J. F. Gunion and T. F. Hoang for their insights on diffractive scattering. I also thank J. Alonso and the Bevatron Operations staff for the beam and support services, F. Bieser and I. Flores for the design and fabrication of the detector electronics, and E. Beleal, M. Bronson, and C. McParland for the data handling software. I gratefully acknowledge the many useful discussions with M. E. Baumgartner, H. J. Crawford, J. Engelage, D. E. Greiner, P. J. Lindstrom, D. L. Olson, and J. L. Romero. I thank the Associated Western Universities for their financial support. Finally, I especially thank F. P. Brady for his guidance and support.

This work was supported in part by the Director, Office of Energy Research, Division of Nuclear Physics of the Office of High Energy, and Nuclear Physics of the U. S. Department of Energy under Contracts DE-AC03-76SF00098 and DE-AS05-76ER04699, in part by NSF grant PHY81-21003, and in part by NASA grant NGR-05-003-513.

Chapter 1

Introduction

1.1 History

The study of interactions between nuclei at relativistic energies began in 1948 with the discovery of heavy ions in primary cosmic rays by Freier et al.[1]. In the following years a series of balloon-borne emulsion experiments[2,3,4] mapped out the framework of the process. Two basic concepts emerged: one in space and the other in time.

Spatially, it is possible to classify the collisions as either central or peripheral by impact parameter[3]. In central collisions, the impact parameter is near zero, and the projectile fragments into its constituent nucleons losing considerable forward momentum in the process (Figure 1.1). On the other hand, peripheral collisions are characterized by the maintenance of forward momentum and the presence of large projectile fragments (Figure 1.2). This classification led naturally to the participant-spectator[4] description of peripheral collisions. When

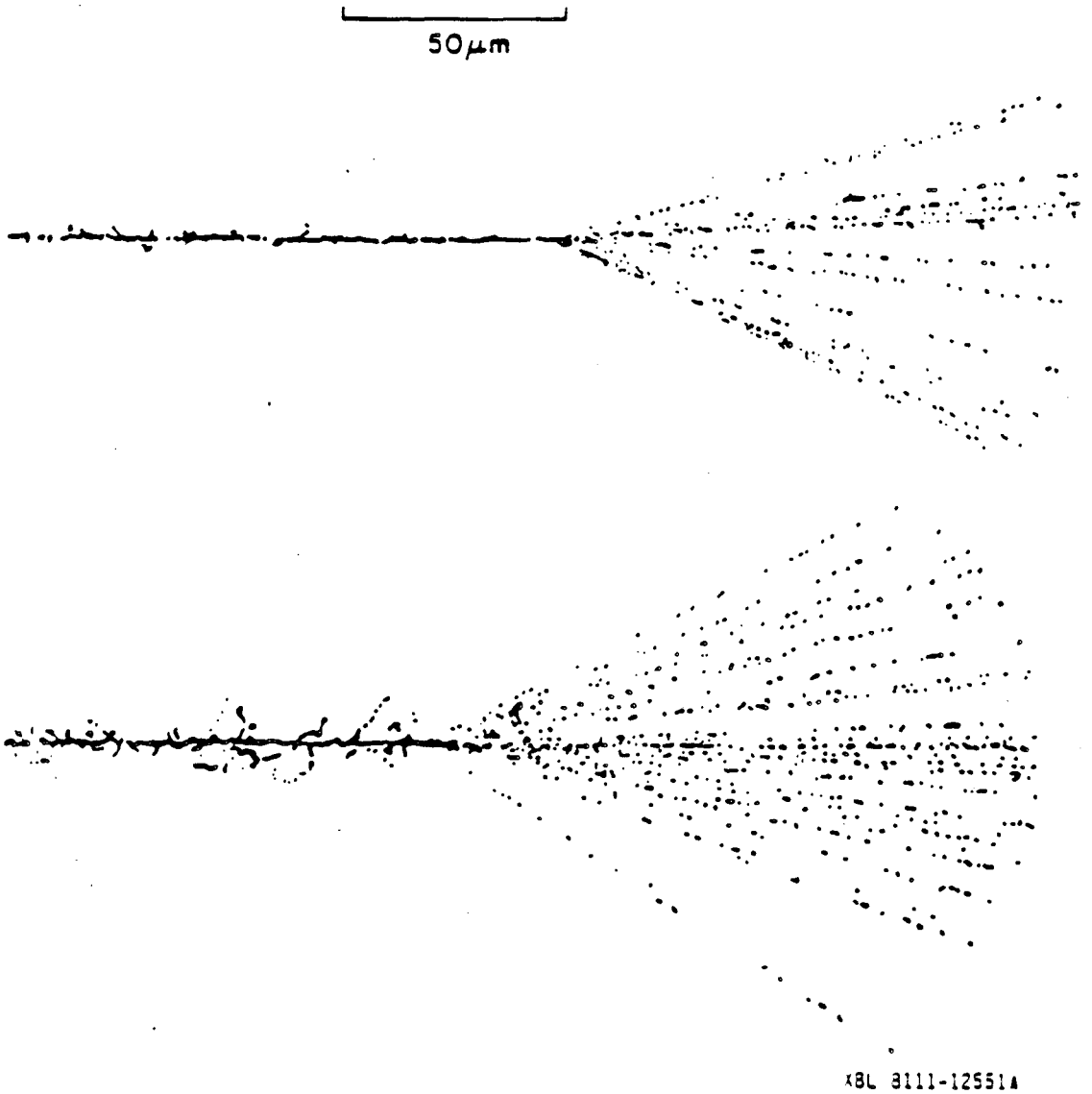

Figure 1.1: Emulsion events with (a) a 2.1 GeV/nucleon ^{14}N producing 15 $Z = 1$ fragments, and (b) a 1.9 GeV/nucleon ^{56}Fe producing one $Z = 2$ and 36 $Z = 1$ fragments[5].

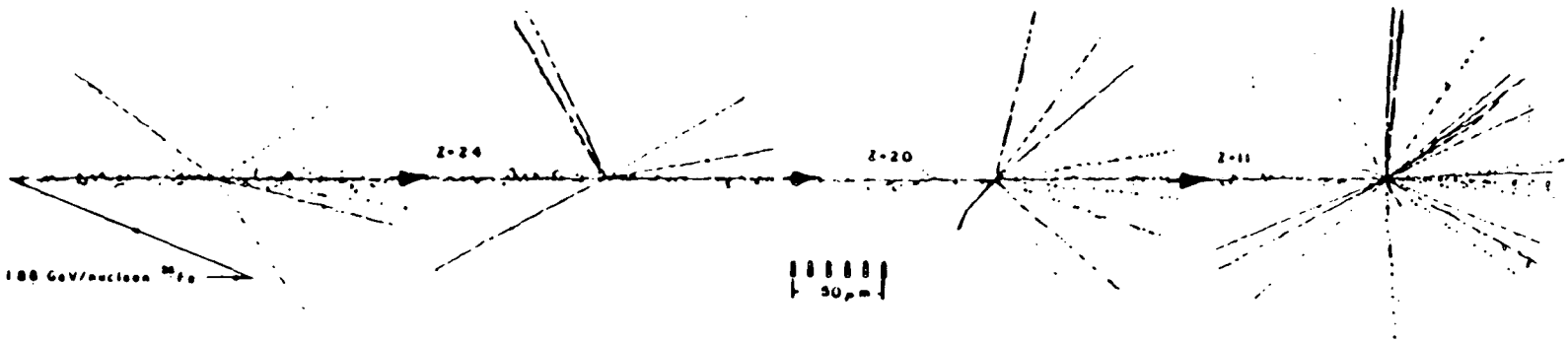

XBL 794-9277

Figure 1.2: A series of four fragmentation reactions initiated by a 1.9 GeV/nucleon ^{56}Fe. In the first three reactions a large fragment persists at 0°[5].

the colliding nuclei interpenetrate, some nucleons in the overlap region scatter; these are the participants. The remaining nucleons comprise the projectile and target spectators.

This separation into participants and spectators brings the temporal concept, abrasion-ablation[6,7], into play. In this prescription, the reaction is a two step process. First the participants are sheared from the nuclei in the abrasion step, a fast process involving direct nucleon-nucleon interactions. This process of abrasion injects some energy into the spectators which then decay by particle emission in the ablation step, a delayed indirect process. The possibility of a grazing collision also exists. In such a collision there is no interpenetration, and thus no individual nucleon-nucleon interactions. The fast direct step, here, is a transfer of energy and momentum between the projectile and target which then later decay by particle emission.

The unpredictable masses and energies of cosmic rays impeded further progress. Mapping out the details of these processes had to wait until the arrival of accelerators capable of delivering heavy nuclei at these energies. In 1970, the synchrophasotron at Dubna accelerated α particles[8], and in 1971 the Princeton Particle Accelerator produced Nitrogen ions[9]. Shortly after, the Bevatron also accelerated Nitrogen ions[10]. Then followed an explosion of experimental results and theory, for which many fine reviews[5,8,11,12] exist.

1.2 Motivation

In relativistic heavy ion collisions there are two types of fragment sources, the participant region and the spectator region, each producing fragments by different mechanisms. In central and near central collisions there are violent interactions in the participant region, while the spectator fragments, if any, receive little energy. The inclusive proton production cross section at large scattering angle is a good measure of this process[13] since protons from the spectators will stay near 0°.

This large angle signal is reduced or absent in peripheral and grazing collisions. Peripheral collisions are characterized by a smaller less violent participant region. Proton scattering at large angles is suppressed, while scattering in the forward direction is enhanced. Protons can also be emitted from a decaying projectile spectator. Grazing collisions have no participant region at all; protons can only come from a decaying projectile. Protons from all sources are predominantly forward peaked, and inclusive measurements[13,14,15,16] cannot adequately distinguish between them, allowing markedly different models[12,17,18,19] to explain the same results. These models will be discussed in detail later (Chapter 2).

We will focus on the direct process in peripheral and grazing collisions to test these models. A simple reaction for studying the direct component of heavy ion fragmentation is ^{12}C fragmenting into ^{11}B+p. There are two possibilities:

(1) the proton is a participant and the ^{11}B is a spectator, or (2) the projectile is collectively excited in a grazing collision and dissociates into a ^{11}B,p pair. This dissociation process has been observed in (^{12}C,3α)[20]. The simplicity of the (^{12}C,^{11}B+p) reaction offers the hope of an unambiguous comparison with the models, and must be understood before more complicated reactions can be attempted with confidence.

To study this reaction one needs a measurement exclusive in projectile fragments. Previous quasi-exclusive measurements of this type have been made with photographic emulsions[21] and streamer chambers[22]. These approaches suffer from poor statistics. They also lack complete particle identification and cannot unambiguously select the reaction of interest.

The data presented here were measured at the Heavy Ion Superconducting Spectrometer (HISS) facility[23] at Lawrence Berkeley Laboratory. The aperture was large enough so that we were able to determine simultaneously the vector momenta of all charged projectile fragments down to zero momentum transfer over a region of phase space containing all the ^{11}B fragments and $72 \pm 19\,\%$ of the protons in the H(^{12}C,^{11}B+p)X reaction.

1.3 Outline

In what follows, we will discuss the applicable models for this reaction (Chapter 2). Then the experimental apparatus necessary for this measurement will

be described (Chapter 3). Next the steps necessary to calibrate the various detectors, and the resolutions obtained will be presented (Chapter 4). Then we elucidate the procedure for converting the detector measurements to usable physical quantities (Chapter 5). These data will then be analyzed, and the implications for the peripheral and grazing collision mechanisms will be pointed out (Chapter 6). Finally, these results will be summarized, and conclusions drawn (Chapter 7).

Chapter 2

Theoretical Models[12]

2.1 Overview

Accompanying the explosion in experimental data since 1970, there has been a similar deluge of theoretical models. The different models emphasize different parts of the reaction mechanism, and thus each is best suited to explaining a particular type of collision, central, peripheral or grazing. Therefore, after discussing features common to all models, we will deal with each type of collision separately.

Nuclear excitations have only a few degrees of freedom at low energies. One sees such things as surface vibrations, rotations, giant resonances, and single particle excitations. For relativistic heavy ion collisions, however, the energy available is so large that it is reasonable to treat the nuclei as a collection of nearly free nucleons. Nuclei are treated as degenerate (non-ideal) gases of particles, and the nucleon-nucleon interaction is paramount.

Due to theoretical difficulties, none of the models are relativistically invariant. Some models do include the Lorentz contraction of the nuclei but the retardation of the potentials involved has not been attempted. It is presumed that these do not alter the qualitative results.

Most models use classical mechanics. The justification used is that the de Broglie wavelength is 0.07 fm at 2.1 GeV/nucleon. However there are areas of low energy motion in these reactions where quantum mechanical effects should be felt, and these are usually dealt with in an approximate way if at all. The strongest of these, the Pauli principle, is usually simulated.

At these energies π production becomes significant. A large proportion of πs come from the decay of nuclear isobars, principally the $\Delta(1232)$ resonance. These are included by assuming free nucleon-nucleon production cross sections.

2.2 Central Collisions

Central collision models are inappropriate for our reaction, since they require a large number of nucleon-nucleon collisions. We include this discussion for the sake of completeness. Since central collisions are characterized by a large number of nucleon-nucleon collisions, the models appropriate for this process incorporate statistical assumptions. The validity of these models hinges on whether equilibration can occur or at least be approached on the time scales of relativistic collisions. The mean free path of a nucleon in static nuclear matter is given by

$\lambda \simeq (\rho\sigma)^{-1}$ where ρ is the density, and σ is the nucleon-nucleon cross section. Using $\rho \simeq 0.17\,\mathrm{fm}^{-3}$ and $\sigma \simeq 25$–$40\,\mathrm{mb}$, yields $\lambda \simeq 1.6$–$2.3\,\mathrm{fm}$. For heavy nuclei $\lambda < R$, the nucleus radius, and these models are plausible.

The fireball model[24] assumes a clean geometry. The overlap region coalesces into a highly excited "fireball" which thermalizes, while the projectile and target spectators maintain nearly their original velocities. The spectators are excited due to the interaction friction and their deformed shapes, and decay largely by particle emission. Emission from the fireball should be isotropic in the nucleon-nucleon center of mass frame and this is not experimentally verified. However this model provides an easily comprehensible benchmark for more complicated models.

A successful modification of the fireball model that retains most of its simplicity is the firestreak model[25]. Instead of allowing the participant region to thermalize, this model imposes a continuous distribution of parallel streaks. The different streaks have different center of mass velocities, and emission is no longer isotropic in the center of mass frame.

Most models describing central collisions, however, are hydrodynamic. Typical of these models are the Los Alamos[26] and Frankfurt[27,28] codes. The major differences in these codes are: (1) The Los Alamos code is relativistic, while the Frankfurt code is not. (2) The Frankfurt code contains binding effects and potentials which the Los Alamos code does not. (3) The Los Alamos

code uses the particle in a cell method[29], and the Frankfurt code uses a flux corrected transport algorithm[30]. Qualitatively both codes make similar predictions. In central collisions the projectile-target system pancakes, and matter is ejected to the sides in a "side-splash" (Figure 2.1a). In off center collisions projectile and target residues are deformed and pushed apart in a "bounce-off" (Figure 2.1b)[28].

2.3 Peripheral Collisions

2.3.1 Overview

Microscopic cascade models are best suited to describing peripheral collisions. The small number of nucleon-nucleon collisions makes the tracking of individual nucleons desirable. Full quantum mechanical treatment of the system has proved impracticable so drastic simplifications have been made. The collision process is treated as a sequence of free nucleon-nucleon binary collisions. Again there are many models extant, so we will discuss two representative models, the VEGAS code[31] and the Cugnon code[19]. Since we chose to compare our data to the Cugnon code we will discuss it in greater depth later (Section 2.3.2).

Like most cascade codes used for nucleus-nucleus collisions, the VEGAS code has evolved from a nucleon-nucleus code. As such it incorporates a nuclear medium. The initial nuclei are not composed of nucleons (called cascade particles), but are continuous media in which cascade particles are created when an

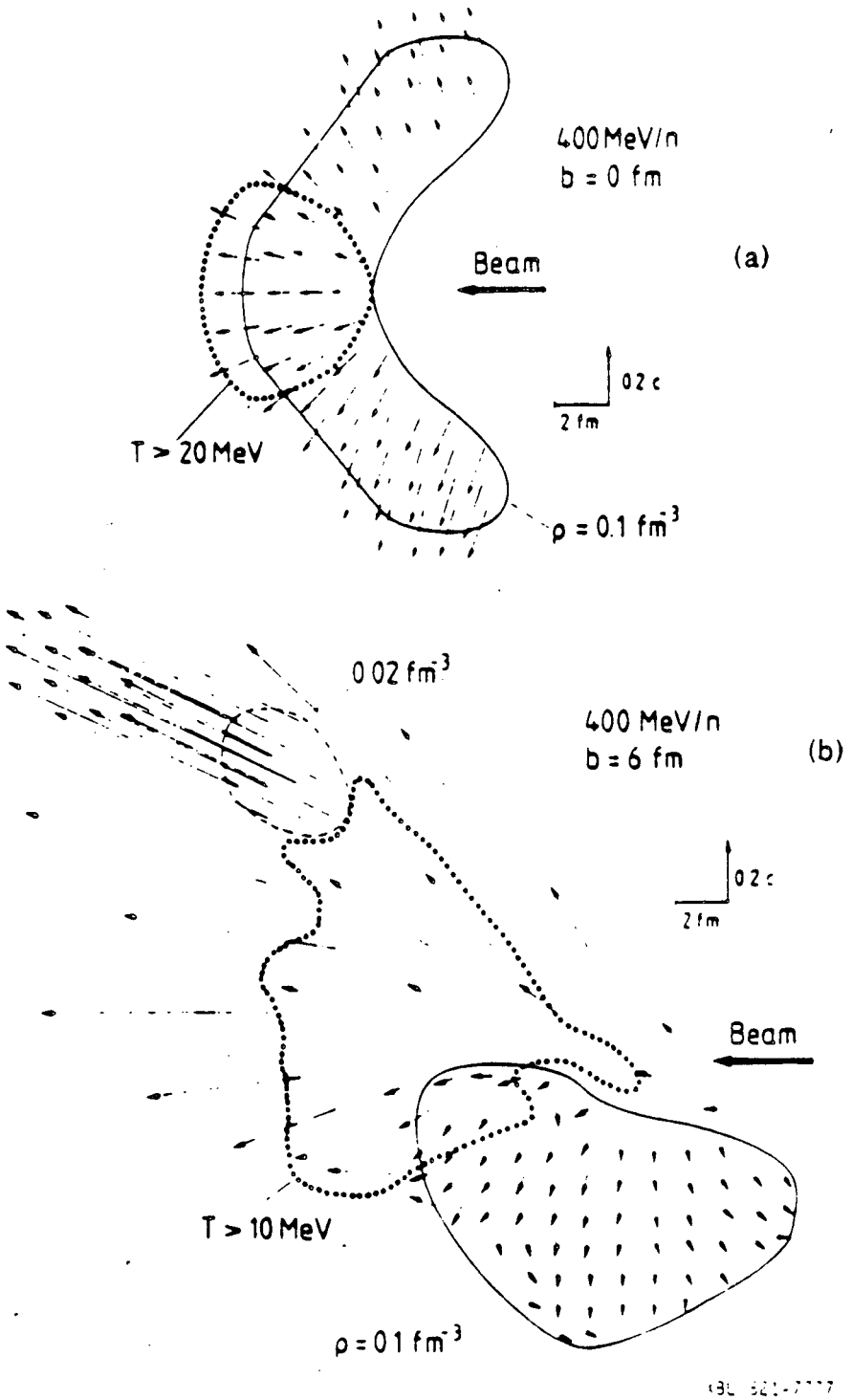

Figure 2.1: Hydrodynamic model calculations for Ne on U at 400 MeV/nucleon with impact parameters of (a) $b = 0$ fm and (b) $b = 6$ fm. In central collisions (a) the projectile-target system pancakes, and matter is ejected to the sides in a "side-splash". In off center collisions (b) projectile and target residues are deformed and pushed apart in a "bounce-off" [28].

interaction occurs. This avoids the problem of describing the ground state, but introduces the problem of how to deplete the nuclear medium when a cascade particle is created. VEGAS offers two choices: (1) "fast" in which the density distribution is uniformly depleted, or (2) "slow" where there is a local depletion. This difficulty is the reason we chose not to use this model in comparing to our data, also all models give similar results when compared to proton inclusive data. The nuclear medium is a cold Fermi gas with a folded Yukawa density distribution.

The Pauli principle is accounted for by requiring the cascade particles to have more than the Fermi energy. The reactions $N + N \rightleftharpoons N + \Delta(1232)$ and $\Delta(1232) \rightleftharpoons N + \pi$ are allowed to occur. Finally, relativity is accounted for by Lorentz contracting the projectile. Like all such models, it has been successful in predicting the proton and π inclusive cross sections.

2.3.2 Cugnon Monte Carlo Cascade Code[19]

This is the model we chose to compare to our data. Our objective was to identify, as transparently as possible, the nucleon-nucleon collision component in our data. We found this model to be the best suited to our purpose, and we describe its main features now. We will point out modifications made, but will defer detailed discussion until we compare with our data (Section 6.2).

1. The nuclei are spheres of radius $1.12A^{1/3}$ fm ($1.3A^{1/3}$ fm for ^{12}C). Here A is mass number. Constituent nucleons are given random positions with a uniform distribution, and random momenta with a Fermi gas distribution with the Fermi momentum $P_F = 270\,\mathrm{MeV/c}$. This value was chosen for bigger nuclei and is too large for ^{12}C. We found it necessary to use P_F as an adjustable parameter.

2. Isospin is not considered. We found it necessary to add isospin weights.

3. After the initial positions and momenta in the projectile are randomly chosen they are Lorentz boosted by the projectile velocity.

4. The calculation begins when the spheres of nuclei touch. The nucleons move along straight lines until closest approach. If this distance is smaller than $[\sigma_{tot}(\sqrt{s})/\pi]^{1/2}$ then that pair scatters. Here σ_{tot} is the total cross section for pair at center of mass energy $\sqrt{s}$. The scatter is randomly elastic or inelastic according to the relative ratios of the associated cross sections. The momenta after the collision are determined randomly from appropriate center of mass angular distribution. Energy and linear momentum are conserved but angular momentum is not. The particles then resume straight line motion.

5. Inelastic scattering proceeds entirely through the $\Delta(1232)$ resonance. The following reactions can occur:

   (a) $N + N \rightarrow N + N$

(b) $N + N \rightarrow N + \Delta$

(c) $N + \Delta \rightarrow N + \Delta$

(d) $N + \Delta \rightarrow N + N$

(e) $\Delta + \Delta \rightarrow \Delta + \Delta$

Cross sections (a) and (b) are taken from experimental data[32]. Cross section (d) is obtained from (b) by detailed balance. Cross sections (c) and (e) are taken to be the same as (a). For a 2.1 GeV kinetic energy the p-p total cross section is 45.0 mb, while the p-n total cross section is 43.0 mb. The p-p elastic cross section is 19.2 mb, and no value for p-n exists. However at 5.6 GeV the elastic cross sections are 10.2 mb and 12.5 mb respectively.

6. The elastic cross section is taken as

$$\sigma(t) \propto e^{A(s)t}$$

where t is the Mandelstam t, and

$$A(s) = 6\frac{[3.65(\sqrt{s} - 1.8766)]^6}{1 + [3.65(\sqrt{s} - 1.8766)]^6}.$$

Here $\sqrt{s}$ is the center of mass energy measured in GeV, and A is measured in $(\mathrm{GeV/c})^{-2}$.

7. The $N + N \rightleftharpoons N + \Delta$ process is usually given an isotropic distribution. We found it necessary to use: $\sigma(t) \propto e^{bt}$ where t is the Mandelstam t, and $b = 10.11\,\mathrm{GeV}^{-2}$[32].

8. The Δ lifetime was originally infinite and then modified to be exponential.

9. All kinematics are relativistic.

10. Quantum effects are mostly ignored. There is no mean field, and there are no three body collisions.

11. Soft nucleon-nucleon collisions are suppressed if the total center of mass energy is less than the rest masses plus 50 Mev. This approximately accounts for Pauli exclusion.

For our reaction (^{12}C,^{11}B+p), one nucleon-nucleon scatter is the most likely occurrence (Figure 2.2). However, a single projectile proton could scatter successively with target nucleons, and this is allowed in this model. Alternatively, the collision could be so peripheral that a nucleon-nucleon scatter does not occur. Instead, the projectile is excited and then decays by proton emission in these grazing collisions. We discuss this possibility next.

2.4 Grazing Collisions

Lukyanov and Titov pointed out that the inclusive spectra[13,14,15,16] could also be explained by excitation and decay[33]. Their result was general and did not specify a reaction mechanism. Since then two possibilities have emerged: electromagnetic[34] and nuclear Weiszäcker-Williams dissociation[18].

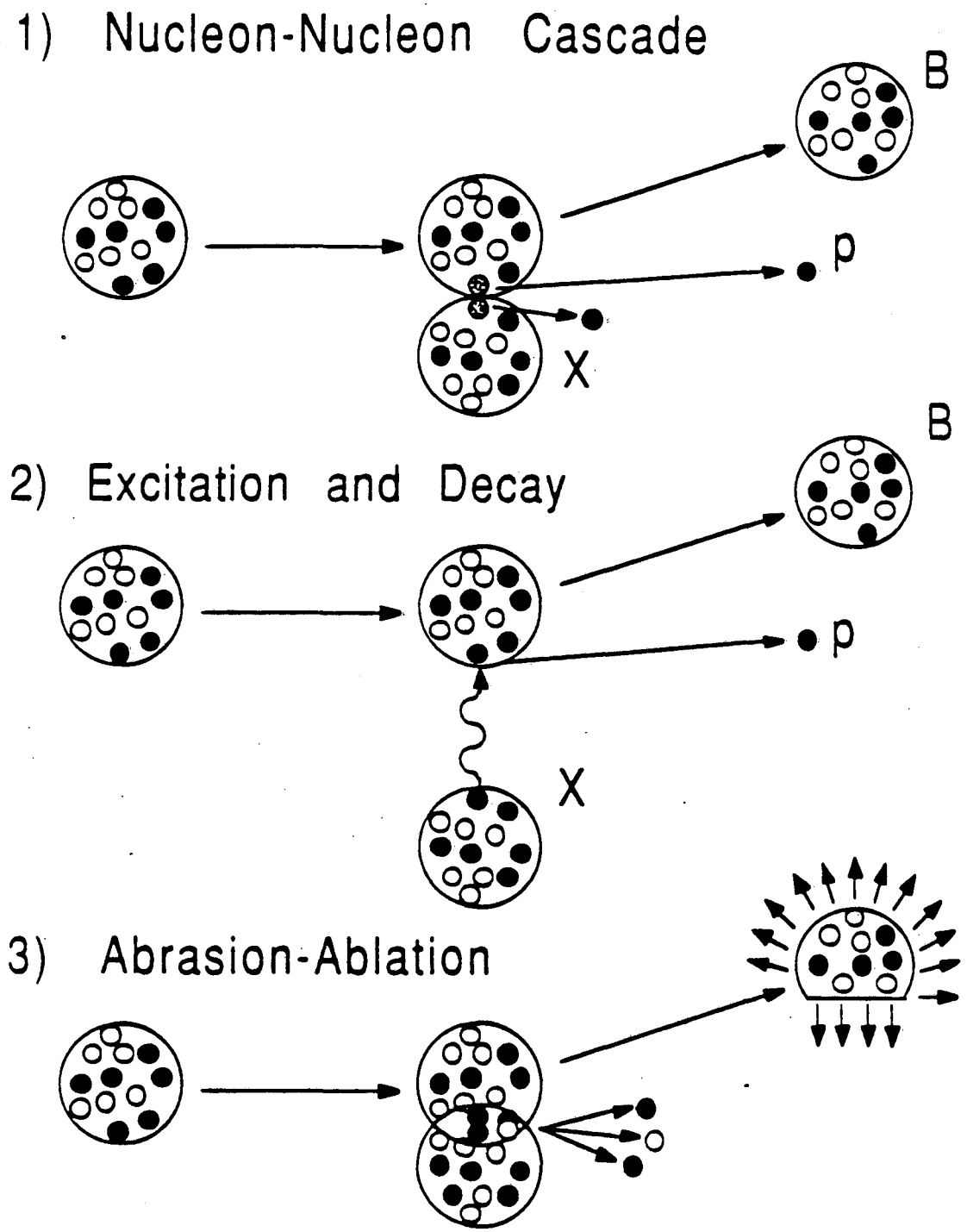

Figure 2.2: Possible (^{12}C,^{11}B+p) reaction mechanisms. (1) One proton in the projectile scatters from one or more nucleons in the target. (2) The projectile is excited by the target and then decays by particle emission. (3) Reactions where many projectile nucleons interact are prohibited, as are reactions where the projectile spectator decays by particle emission following a proton-nucleon scatter.

Electromagnetic Weiszäcker-Williams dissociation occurs when the projectile fragments in the Coulomb field of the target nucleus. The projectile absorbs a photon and then decays by particle emission. For a given projectile mass and energy, the cross section of this process, σ_{em}, scales as $Z_T^2 b_{min}^2$ where Z_T is the target charge, and b_{min} is the minimum impact parameter for the process. The target dependence of b_{min} can be incorporated in the exponent of Z_T giving $\sigma_{em} \propto Z_T^{1.8}$[35]. The reaction ^{29}Cu(^{12}C,^{11}B+x)X at 2.1 GeV/nucleon has a σ_{em} of 4 mb[36]. With the $Z_T^{1.8}$ scaling this process contributes a negligible amount of cross section to our reaction, 0.2 mb for a C target and 0.09 mb for a H target, therefore, we do not compare this mechanism to our data.

Nuclear Weiszäcker-Williams dissociation occurs when the projectile fragments in the nuclear mean field of the target nucleus. The projectile absorbs a "phonon" and then decays by particle emission. The cross section for this process is not well known, but it has been claimed[18] that this model is consistent with proton inclusive data. We will compare this model to our data.

Chapter 3

Experimental Setup

3.1 The Bevalac

The Bevalac, a hybrid of the Super-Hilac and Bevatron accelerators at the Lawrence Berkeley Laboratory, provided the ^{12}C beam for this experiment. The Hilac, a linear accelerator, stripped the ^{12}C nuclei and then accelerated them to a kinetic energy of 8.5 MeV/nucleon. The beam was then sent to the Bevatron through a transfer line at a rate of 1 to 2 pulses per second. The Bevatron, a weak focussing synchrotron, then raised the kinetic energy to 2.1 GeV/nucleon[37].

Then beam was extracted and directed to beam line 42 at a rate of 10 pulses per minute. The beam line contained 3 dipole magnets and 7 quadrapole magnets which were used to transport the beam to the HISS experimental area (Figure 3.1). Three swinger quadrupoles, five meters upstream of the HISS dipole provided the final beam focus.

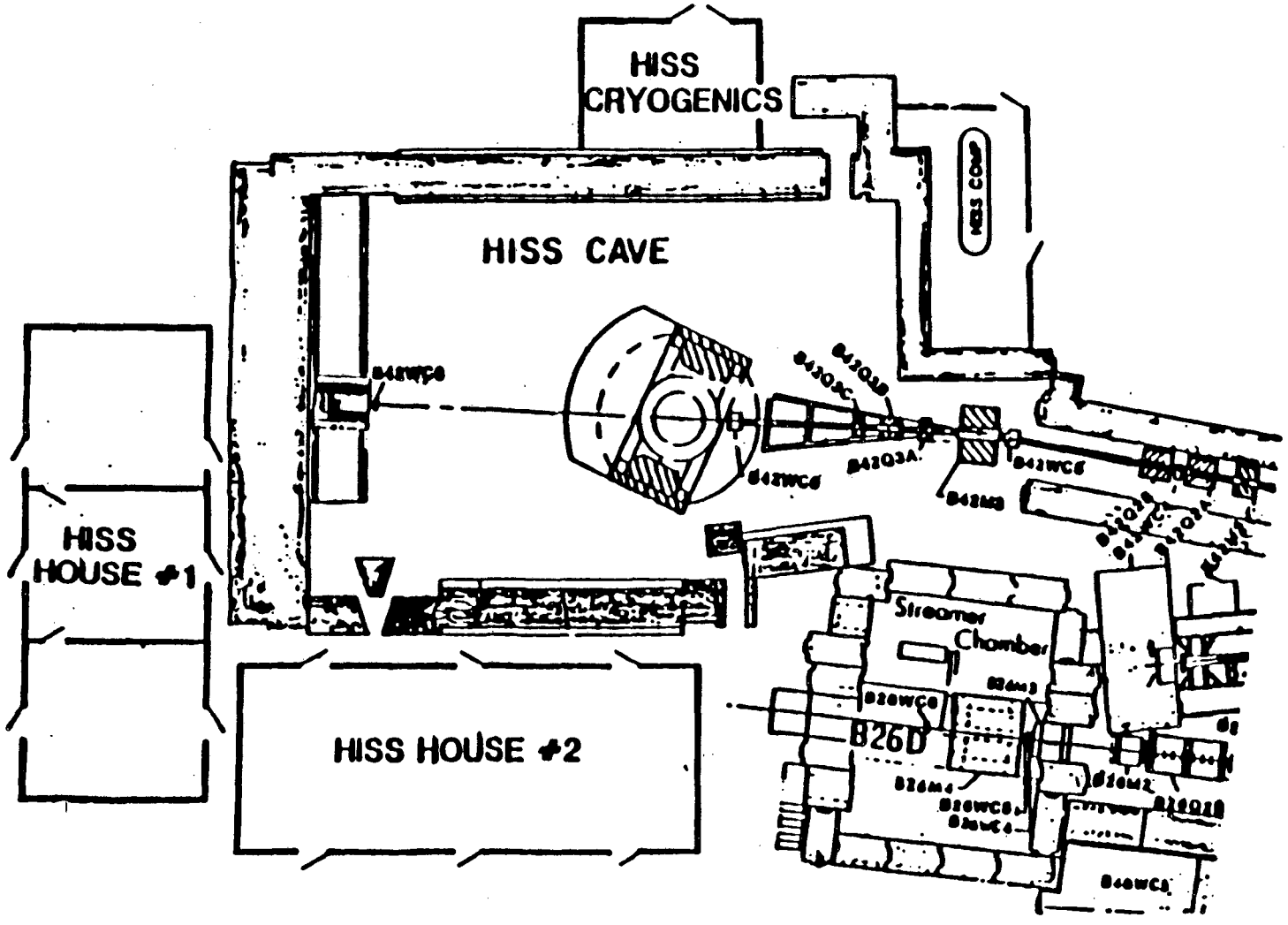

Figure 3.1: The HISS experimental area.

3.2 The Magnet

The heart of the spectrometer system is the 625 ton superconducting dipole. The HISS magnet has pole tips with a diameter of 2.1 m, a gap of 1 m, a maximum central field of 3 T, and a maximum $\int B \cdot dl = 7.5\,\mathrm{T{\cdot}m}$ (Table 3.1). A 40 ton stainless steel vacuum tank with a 1×3 m exit window rested between the pole tips and this reduced background interactions (Figure 3.2). A steel yoke limited the stray field[38].

The dipole is cooled by a 400 W helium refrigerator from Cryogenic Consultants Inc. with a Sullair screw type compressor. The refrigerator is a Claude cycle, liquid nitrogen precooled, twin series expander (20° K and 5° K expansion) device using wire wound heat exchangers and piston expanders[39]. The cryogenic system is computer controlled by a Digital Equipment Corporation LSI 11/23 microprocessor with a touch screen input.

Electrical, mechanical, and cryogenic systems are monitored once per second by more than 100 sensors. These sensors include 32 strain gauges monitoring the mechanical integrity of the support cylinders, 19 thermistors measuring coil and helium gas temperatures, 30 solid state pressure and liquid level sensors gauging the pressure and fluid level of the helium coolant, 8 isolation amplifiers tracking voltages in the coils, and 48 channels of relay input registers scanning power supply and quench protection chains. The quench detectors switch out

Table 3.1: The physical parameters of the HISS dipole.

HISS Magnet Parameters

Central field	3 Tesla
Field on conductor	4.6 Tesla maximum
Superconducting coil	Nb-Ti in Cu matrix in liquid He
Conductor cross section	1.19 cm × 0.4 cm
Copper/Superconductor ratio	19:1
Ampere turns	5.12×10^6
Current	2200 A
Conductor current density	5000 A/cm^2
Magnetic energy	55.2 MJ
Yoke: Window frame type	5.13×10^5 Kg
Pole diameter	2.1 m (83 inches)
Magnet gap	1.0 m (40 inches)
Unobstructed azimuthal angle	110° at front and back
Mounting	Rotatable base
Magnet total mass	5.67×10^5 Kg

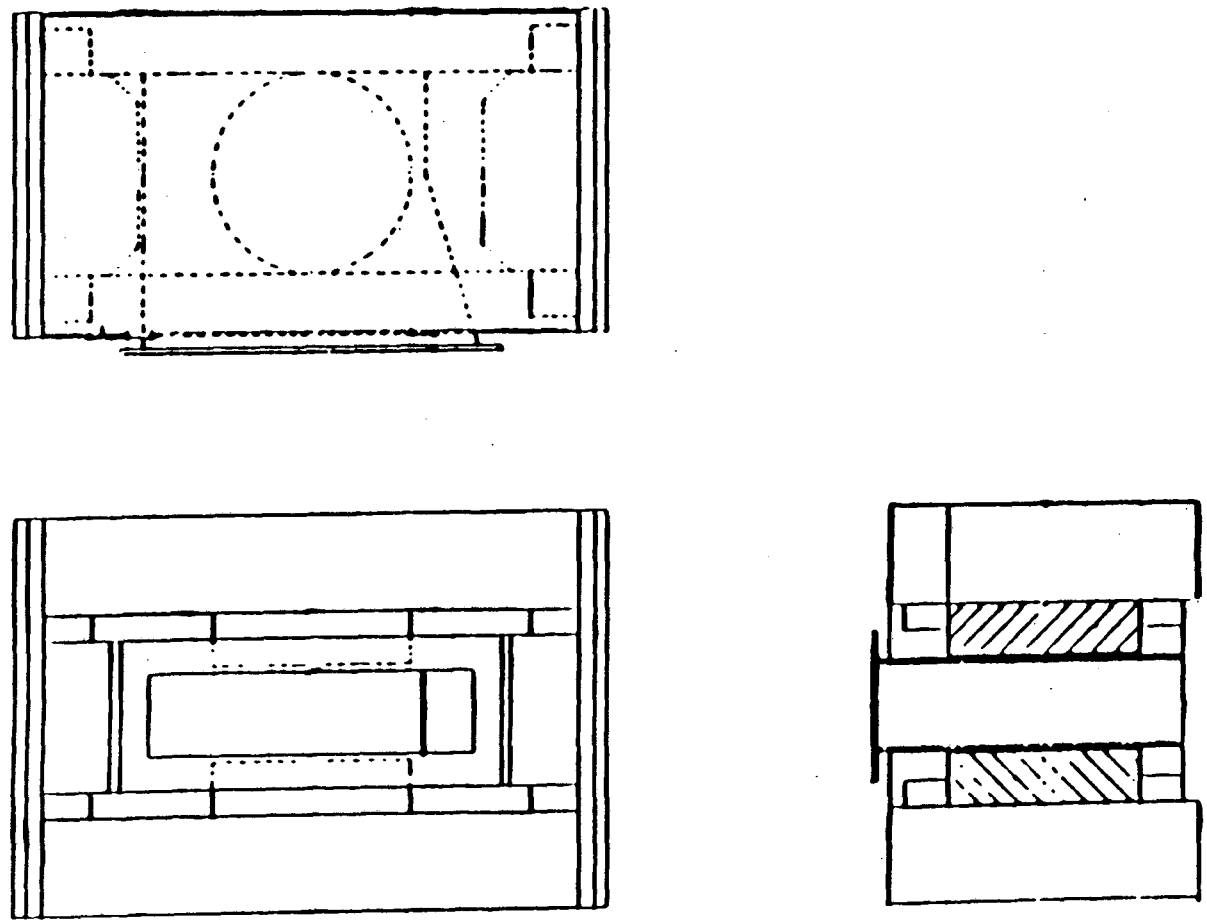

Figure 3.2: The HISS dipole and vacuum chamber.

the power supply if a resistive voltage is found in the coils and discharge the circulating current through a 4000 lb, 0.22 Ω, iron dump resistor that is hard wired to the coils[38]. A PDP 11/34 computer reads the sensor data via CAMAC and provides several graphic displays for immediate analysis. The data are then logged on a VAX 11/780 (Figure 3.3)[40].

3.3 Detector System

3.3.1 Beam Definition Scintillators and Start Logic

The first two of five beam definition scintillators were 15 m upstream of the dipole (Figure 3.4). The $TOF1$ and TOT scintillators provided the start for the time to digital converters (TDC). The second set of scintillators, E and HS, were 10 m downstream of $TOF1$ and TOT. The 0.020 inch thick E scintillator's output passed through a window discriminator to veto all but single ^{12}C projectiles. The 0.25 inch thick HS scintillator had a 2.0 inch hole in its center and was used as a veto. The coincidences between E and $\overline{HS}$ measured beam flux. The remaining beam scintillator, DS, was 8 m downstream of the dipole center and vetoed charge six particles in the beam envelope.

The five beam scintillators defined the raw interaction trigger with logic ($TOF1 \bullet TOT \bullet E \bullet \overline{HS} \bullet \overline{DS}$) (Figure 3.5). For a valid event trigger we further required that no particle had entered the detectors in the preceding 250 ns. To accomplish this we included an updating one shot ($UDOS$) in the logic. The

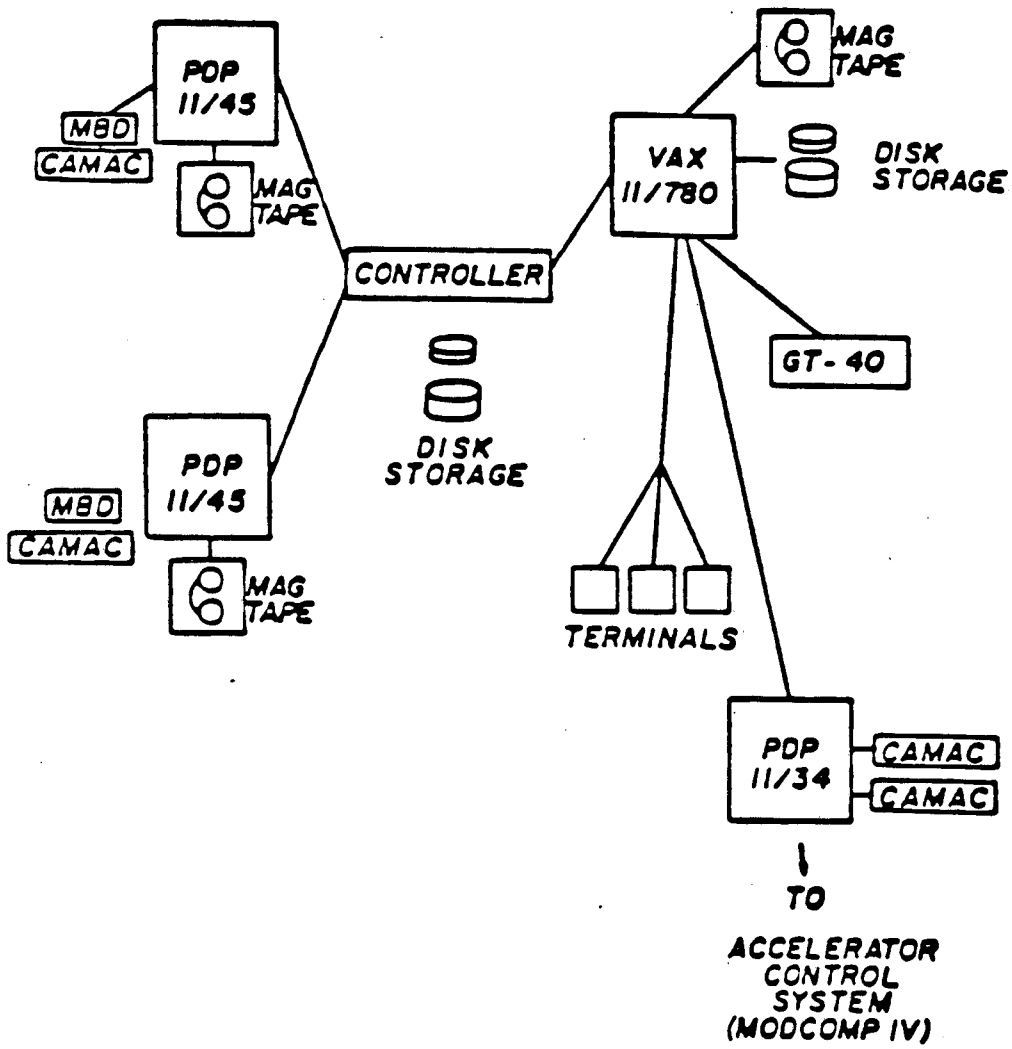

Figure 3.3: The HISS computer system.

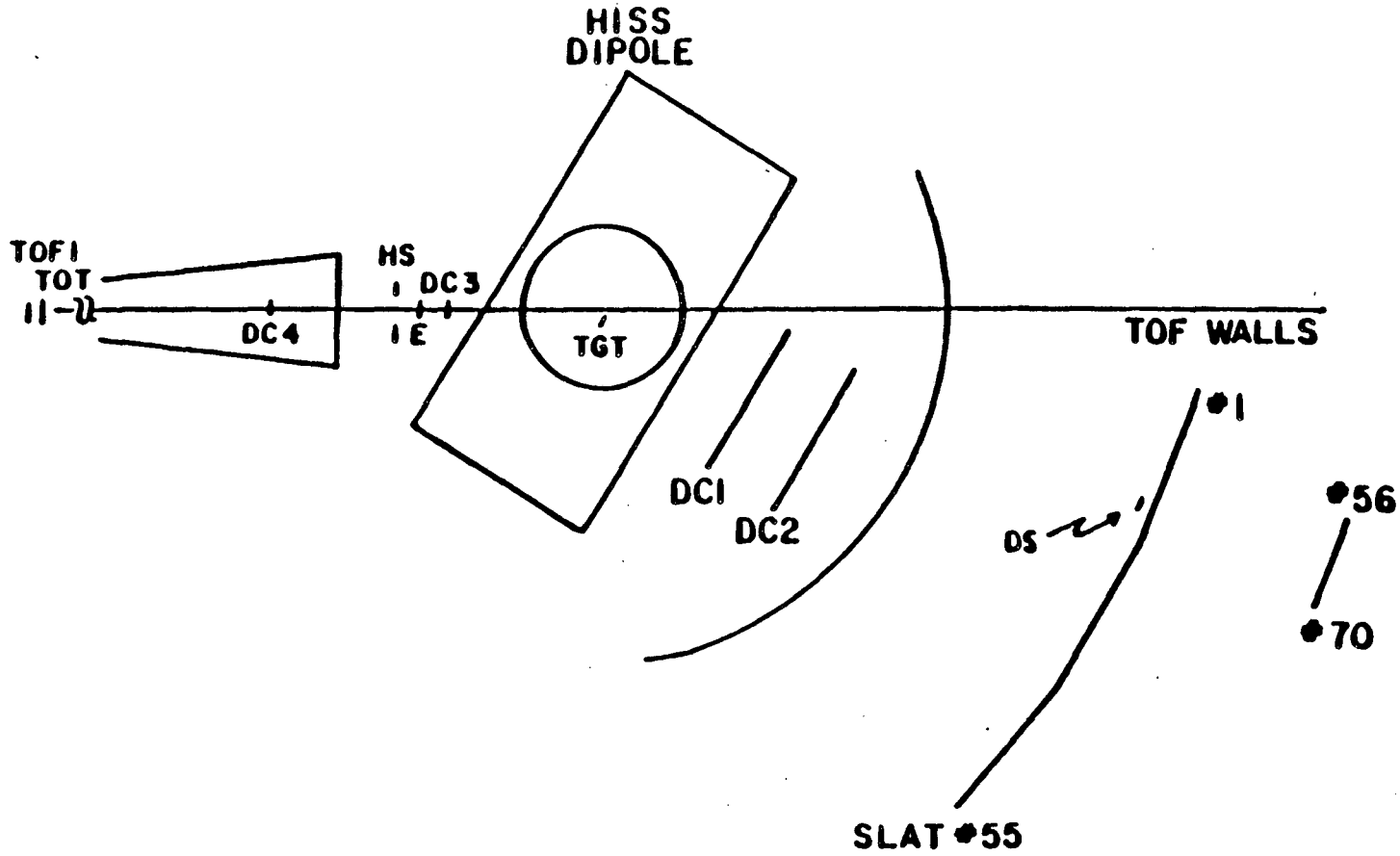

Figure 3.4: Detector Placement. Beam scintillators $TOF1$, TOT, HS, E, and DS defined the trigger with logic ($TOF1 \bullet TOT \bullet E \bullet \overline{HS} \bullet \overline{DS}$). Drift Chambers $DC4$, and $DC3$ determined the incoming ^{12}C trajectory and drift chambers $DC1$ and $DC2$ determined the charged projectile fragments' trajectories. The TOF wall, an array of 10 cm wide scintillators, determined the charge and time of flight for all projectile fragments.

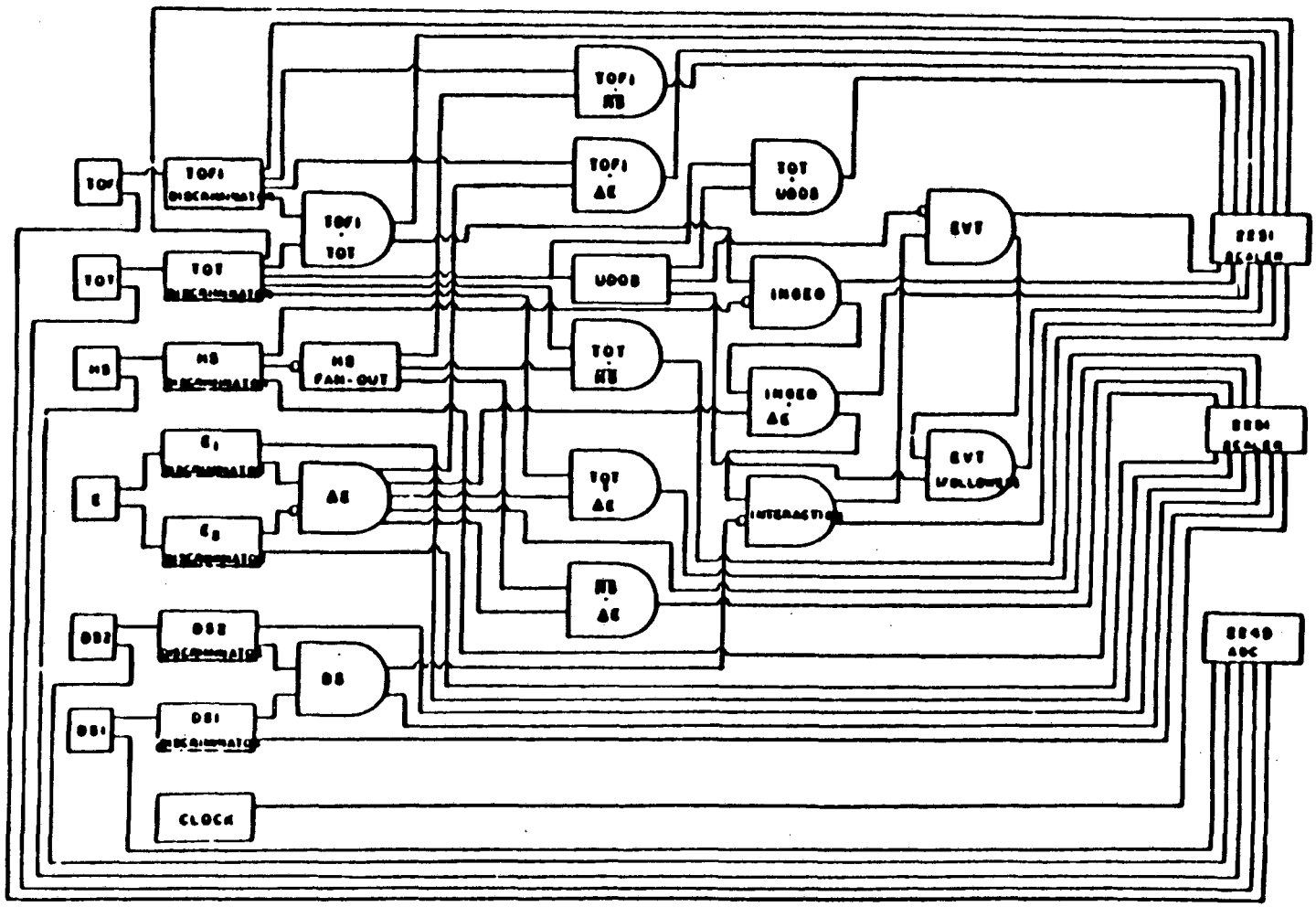

Figure 3.5: Event trigger electronics diagram with logic ($TOF1 \bullet TOT \bullet E \bullet \overline{HS} \bullet \overline{DS}$). The $UDOS$ ensured that no particle had entered the detectors in the preceding 250 ns.

UDOS triggers on the leading edge of a pulse but updates on the trailing edge. Thus with the *UDOS* pulse width set to 250 ns, the *UDOS* turns off only 250 ns after the last preceding pulse. Finally, valid event triggers latched a busy flip flop that prevented further event triggers from reaching the electronics (Figure 3.6). The busy was cleared when the computer was finished encoding the data.

3.3.2 Drift Chambers

The first of four drift chambers, $DC4$, was positioned two meters upstream of the E and HS scintillators. The second upstream drift chamber, $DC3$, was 223 cm downstream from $DC4$. Both $DC3$ and $DC4$ had six sense planes each with a 40 cm × 30 cm active area. These chambers established the beam position and angle in the target. These beam definition chambers were prototypes of the other two drift chambers, and have the same mechanical construction and electronic instrumentation.

The large drift chambers, $DC1$ and $DC2$, were 250 cm and 345 cm downstream of the HISS dipole center. They also contained six sense planes and eight high voltage foil planes. However their active area was 2 m × 1 m, requiring a 1 inch thick aluminum frame for support (Figure 3.7). The high voltage foil planes were aluminized mylar, 100 nm of aluminum on 1/4 mil mylar. The foils were stretched across epoxy-fiberglass windows made of NEMA-G10. The wire planes were 75 μm Beryllium-Copper wire stretched and glued on frames made

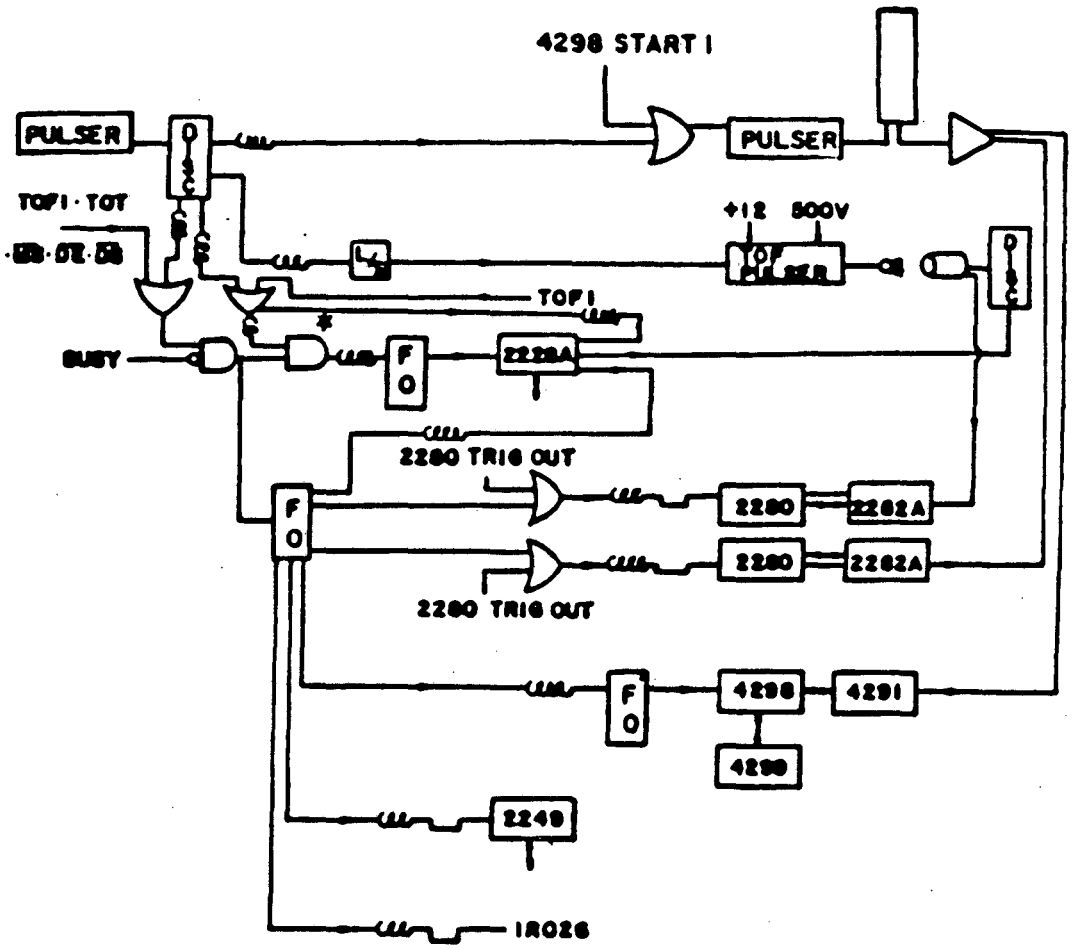

Figure 3.6: Common start electronics with logic ($TOF1 \bullet TOT \bullet E \bullet \overline{HS} \bullet \overline{DS}$). The start is issued to the TOF TDCs (2228A), TOF ADCs (2280,2282A), DC TDCs (4298,4291), Beam scintillator ADCs (2280,2282A), and the computer (IR026).

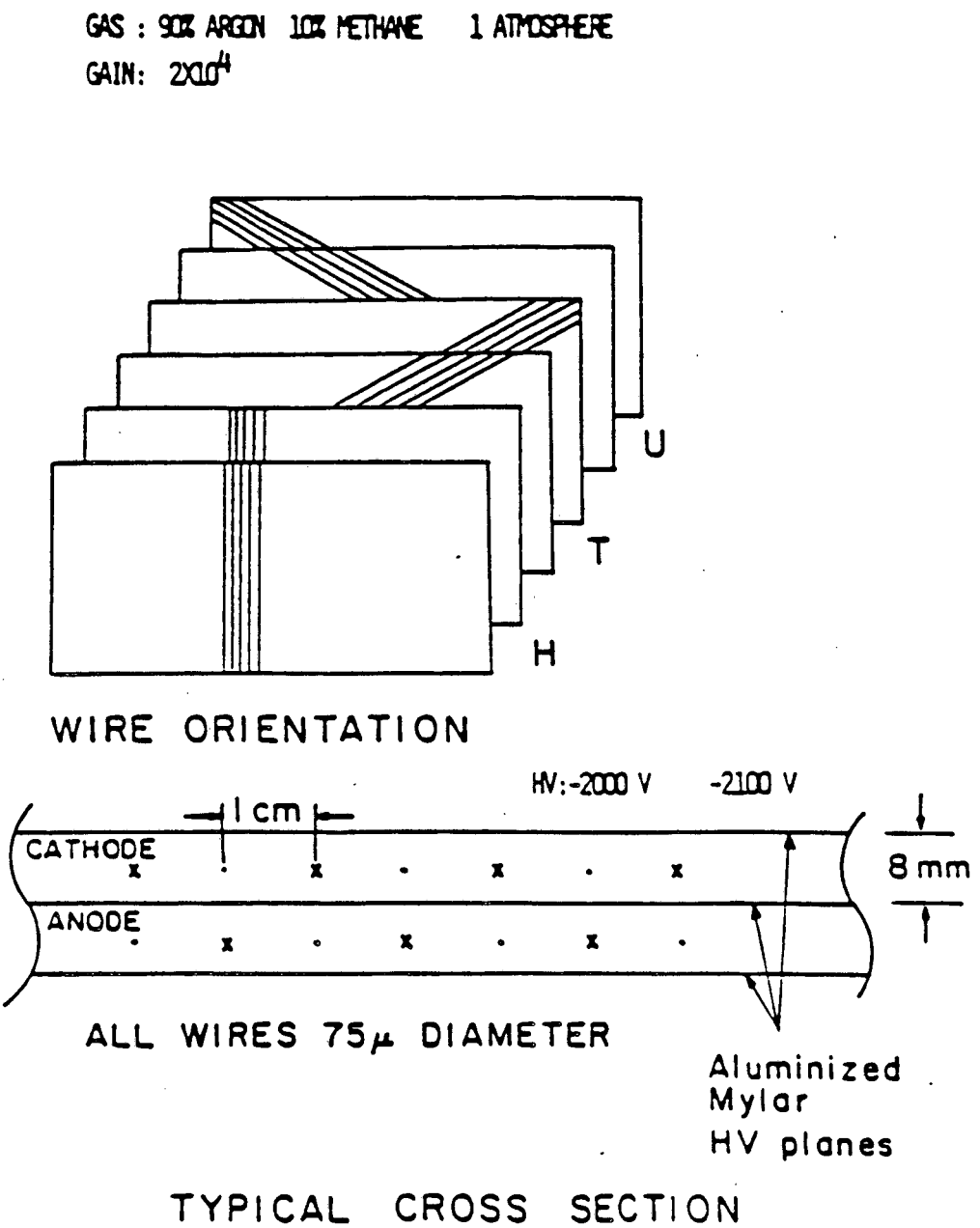

Figure 3.7: HISS drift chamber construction diagram.

of printed circuit board and epoxy-fiberglass plates. The wires were oriented at 0°, +60°, and −60° with respect to their fiberglass frames. The wires were spaced 1 cm apart, alternating anode (sense) and cathode (high voltage). Planes of similar wire orientation were aligned in pairs such that the high voltage wires of one plane were shadowed by the sense wires of the other plane. This alignment made it possible to determine whether a particle passed to the right or left of each sense wire. Each chamber provided a measurement for each of the three orientations listed above. This redundancy in measuring position, coupled with the thickness of the chambers was used to calculate the direction of motion for each ion.

3.3.3 Time of Flight (TOF) Scintillation Array

The *TOF* array mentioned above has two sections of 20 plastic scintillators with dimensions $2.5 \times 10 \times 300\,\mathrm{cm}^3$, and two sections of 15 scintillators with dimensions $2.5 \times 10 \times 300\,\mathrm{cm}^3$. These were placed about 4.5 meters behind *DC*2. Each scintillator is individually wrapped and has Amperex XP2230 photomultiplier tubes at top and bottom. Each tube is connected to a base that is modified to operate over a large dynamic range while exhibiting only a small distortion in pulse shape. Each section of the *TOF* array is powered by a LeCroy HV4032A computer controlled high voltage power supply. The high voltage was set so that each tube delivered a 300 mV pulse when irradiated with a ^{90}Sr source at the *TOF* slat midpoint. The tube bases are equipped with two anode outputs, one

of which is connected to a LeCroy 2280 PHA system. The second anode supplies the stop for the individual channels in a LeCroy 2228A TDC system. The 2228A TDC system was activated by a $TOF1$ logic pulse (Figure 3.8).

3.4 Computing Facilities

Incoming data are read from CAMAC through a microprogrammable branch driver (MBD) and into a PDP 11/45. The PDP 11 then routes the data to a local magnetic tape unit and to a shared 80-megabyte disk (Figure 3.9). This disk stores the experimental data in a circular buffer so that two other PDP 11's, and the VAX 11/780 are able to access the most recent data (Figure 3.3). This allows real time comparisons between current and past data sets. Consequently, one set of programs, in addition to those incorporated into the PDP 11 for spill by spill diagnostics, sufficed for both on-line analysis and off-line data reduction[41].

During the data taking, scalar readings from visual scalars were compared with the values read from the camac scalars by an on-line analysis program, FT83. The flat top display program, FT83, reads the camac scalars via the data acquisition program, DATACQ. (Figure 3.10). Also, the scalar values are read off-line in the program, TYPE1320. The TYPE1320 program is one of eight programs running under the analysis shell program. LULU. The LULU analysis shell is an executive program which contains sophisticated sorting and plotting packages[42].

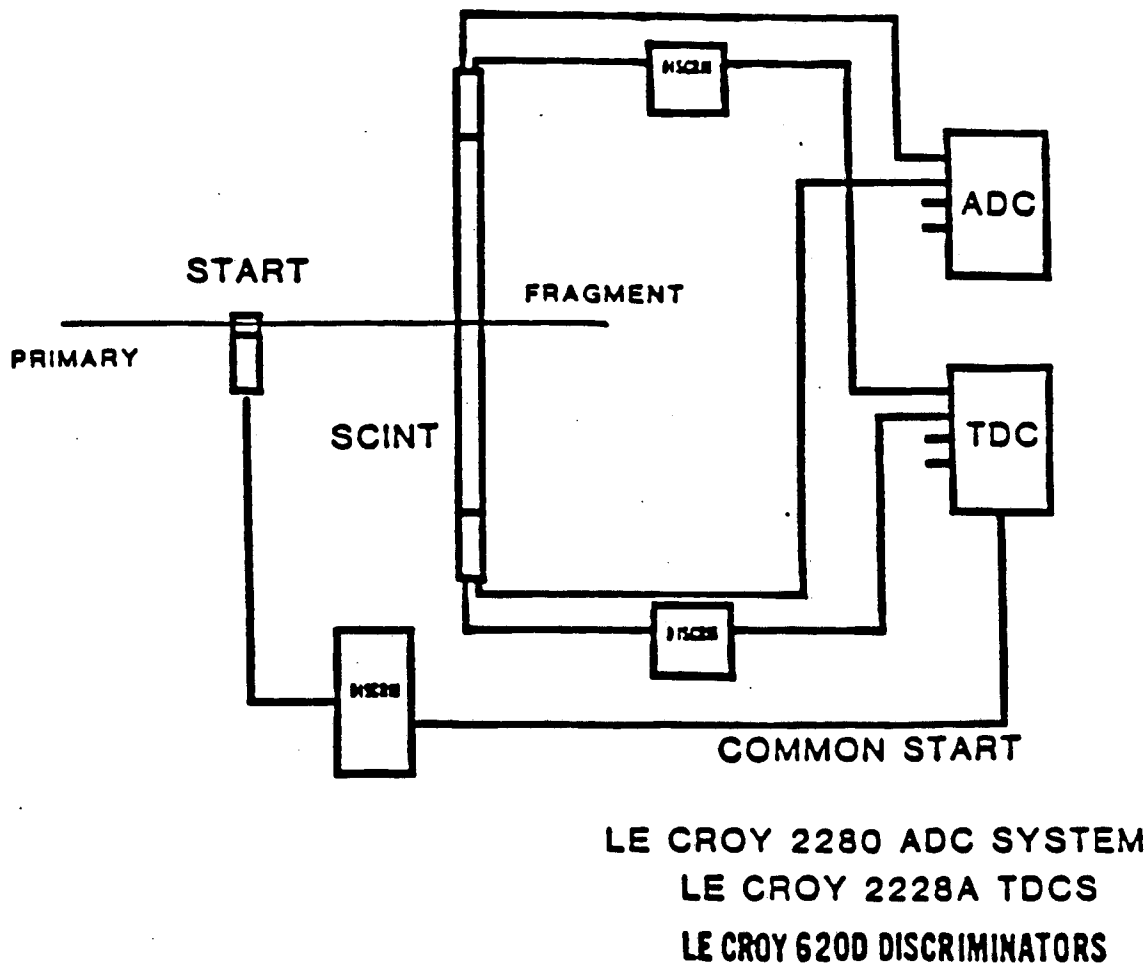

Figure 3.8: Time to digital converters (TDC) start electronics diagram.

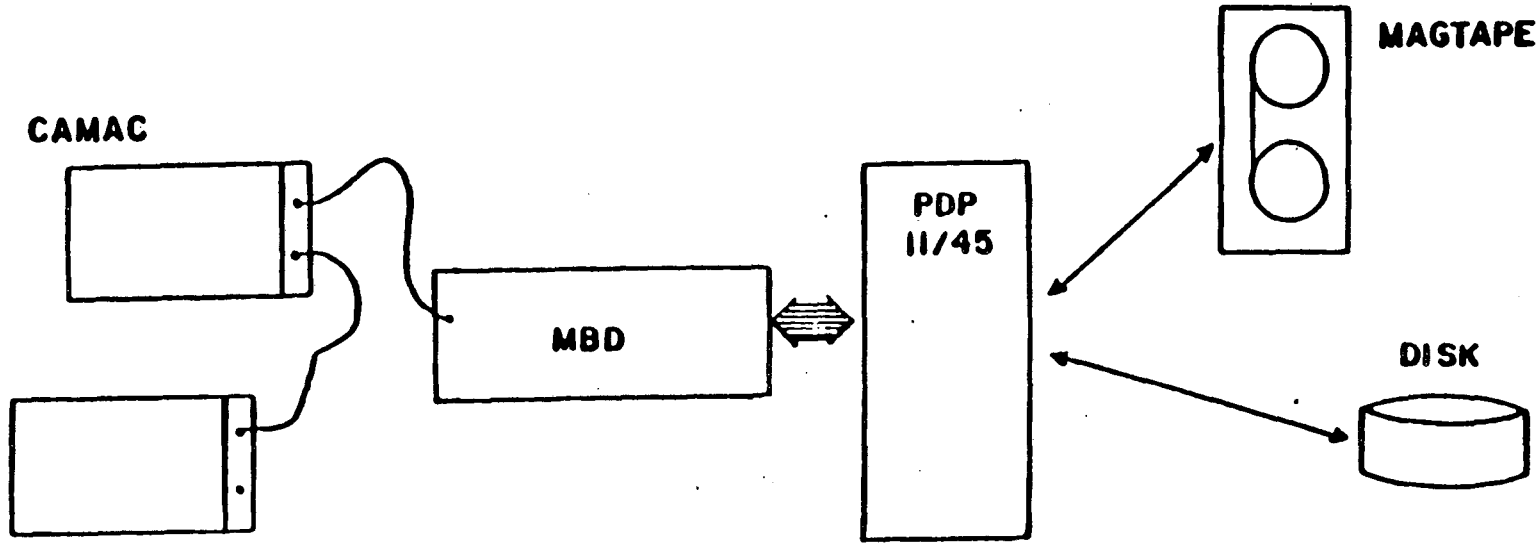

Figure 3.9: HISS data acquisition hardware.

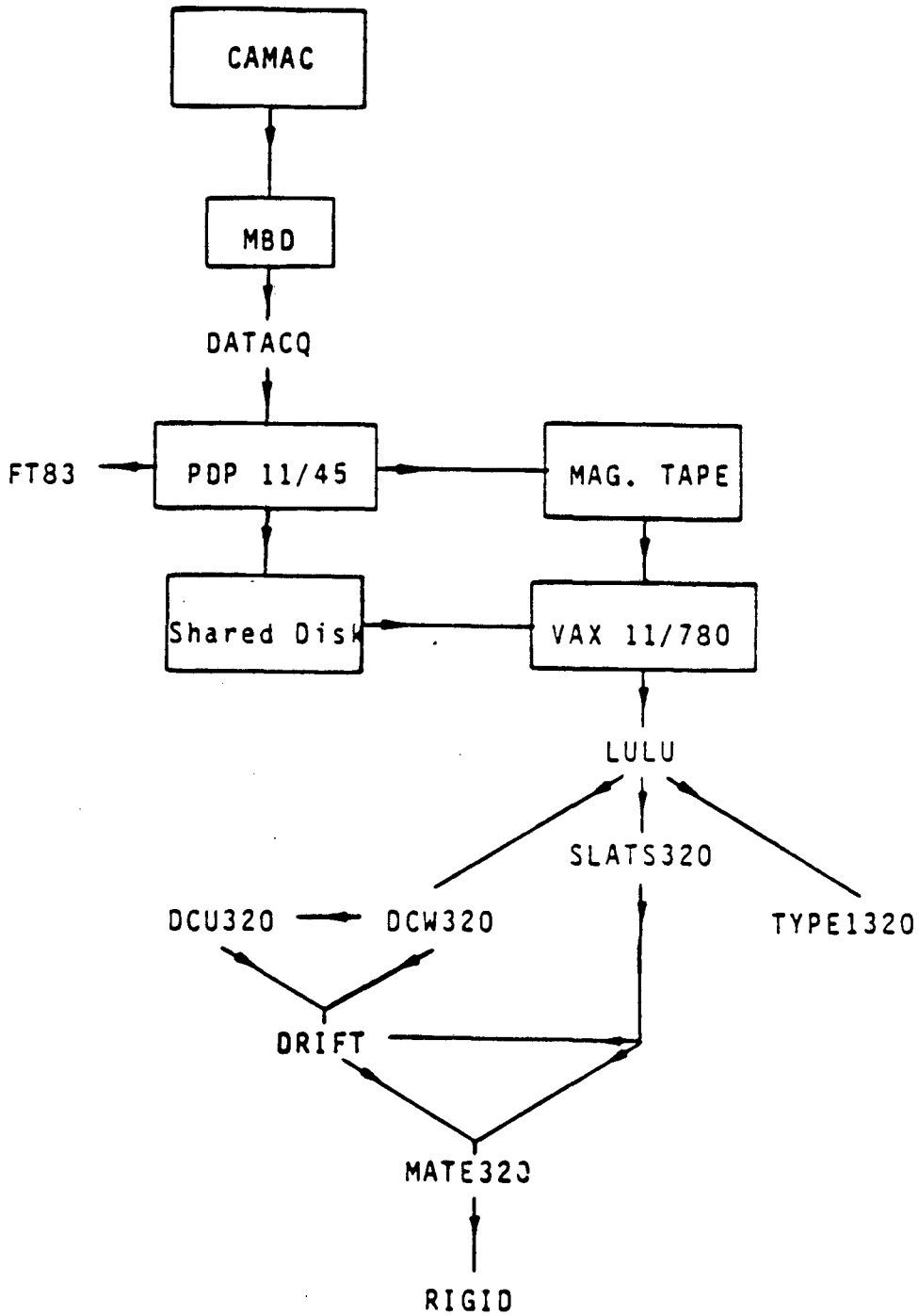

Figure 3.10: Flow chart for the coupling of the data acquisition hardware and software to the data analysis software. Hardware pieces are enclosed in boxes.

Chapter 4

Detector Calibration and Resolution

4.1 TOF Array Calibration and Resolution

The *TOF* wall measured the charge of the ions. A beam of protons and a beam of ^{12}C particles were used to obtain the charge calibration for the *TOF* wall. Both beams were swept across each scintillator of the *TOF* wall by ramping the current in the HISS magnet. The product of the ADC signals from the two photomultiplier tubes on each scintillator was then used with the incident charge to obtain a charge calibration of the form:

$$Prod(Z) = \left[\frac{Z^2}{aZ^2 + bZ + c}\right] \times Prod(Z = 6).$$

The sum of the ADC outputs was not used because the output signals of the ADCs were known to reflect the effects of light attenuation in the scintillator, since the length of the scintillators in the *TOF* wall was about the attenuation length of the scintillator plastic. However, the use of the product of the ADC

outputs cancelled the simple exponential attenuation of the signals. The linear term in Z in the above equation was used to correct for the saturation of the scintillator (Figure 4.1). After corrections, the TOF wall resolved protons with a standard deviation of 0.055 charge units, and ^{11}B's with a standard deviation of 0.14 charge units (Figure 4.2). The proton distribution exhibits a tail at high charge due to delta ray contamination.

The second function of the TOF wall was to measure the time of flight of the fragments. The time of flight for an individual fragment was determined in the following way. First the two TDC values from the photomultiplier tubes attached to the struck scintillator were averaged. Next, a predetermined start time offset, t_o, was subtracted from the above average. The resulting number was then multiplied by the number s, the value of which was about 50 ps/channel, in order to convert the average to an actual flight time in picoseconds. The start time offsets were obtained by sweeping a beam of constant rigidity across the entire time of flight wall. Since leading edge discriminators were used, the output signals from the TDCs exhibited a slight dependence on the rise time of the photomultiplier tubes. The slope of the electronic pulse was a function of the charge of the particle being detected. Thus a second offset, $t(Z)$, was used to cancel the TDC slewing caused by differences in charge. So the equation for the time of flight, t_{TOF}, in picoseconds was

$$t_{TOF} = s \cdot \left[\frac{TDC1 + TDC2}{2}\right] + t_o + t(Z).$$

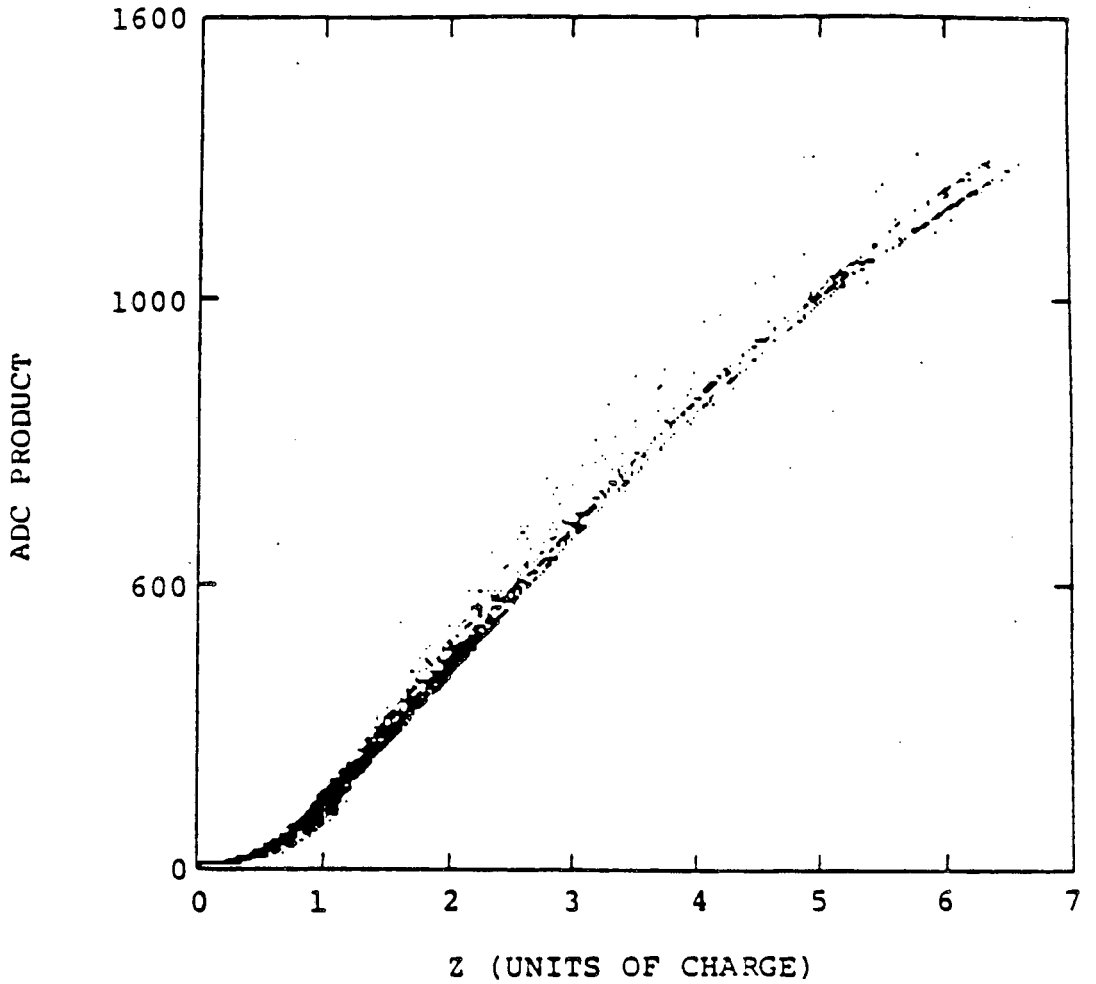

Figure 4.1: ADC product versus charge for scintillator 16. If there were no saturation this curve would be proportional to Z^2. The counts between the integral charges are due to fragments that had shortened tracks because they penetrated the slat sides.

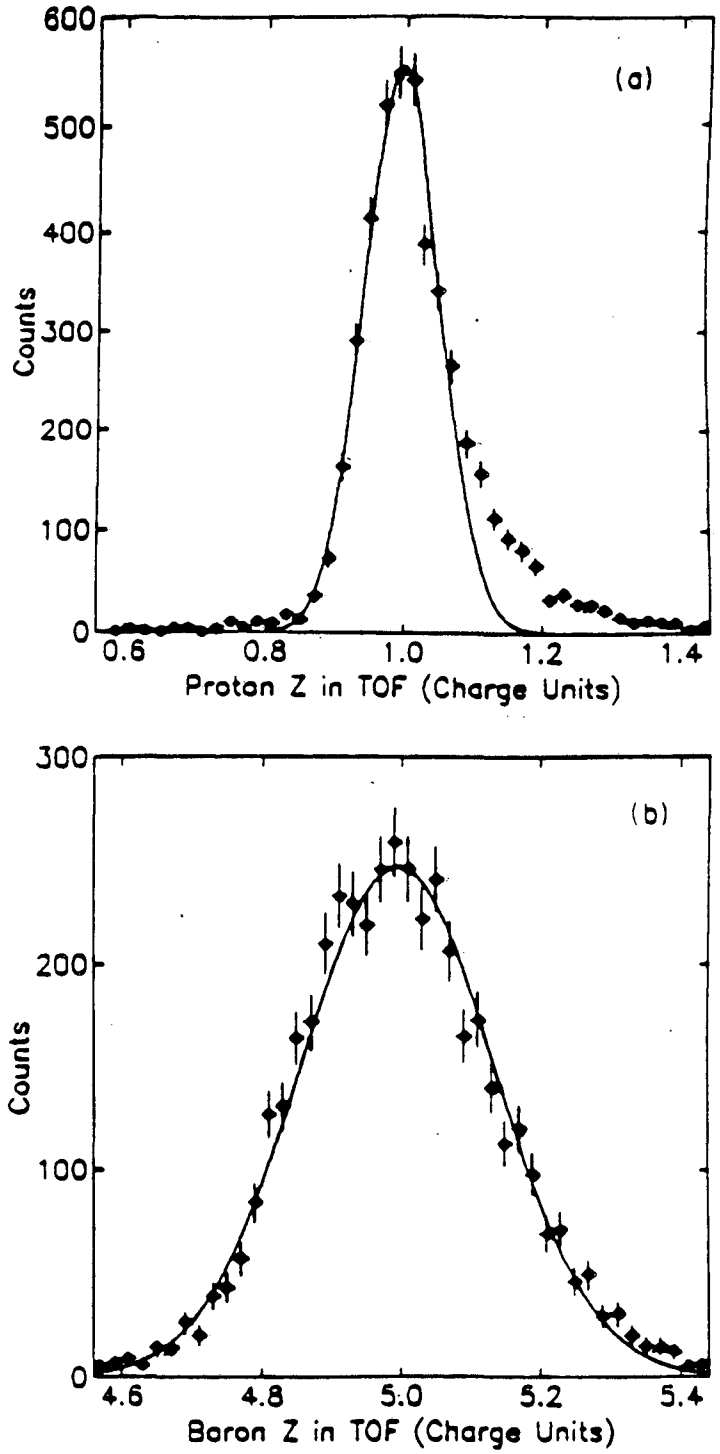

Figure 4.2: Charge distribution in the *TOF* wall for protons and ^{11}B's. The data are fit with a Gaussian of (a) $\sigma = 0.055$ charge units for protons, and (b) $\sigma = 0.14$ charge units for ^{11}B's. The proton distribution (a) exhibits a tail at high charge due to delta ray contamination.

Over a 7.6 m flight path proton times were resolved to a standard deviation of 250 ps, while ^{11}B times had a standard deviation of 170 ps. (Figure 4.3).

4.2 Drift Chamber Calibration and Resolution

4.2.1 Upstream Drift Chambers

The trajectories of incoming beam particles were determined using the twelve (12) TDC values in $DC3$ and $DC4$. The calculated trajectories were subsequently used to generate the **X** and **Y** coordinates at which the beam particle hit the target. Both $DC3$ and $DC4$ also served to identify particles coming from the beam halo, and any events in which the particle interacted in the material upstream of the target. This proved invaluable since several of these projectiles escaped detection by the HS veto scintillator and the window discriminator associated with the E scintillator.

There were three ways in which these so called "bad upstream" events were flagged. First, events in which the incoming beam particle was incident outside the active area of the target were removed. These events were easily identified because their coordinates (X_3, Y_3) in $DC3$, or (X_4, Y_4) in $DC4$, or both lay outside acceptable limits. These limits were established by determining the coordinates of the incoming beam particles that struck the assembly which held the target (Table 4.1). These coordinates in $DC3$ and $DC4$ were obtained by examining the data taken with no target in the beam. Next, events in which the

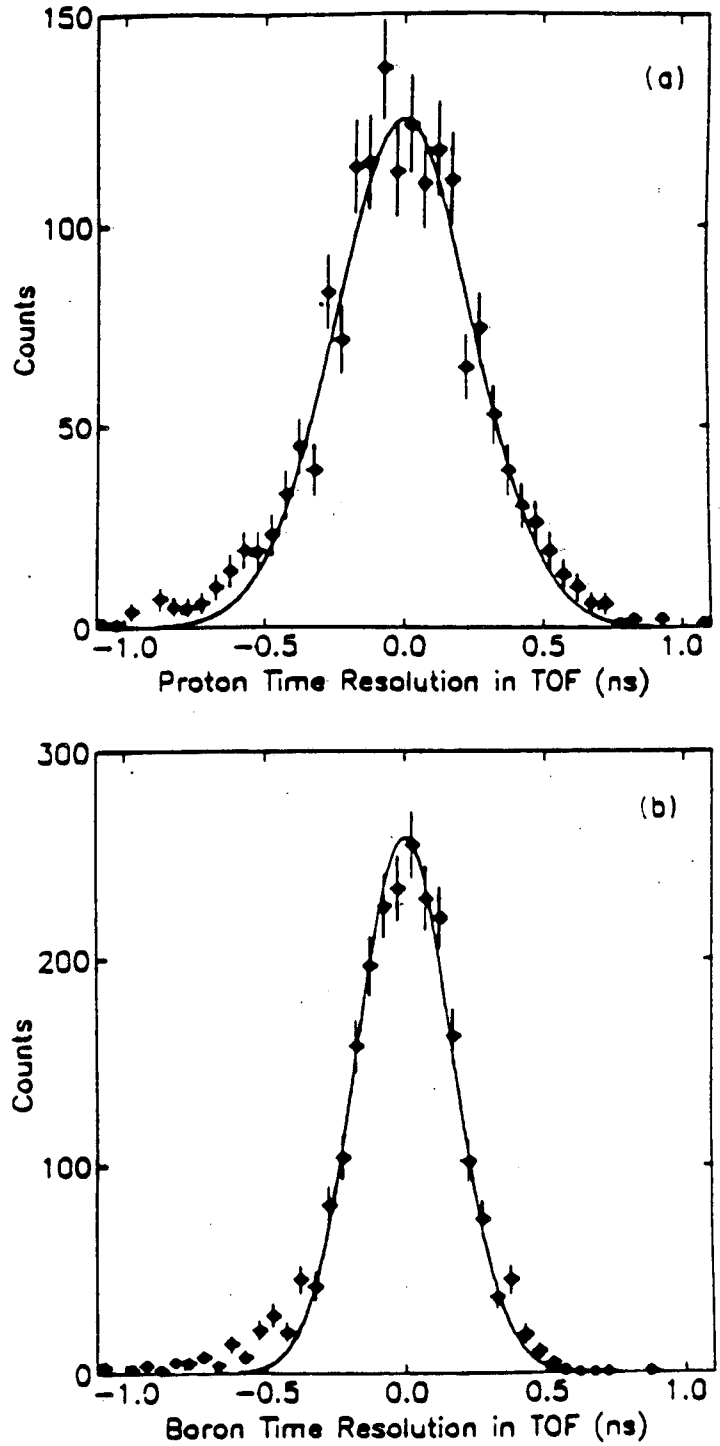

Figure 4.3: Timing resolution in the *TOF* wall for protons and ^{11}B's. The data are fit with a Gaussian of (a) $\sigma = 250$ ps for protons, and (b) $\sigma = 170$ ps for ^{11}B's.

Table 4.1: Event selection criteria for the upstream drift chambers used by the program DCU320.

Limits on Upstream Parameters	
X_3 lower limit	13.2 cm
X_3 upper limit	16.0 cm
Y_3 lower limit	-18.7 cm
Y_3 upper limit	-14.0 cm
X_4 lower limit	12.0 cm
X_4 upper limit	16.0 cm
Y_4 lower limit	-21.0 cm
Y_4 upper limit	-14.5 cm
$\Delta(X_3,X_4)$ correlation	0.17 cm
$\Delta(Y_3,Y_4)$ correlation	0.12 cm
$DC3$ "darkness" lower limit	3.2
$DC4$ "darkness" lower limit	3.2

projectile suffered a small elastic collision between chambers $DC3$ and $DC4$ or passed outside the linear region of the last quadrupole were removed. A linear correlation existed between $\mathbf{X}_3$ and $\mathbf{X}_4$, and between $\mathbf{Y}_3$ and $\mathbf{Y}_4$, for good events. Unacceptable events were those for which the ordered pair ($\mathbf{X}_3$, $\mathbf{X}_4$) was more than 1.7 mm from the $\mathbf{X}_3$–$\mathbf{X}_4$ correlation (Figure 4.4a). Similarly, events for which the ordered pair ($\mathbf{Y}_3$, $\mathbf{Y}_4$) was more than 1.2 mm from the $\mathbf{Y}_3$–$\mathbf{Y}_4$ correlation were rejected (Figure 4.4b). Thirdly, events were discarded if more than one (1) track through $DC3$ and $DC4$ was possible or if a beam track had a "darkness" of less than 3.2. "Darkness" is a quantity, developed by Peter J. Lindstrom[43], with which one can evaluate the quality of a track in a drift chamber. This method will be discussed later (Section 4.2.2).

The bad upstream contamination constituted a large correction to the data. For data taken with the beam veto scintillator, DS, in the trigger, about 20% of the events were flagged. For data taken with the beam veto scintillator, DS, out of the trigger, only 10% of the events were flagged. If the ratio of bad upstream events to good events is time independent then the number of good events in a row should have a Poisson distribution. The number of good events logged between events labeled as bad upstream for two different settings of the beam collimating jaws is shown in Figure 4.5. The absence of a clean Poisson distribution in both figures implies time dependent behavior, that is, that beam structure was possible. The reduction of the ratio of flagged to good events with the closing of the beam collimator was a clear indication that the beam had a

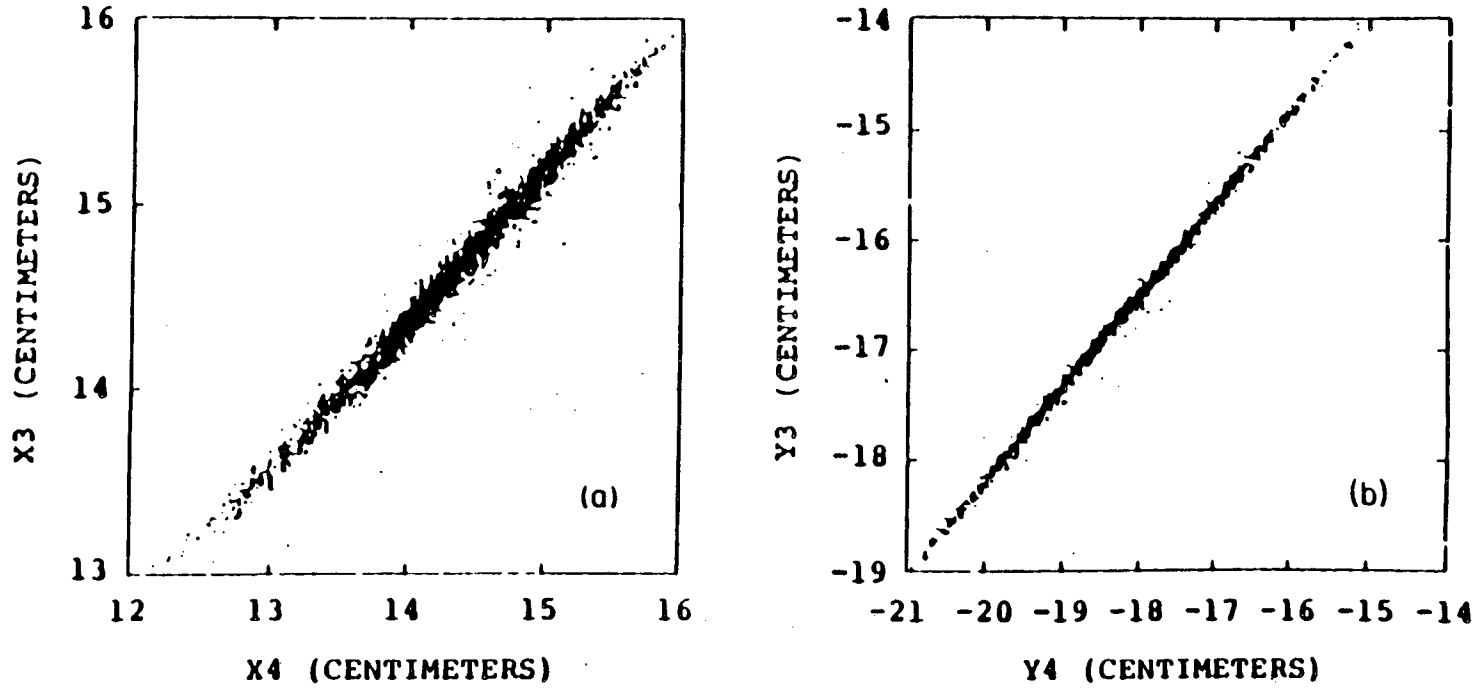

Figure 4.4: A plot of (a) the **X** coordinate in $DC3$ versus the **X** coordinate in $DC4$, and (b) the **Y** coordinate in $DC3$ versus the **Y** coordinate in $DC4$. Note the linear correlation between the variables in both plots.

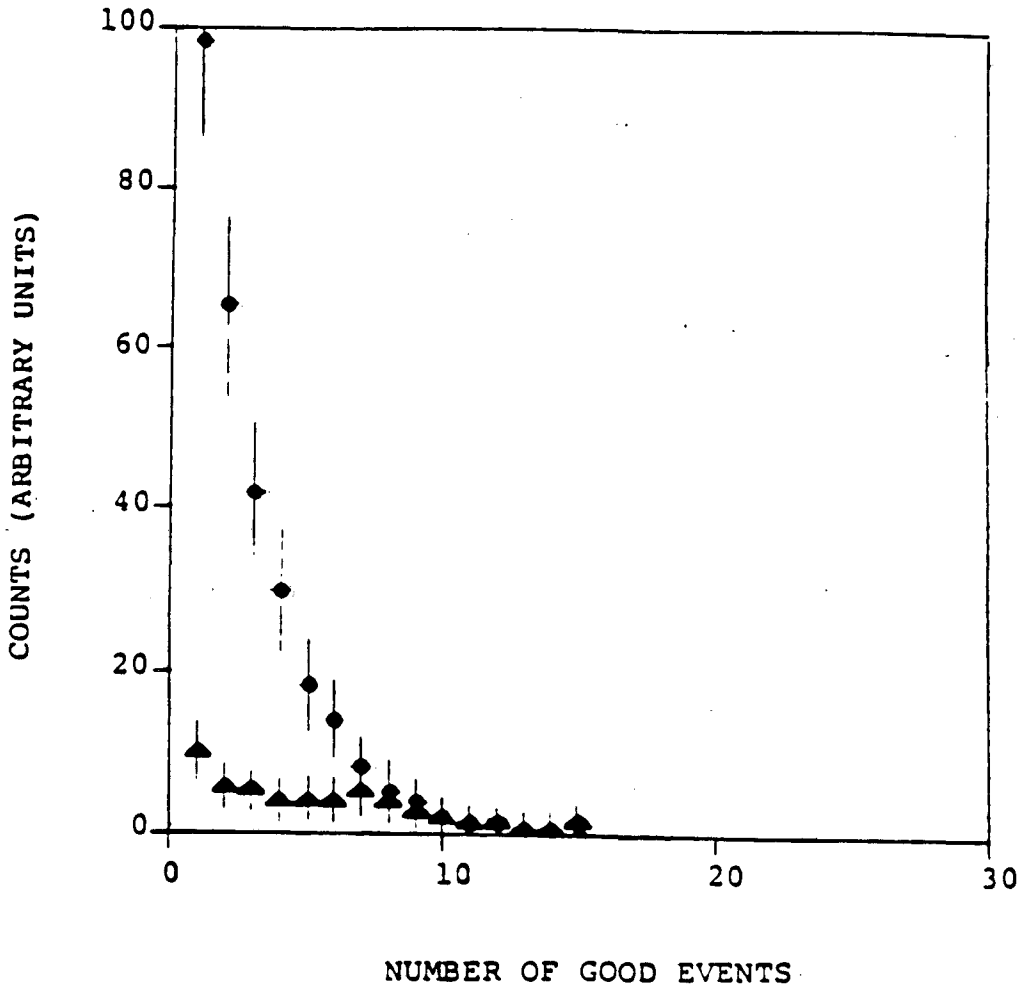

Figure 4.5: The number of good events logged between events which did not pass the cuts put on the upstream drift chamber data (Table 4.1) for a beam collimation jaw set completely open (•) and closed to 0.250 (▲).

halo. The above observations coupled with the high efficiencies for $DC3$ and $DC4$ implied that most bad upstream events were due to beam optics, rather than to mechanical malfunctions.

The efficiencies for $DC3$ and $DC4$, 98.1% and 99.5%, respectively, were determined using data taken with the beam veto scintillator, DS, out of the trigger. This data sample was then restricted to events for which the ADC values for the DS scintillator corresponded to a charge six (6). The number of events that were not flagged as bad upstream was divided by the sum of those events plus events that were labeled as bad upstream due to problems with "darkness", to determine the efficiencies of the upstream chambers.

4.2.2 Downstream Drift Chambers

Downstream tracks for primary fragments, or beam particles which missed the DS veto, were generated from their **X** and **Y** coordinates in $DC1$ and $DC2$. Each spatial coordinate was grossly determined by drawing an imaginary line between the predicted coordinates of the interaction in the target and the coordinates of each primary fragment in the TOF wall. The **X**-position of a primary fragment at the TOF wall was roughly determined by the **X**-position of the scintillator in the TOF wall that was fired. The **Y**-position of a primary fragment at the TOF wall was roughly determined by using the TDC signals from the scintillator that

was fired, as follows

$$Y_{TOF} = \left[\frac{TDC1}{TDC1 + TDC2}\right] \times L$$

The quantity L in the above equation is the length of the scintillator under examination. The line was constructed only for primary fragments with a charge greater than 0.6 which hit somewhere between scintillators 8 and 54, the range of the drift chambers. Any scintillator in the TOF wall that was fired was required to have output signals for both TDCs and both ADCs to meet the above requirements. Further, the sum of the outputs from the TDCs could not be greater than 10 ns, or 200 channels. No tracks were found if there were no matching hits in the TOF wall. At this point, the expected **X** and **Y** positions in $DC1$ and $DC2$ were determined from the intersection of the chambers and the imaginary line, discussed above. For the next iteration of those spatial coordinates the closest combination of wires in $DC1$ and $DC2$, within a ten (10) centimeter radius of the coordinates predicted, was located. The final positions were obtained using the output TDC values of the wires that were located. The outputs from the TDCs were converted to a distance channel by channel by using a look up table. A separate table for each pair of planes (S, T, and U) was developed for each chamber. There was a non-linear relation between time and distance (Figure 4.6). The single cell spatial resolution, typically having a $FWHM$ of 80 μm, was obtained from the width of the sum of TDC distances like those discussed above (Figure 4.7). Overall drift chamber resolution was worse, due mainly to

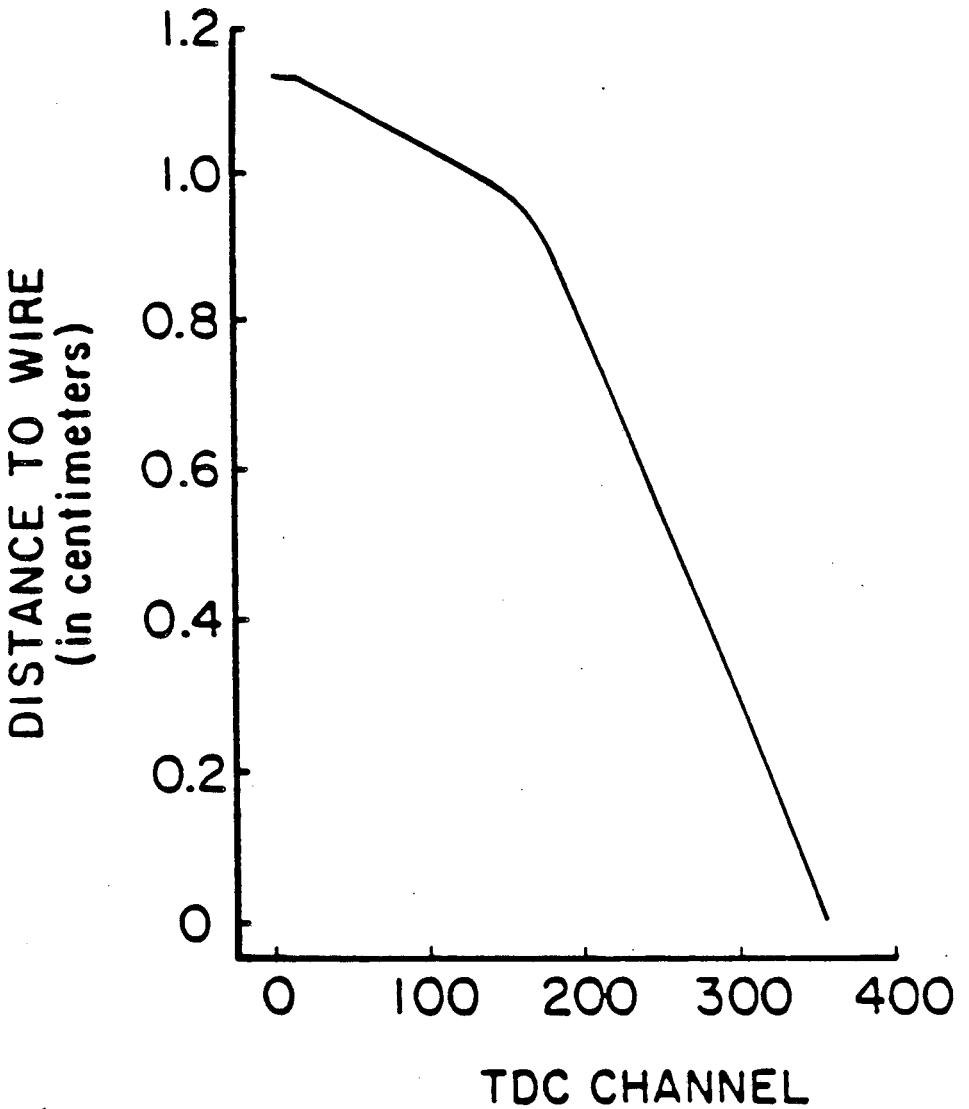

Figure 4.6: Drift distance versus TDC channel number for the S plane of $DC1$.

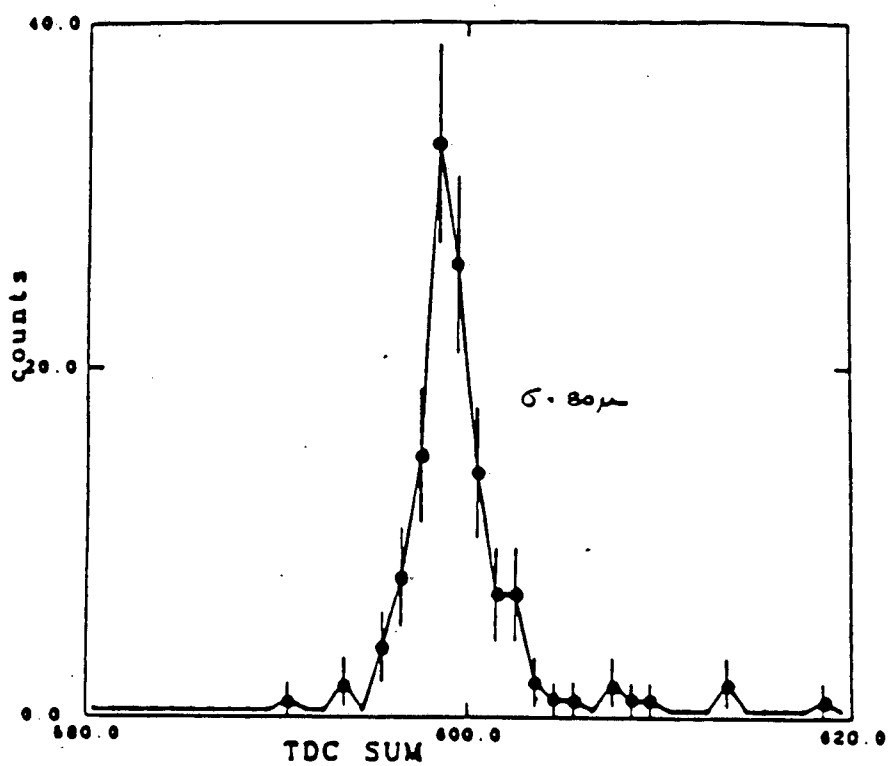

Figure 4.7: The single cell spatial resolution for beam particles in the S planes of $DC1$.

delta ray contamination. This will be discussed when we deal with the overall resolution of the experiment (Section 4.3).

The reason for taking three steps to find the track for each fragment was the large number of wires that were fired per particle in $DC1$ and $DC2$. The production of delta rays doubled the number of wires that were fired in $DC1$ and $DC2$ (Figure 4.8). The vast number of wires that fired made it difficult to distinguish the wires fired by the primary fragment from the wires fired by either delta rays or cross-talk in the electronics. The problem was successfully overcome by the introduction of the "darkness" quantity mentioned earlier.

The simplest procedure for track fitting would have been to minimize the sum of the differences squared from all 12 drift chamber planes. This least squares fit would not work for us since it uses all differences and heavily weights the largest differences. In the average track there were several spurious differences due to delta ray contamination. Thus we needed a method that would heavily weight small differences and ignore large differences. The method we chose was to maximize the "darkness" for a series of test tracks within a 10 cm radius of the predicted track.

The first step in calculating the "darkness" for a test track was to determine the predicted hit locations, $\overline{\xi}_n$, for each plane, n. The second step was to find the difference between the predicted location, $\overline{\xi}_n$, obtained from the test track, and the actual location, ξ_n, for each plane, n. The actual location for each plane

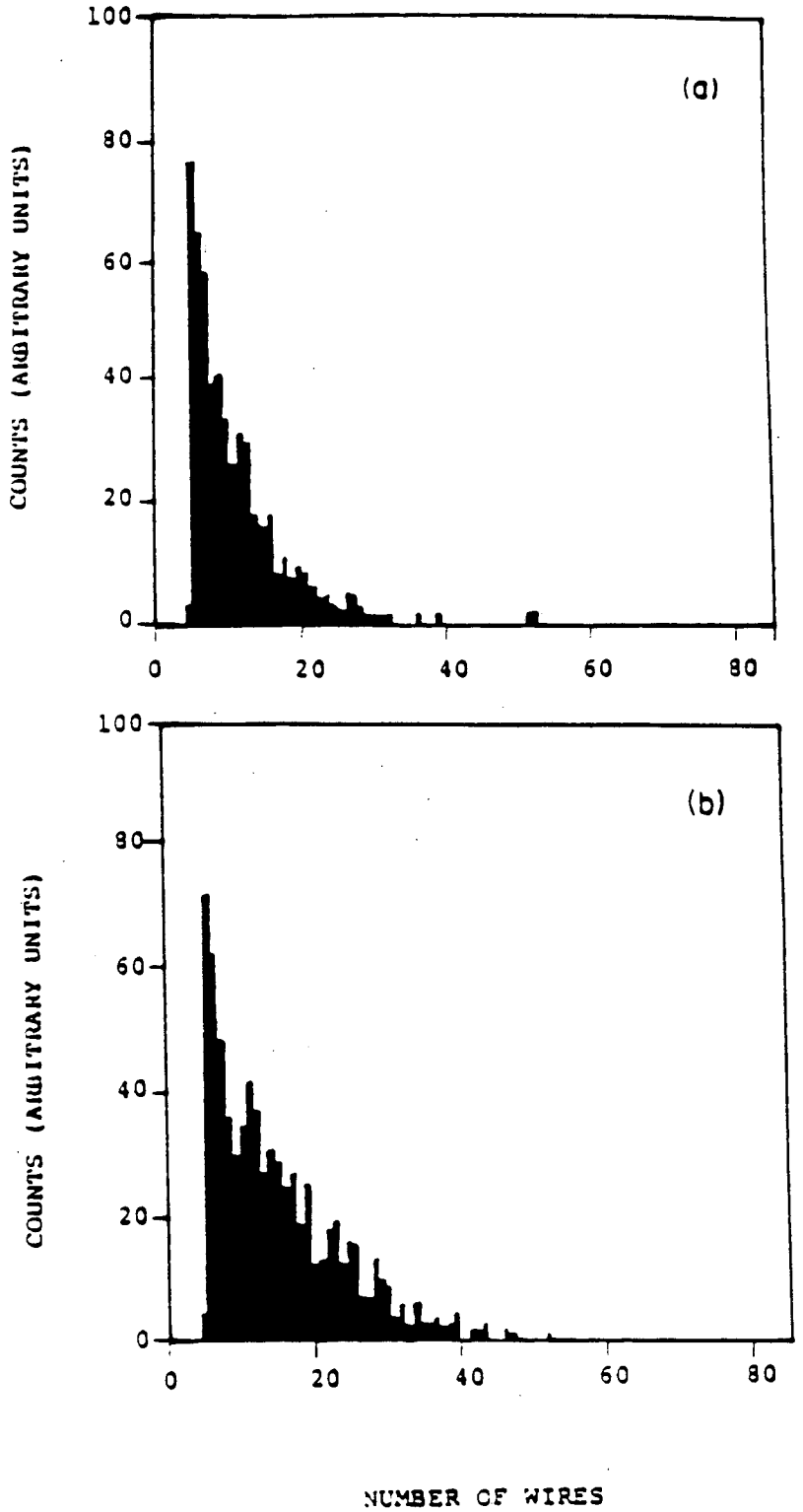

Figure 4.8: Number of wires firing in (a) $DC1$ and (b) $DC2$ for events with a single particle of charge $Z = 6$.

was determined by the number of the wire that fired, and the drift time of the TDC on that wire. Next a "darkness" was calculated for each of those differences from a Gaussian distribution with a standard deviation, $\sigma = 1\,\mathrm{mm}$. Finally the "darkness" of a chamber was obtained by summing the values from each plane in that chamber. Thus "darkness" can be defined as

$$\text{Darkness} = \sum_{n=1}^{6} \exp\left[\frac{-(\bar{\xi}_n - \xi_n)^2}{2\sigma^2}\right]$$

To illustrate the effect of this "darkness" maximization, consider the case with only two differences, x and y, with $y = D - x$. If $D < 2\sigma$ then "darkness" is maximized at $x = y = D/2$. If $D > 2\sigma$ then "darkness" is maximized at two places, one near $x = 0$, and the other near $y = 0$. Thus the parameter, σ, determines whether a differences is small enough to be included in the average or rejected. True hits are those produced by the passage of the primary fragment. They typically lay closest to the predicted position, while spurious hits from knock-on electrons were usually further away from the predicted position.

The efficiency of the downstream drift chambers, $DC1$ and $DC2$ was 0.924 ± 0.003 for charge $Z = 5$ particles, where the error quoted is a statistical standard deviation. As in the upstream case, "darkness" was employed to calculate these efficiencies. This calculation utilized a data set consisting of particles that struck the front TOF array and had an agreeing integral charge in the back TOF array. The efficiency of the downstream drift chambers was calculated by determining the percentage of these particles with good tracks. A good track was defined as

one which

1. pointed back to the target in the Y direction to within ± 1 mm,

2. yielded a correct mass number, $8.5 < A < 12.5$, and

3. had a "darkness" greater than three, meaning that at least four planes in both $DC1$ and $DC2$ returned reasonable values.

Since the data were normalized to a previously measured ^{11}B inclusive this efficiency did not affect the results.

More important was the proton efficiency in events where a ^{11}B was also detected. This efficiency was 0.79 ± 0.05 for charge $Z = 1$. The data set used required a ^{11}B to be detected with its track pointing back to the target within ± 1 mm. We also insisted that time of flight wall slats 19–39 have only charge $Z = 1$ in them. This data set had delta ray contamination as evidenced by the number of events with charge $Z = 1$ multiplicity greater than one (Table 4.2). To fit this distribution we assumed that the proton and delta ray multiplicity distributions were statistically independent. For the proton we used a Binomial distribution:

$$\begin{aligned} \Pr(proton\ in\ TOF) &= p \\ \Pr(no\ proton\ in\ TOF) &= q \equiv (1-p). \end{aligned}$$

Table 4.2: Charge $Z = 1$ multiplicity in TOF wall slats 19–39. These slats 19–39 had only charge $Z = 1$ in them. A ^{11}B was also detected with its track pointing back to the target within ± 1 mm. The predicted multiplicity assumes a Poisson distribution for the delta ray population.

Charge Z = 1 Multiplicity

Multiplicity	Data	Predicted
0	981	981.1
1	640	639.9
2	29	29.3
3	1	0.7
4	0	0.01

Here p is the mean number of protons per event. For the delta rays we used a Poisson distribution:

$$\Pr(r \textit{ delta rays in } TOF) = \frac{\lambda^r e^{-\lambda}}{r!}.$$

Here λ is the mean number of delta rays per event. Combining the two distributions we have:

$$\begin{aligned}
\Pr(mult = 0) &= qe^{-\lambda} \\
\Pr(mult = 1) &= q\lambda e^{-\lambda} + pe^{-\lambda} \\
&\vdots \\
\Pr(mult = n) &= q\frac{\lambda^n e^{-\lambda}}{n!} + p\frac{\lambda^{n-1} e^{-\lambda}}{(n-1)!}.
\end{aligned}$$

If two delta rays or a delta ray and a proton go into the same slat then that slat will have an invalid charge, and the event is discarded from our sample. We assume that the delta rays uniformly illuminate the TOF wall, and thus:

$$\Pr(mult = n, \textit{different slats}) = \frac{N!}{N^{n-1}(N-n+1)!} \cdot \Pr(mult = n),$$

where N is the total number of slats examined, and $n \geq 2$. The best fit values are $p = 0.376$ and $\lambda = 0.0500$. For multiplicity one events this gives 590.8 protons and 49.1 delta rays. So delta ray contamination is a 8% effect.

4.3 Overall Position Resolution

The major sources of error were multiple scattering and delta ray contamination. Both these effects decreased the effective position resolution of the drift chambers.

We computed this effective position resolution by examining the linear correlation between **Y** positions in all four drift chambers. The **Y** coordinates were used to remove the effect of the HISS dipole, making the tracks linear in this dimension.

We predicted the $DC1$ **Y** coordinate using the **Y** coordinates of $DC2$ and $DC3$, that is:

$$y_{1P} = a_0 + a_2 y_2 + a_3 y_3.$$

The (y_1, y_2) correlation removes the effect of target scattering, and the (y_1, y_3) correlation removes the effect of beam spot size and divergence. The (y_3, y_4) correlation was so strong that including y_4 would not have improved the prediction. If the errors in all chambers are independent we have:

$$\begin{aligned} e^2 \equiv (y_1 - y_{1P})^2 &= e_1^2 + a_2^2 e_2^2 + a_3^2 e_3^2 \\ e^2 &= (1 + a_2^2 + a_3^2) e_i^2 \qquad \text{for } Z = 6. \end{aligned}$$

Solving this for e_i, we have found the experimental resolution for charge $Z = 6$ particles in all chambers, 0.24 mm. Setting e_3 to that value and solving

$$e^2 = (1 + a_2^2) e_i^2 + a_3^2) e_3^2 \qquad \text{for } Z \neq 6$$

for e_i, we have the downstream resolutions of 0.24 mm for charge $Z = 5$, and 0.71 mm for charge $Z = 1$.

Chapter 5

Data Reduction

5.1 Momentum and Mass Reconstruction

At this point in the analysis, the information obtained from the TOF wall and the information from the drift chambers were sewn together for each primary fragment. Passing information between the different analysis programs was greatly simplified with those programs running under the LULU analysis shell.

The interaction position at the target and the **X** and **Y** coordinates in $DC1$ and $DC2$ were coupled with a set of Chebyshev coefficients to give the rigidity vector at the target, and length of the flight path from the target to the TOF wall for each fragment. The set of Chebyshev coefficients was obtained by numerically integrating a large number of sample trajectories through the field of the HISS magnet. The generation of the Chebyshev coefficients was such that the error was insignificant when compared to an uncertainty of 0.24 mm in the position of a particle in the drift chambers. The surface of the field of the HISS magnet was

mapped to an accuracy of one (1) Gauss at one (1) centimeter intervals. It was converted to a volume map using LaPlace's equation and the VAX 11/780 computer. A resulting resolution in rigidity of $\Delta R/R = 0.0042$ for beam particles was obtained. The rigidity was then used with the value of the charge as measured in the *TOF* wall to determine the momentum of each fragment (Table 5.1). In the projectile frame, the proton momenta were measured to standard deviations of 10 Mev/c parallel to the beam and 7.7 Mev/c transverse. The corresponding ^{11}B standard deviations were 105 Mev/c and 32 Mev/c. Although we only used transverse momentum in our analysis, for comparison we give the standard deviations of the components of transverse momentum parallel to, $\sigma(p_y)$, and perpendicular to, $\sigma(p_x)$, the dipole field.

$$\begin{aligned}
\sigma(p_y) &= 2.8\,\mathrm{MeV/c} && \text{proton} \\
\sigma(p_x) &= 9.5\,\mathrm{MeV/c} && \text{proton} \\
\sigma(p_y) &= 10.7\,\mathrm{MeV/c} && {}^{11}\mathrm{B} \\
\sigma(p_x) &= 45.9\,\mathrm{MeV/c} && {}^{11}\mathrm{B}
\end{aligned}$$

If the errors were independent and gaussian then

$$\sigma(p_\perp) = \sqrt{\frac{\sigma(p_x^2) + \sigma(p_y^2)}{2}},$$

but this is not the case.

The velocity for each fragment was similarly obtained by dividing the calculated path lengths by the adjusted time of flight values. The mass, m, of each

fragment was then determined using the following formula

$$m = \frac{R \cdot Z \cdot c}{L} \times \left[T^2 - \left(\frac{L}{c}\right)^2\right]^{\frac{1}{2}}$$

where R was the rigidity of the fragment, Z was the charge of the fragment, L was the path length, and T was the adjusted time of flight. The system resolved protons with a standard deviation of 0.093 mass number, and ^{11}B's with a standard deviation of 0.19 mass number (Figure 5.1).

5.2 Aperture of the HISS Spectrometer

All ^{11}B's were in the experimental aperture, but this was not the case for protons. Only 72 ± 19 % of the protons from the H(^{12}C,^{11}B+p)X reaction were within the aperture. The aperture was limited by the second downstream drift chamber, and at low velocity by the region of phase space covered by the momentum reconstruction Chebyshev coefficients.

The proton aperture was a function of p_x, p_y, and p_z simultaneously. The aperture for p_y was geometric because the HISS dipole field was in that direction and little bending occurred outside the x-z plane. In the bending plane the aperture had a complex shape (Figure 5.2).

Table 5.1: The detector systems and the physical quantities computed from them.

Measured Quantities

1. Drift Chambers and Magnet

   (a) Rigidity $= R = B \cdot r = \frac{p}{Z}$

   (b) Path Length $= L$

2. Scintillator Wall

   (a) Time of Flight $= T$

   (b) Charge $= Z$

Computed Quantities

1. $\beta = \frac{L}{Tc}$

2. $\gamma = \frac{1}{\sqrt{1-\beta^2}}$

3. Momentum $= p = RZ$

4. Mass $= m = \frac{RZ}{\beta\gamma}$

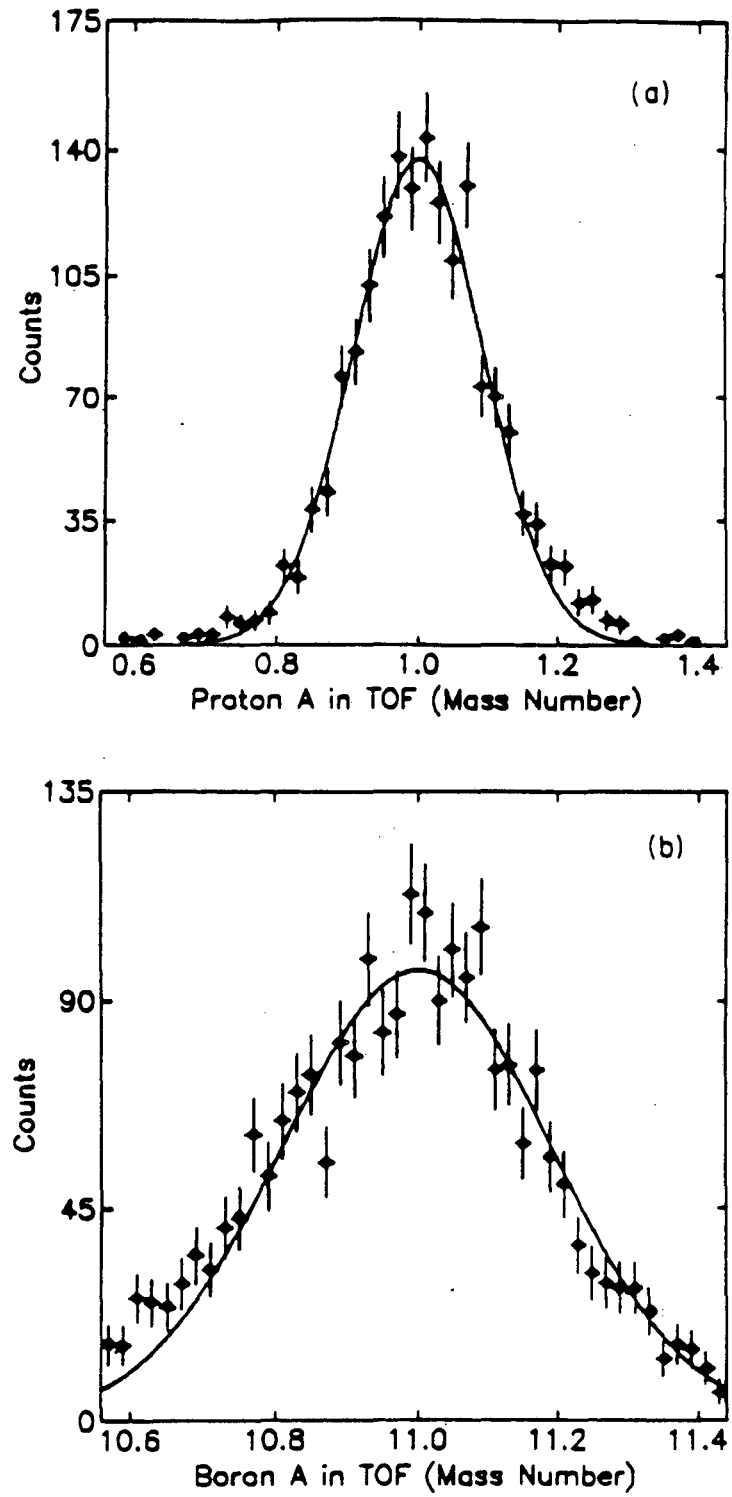

Figure 5.1: Mass distribution for protons and ^{11}B's. The data are fit with a Gaussian of (a) $\sigma = 0.093$ mass number for protons, and (b) $\sigma = 0.19$ mass number for ^{11}B's.

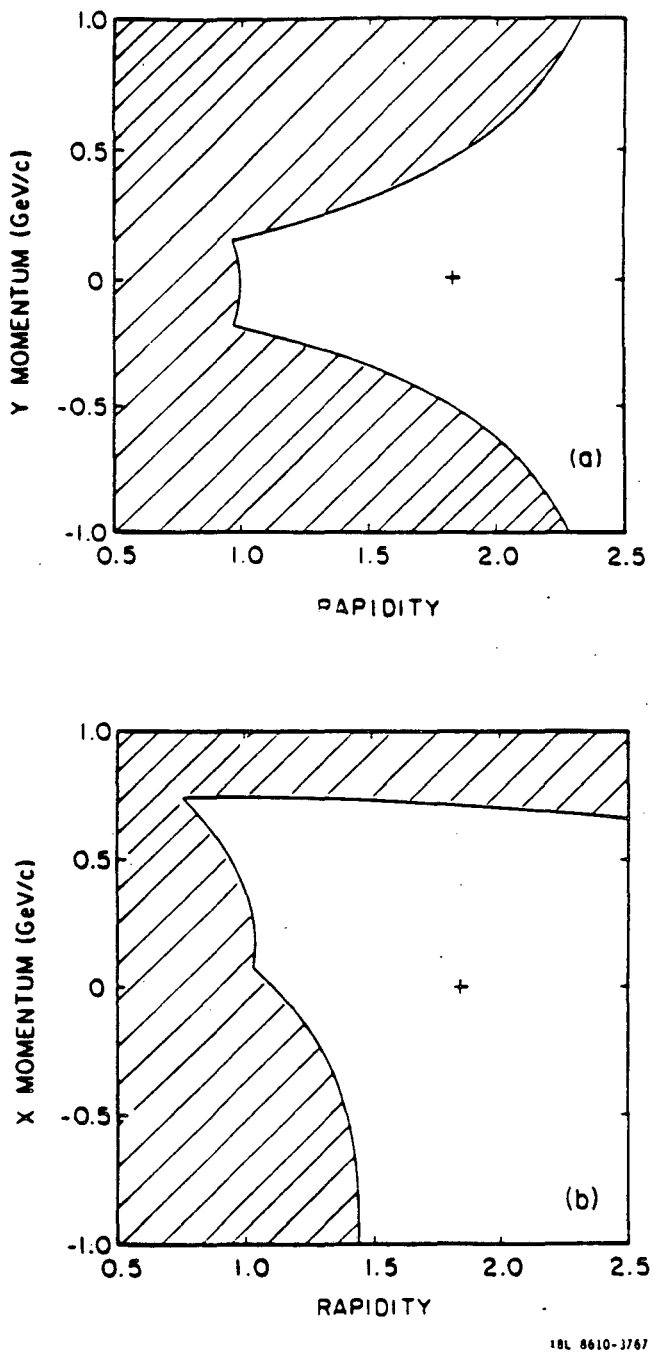

Figure 5.2: Experimental aperture for protons shown as a function of rapidity and perpendicular momentum (a) parallel and (b) perpendicular to the dipole field. Drift chamber $DC2$ and the momentum reconstruction code were the limits to the acceptance. The crosses represent beam velocity protons. All ^{11}B were in the aperture.

Chapter 6

Data Analysis and Results

6.1 Introduction

We have measured two processes, (^{12}C,^{11}B+x) and (^{12}C,^{11}B+p). Only the first was entirely within the experimental aperture so (^{12}C,^{11}B+x) experimental cross sections were normalized to the ^{11}B inclusive measurements[15] of 30.9 ± 3.4 mb for the H target and 53.8 ± 2.7 mb for the C target. This allowed us to extract cross sections for the (^{12}C,^{11}B+p) process.

The projectile excitation energy spectra for (^{12}C,^{11}B+p) show two components, a low excitation energy peak and a long tail (Figure 6.1). Experimental energy resolution for this reaction, a standard deviation of 6 MeV, precludes the identification of individual resonance peaks. Since we expect nucleon-nucleon scattering to be a major component of this cross section we next examine the proton spectra. These (Figure 6.2) display three features. (1) A ridge appears in the data along the line of nucleon-nucleon quasi-elastic scattering. The width of

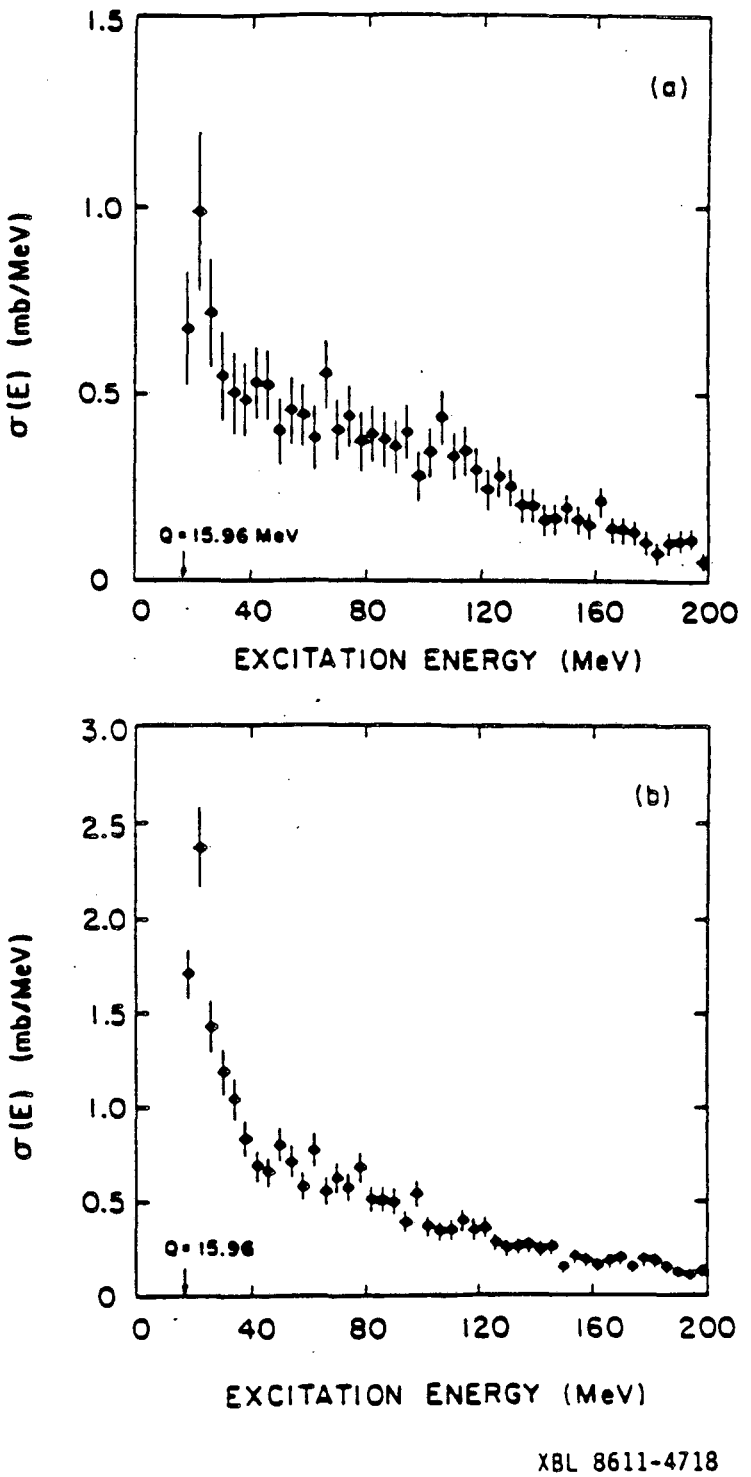

Figure 6.1: Excitation energy for the p,^{11}B pair from (a) a H target and (b) a C target. Excitation energy is determined by finding the invariant mass of the projectile fragments and subtracting the ^{12}C rest mass.

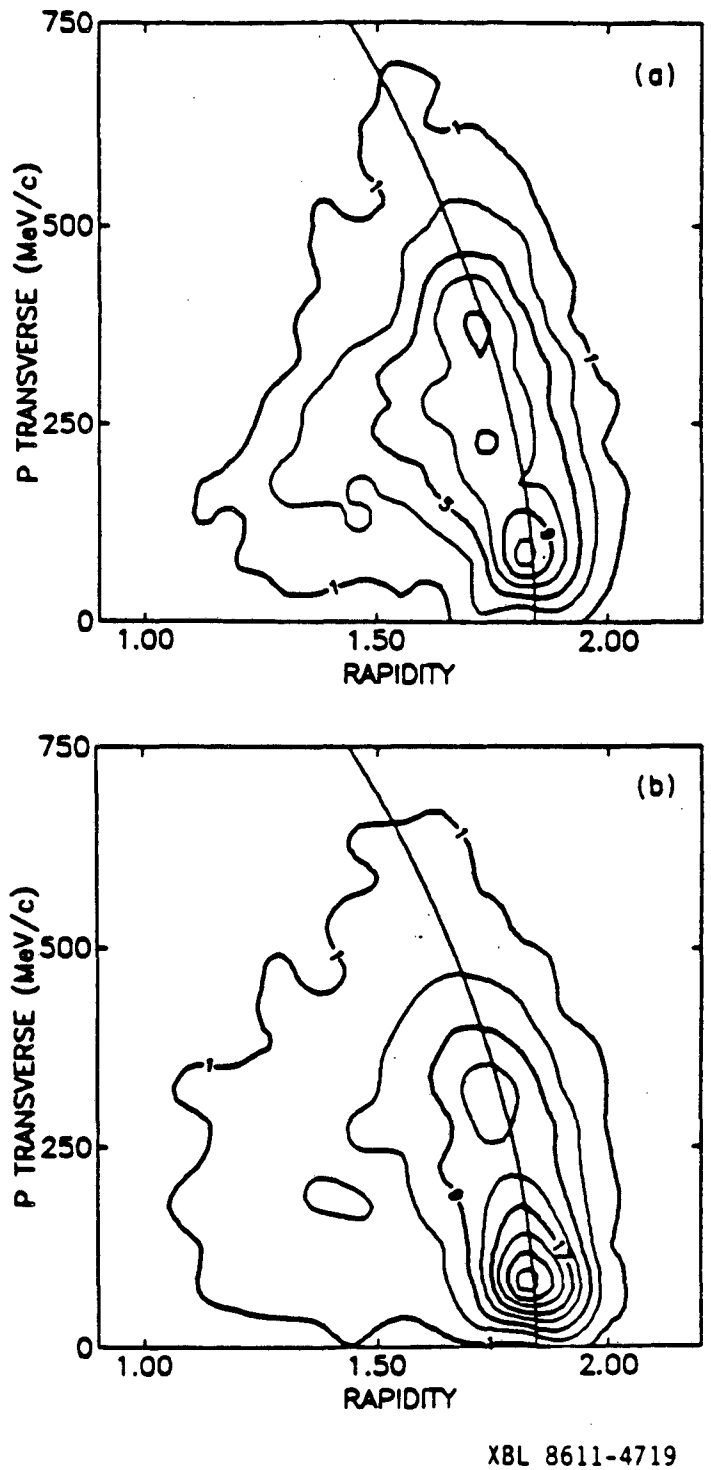

Figure 6.2: Rapidity versus transverse momentum for protons from (a) a H target and (b) a C target. The contours are measured in units of 10^{-2}mb·rapidity^{-1}·(MeV/c)$^{-1}$. The line shows the location of nucleon-nucleon quasi-elastic scattering.

the ridge is a measure of the initial Fermi motion of the scattered nucleons. (2) There is also a plateau at lower rapidity. The large rapidity loss indicates that these are inelastic events. (3) A sharp peak appears at 100 MeV/c transverse momentum and beam rapidity. This is due to a low energy and momentum transfer process, and is much stronger for the C target.

The ^{11}B spectra (Figure 6.3) display only a single peak, suggesting that the ^{11}B is indeed a minimally interacting participant to the reaction. The presence or absence of a simultaneously detected proton made no difference to the shape of the ^{11}B spectra, therefore we show only ^{11}B inclusive spectra.

It is useful to compare these proton and ^{11}B cross sections with free nucleon-nucleon scattering. For comparison to our data we used a Monte Carlo cascade model[19] with π production mediated through the $\Delta(1232)$ resonance, the dominant inelastic mechanism. This model is a sum of free nucleon-nucleon processes, and any differences between it and the data can be attributed to collective effects.

In what follows we will first discuss the cascade model and the modifications made to it. We then will compare the model and data for the ^{11}B inclusive spectra. Next a comparison for the proton exclusive spectra will be made. Finally we will discuss that part of the exclusive spectra which can not be fit by the cascade model.

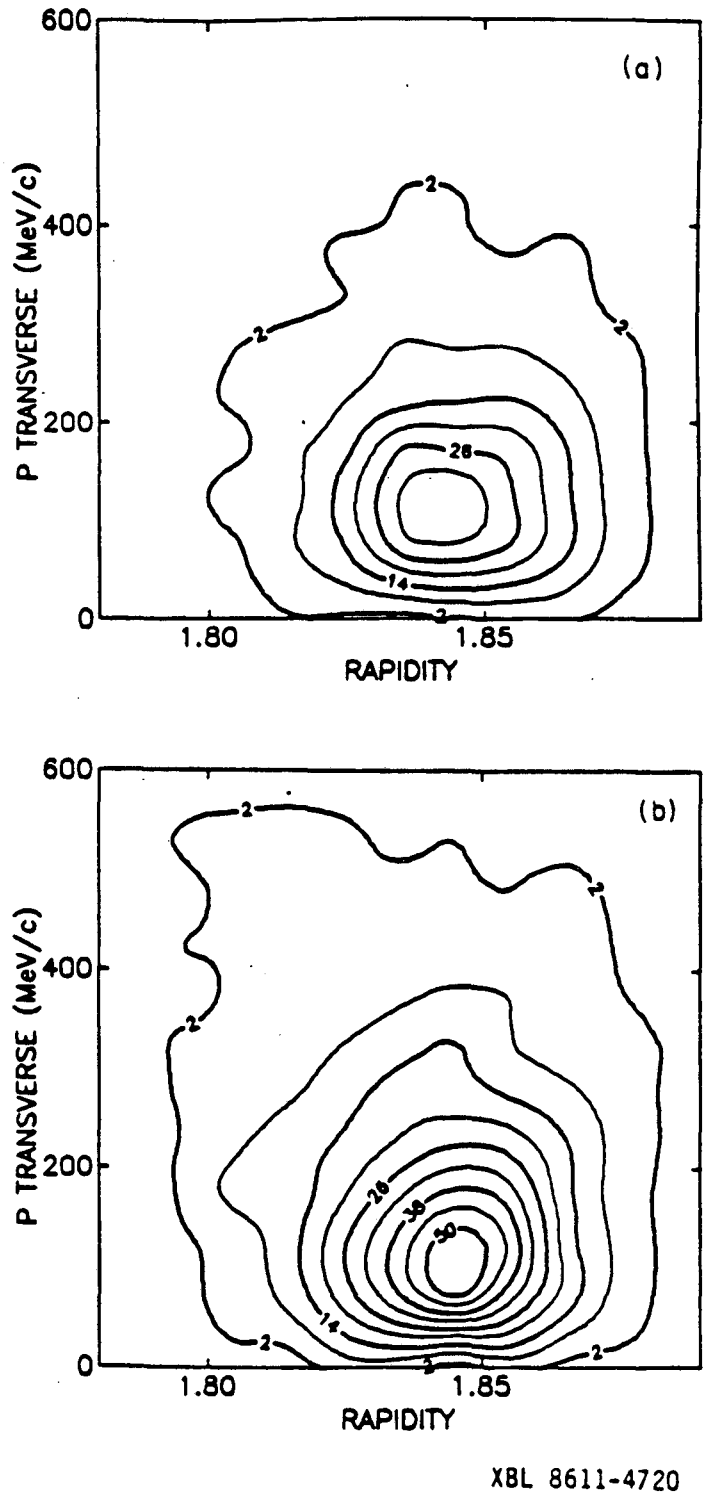

Figure 6.3: Rapidity versus transverse momentum for ^{11}B inclusive from (a) a H target and (b) a C target. The beam rapidity was 1.84. The contours are measured in units of 10^{-1}mb·rapidity^{-1}·(MeV/c)$^{-1}$.

6.2 Monte Carlo Cascade Model

[19] We now discuss the changes[44] to the Cugnon cascade model alluded to earlier (Section 2.3.2) and point out the impact these changes have on the comparison to our data. The model has no binding energy, so the nuclei expanded with time. Freezing the nuclear distribution until an interaction occurs stops this. To better reflect knowledge about $\Delta(1232)$ production gained from proton-proton scattering[32], two changes were made. The Δ was given an exponential lifetime, and the functional form of the Δ production cross section was changed. Of these changes only the latter significantly altered the model results for our case.

Under the original assumption of isotropic Δ production, only 20% of the protons from the decay of Δ's were within the detector aperture. Using a production cross section of $\sigma(t) \propto e^{bt}$ where t is the Mandelstam t, and $b = 10.11\,\mathrm{GeV}^{-2}$[32], 53% of the protons from the decay of Δ's are within the aperture. If the isotropic production cross section is used, the cascade model cannot be reconciled with the the ratio of (^{12}C,^{11}B+p) to (^{12}C,^{11}B+x) measured. Finally, to better fit our data we use the Fermi momentum as an adjustable parameter.

The major problem in comparing these cascade model results with the data is that the cascade model does not explicitly account for isospin. A significant fraction of the Δ production channels involve charge exchange. If such a reaction

leaves a neutron in the projectile frame it is indistinguishable from a ^{11}B+p event with the proton outside our aperture. Thus, for a valid comparison, the model predictions for the ^{11}B inclusive cross sections and the (^{12}C,^{11}B+p) cross sections in aperture must be consistent with the data. Fortunately charge independence holds well in this energy region[32], and this reaction channel is dominated by single nucleon-nucleon interactions, so it is possible to separate the cascade model results into components which can be weighted by isospin branching ratios (Appendix B).

To derive cross sections from the cascade model results we found the fraction of the interactions that scattered only one projectile nucleon. Any number of target nucleons were allowed to scatter. We then multiplied that fraction by the total fragmentation cross section to obtain a single nucleon scattering cross section. Using an experimentally derived total fragmentation cross section of 250 ± 10 mb for a H target[45] the cascade model predicts 100.4 ± 4.1 mb for single nucleon scattering with a H target. What follows is an analysis for a H target; the C target analysis is similar, and both results are shown in Table 6.1. Assuming the scattered projectile nucleon is a proton 50% of the time the cascade cross section for producing ^{11}B's is 50.2 ± 2.0 mb, significantly higher than the previously measured value of 30.9 ± 3.4 mb[15] or the abrasion model value of 34.4 mb[7]. We conclude that even at this basic level nucleus-nucleus collisions cannot be considered as just a sum of free nucleon collisions.

Table 6.1: Monte Carlo cascade model[19] cross section predictions for ^{11}B+x and ^{11}B+p production from H and C targets. These are compared to data[15] and to a purely geometric calculation[7], the abrasion step of the abrasion-ablation model. From isospin considerations, for the H target, 1/4 of the proton-proton collisions resulting in Δ's in the target also produce a proton in the projectile, while 11/12 of the projectile Δ's decay into a proton. For the C target 3/8 of the proton-nucleon collisions resulting in a target Δ leave a proton in the projectile, while 17/24 of the projectile Δ's decay into a proton. Also quasi-elastic charge exchange is 2.86 ± 0.65 %[32] of quasi-elastic scattering from the C target. The cross sections have been normalized to experimentally derived total fragmentation cross sections of 250 ± 10 mb for a H target and 810 ± 20 mb for a C target[45].

Monte Carlo cascade model process cross sections	H Target (mb)		^{12}C Target (mb)	
	^{11}B+x	^{11}B+p	^{11}B+x	^{11}B+p
Nucleon-nucleon elastic scattering	25.6±1.1	25.6±1.1	33.99±0.93	33.02±0.93
Δ production in the projectile	12.30±0.52	11.28±0.48	23.43±0.67	16.59±0.47
Δ production in the target	12.30±0.52	3.08±0.13	23.43±0.67	8.79±0.25
Cascade model total	50.2±2.0	39.9±1.6	80.8±2.1	58.4±1.5
Measured total	30.9±3.4	—	53.8±2.7	—
Abrasion model total	34.4±1.4	—	74.9±1.8	—

This cross section can be further separated into: (1) quasi-elastic scattering, 25.6 ± 1.1 mb, (2) Δ production in the projectile, 12.30 ± 0.52 mb, and (3) Δ production in the target, 12.30 ± 0.52 mb. From isospin considerations, 1/4 of the proton-proton collisions resulting in Δ's in the target leave a proton in the projectile, while 11/12 of the projectile Δ's decay into a proton. The ^{11}B+x and ^{11}B+p cascade model cross sections for both targets are shown in Table 6.1.

6.3 ^{11}B Inclusive Spectra

In the Monte Carlo cascade model the ^{11}B has a projectile frame momentum equal and opposite to the initial Fermi momentum of the scattered proton, so its spectrum (Figure 6.4) has the same shape for both targets. These spectra are inclusive since what happens to the proton after scattering is immaterial to the ^{11}B momentum distribution. To obtain the best fit to the data we allowed both the Fermi momentum and the cross section to vary in a χ^2 fit to the transverse momentum distribution.

The integral cross sections obtained from the fit were 18.6 ± 1.3 mb for the H target and 26.0 ± 1.7 mb for the C target. These are 60.2 ± 2.9 % and 48.3 ± 1.9 % of the data respectively. The difference is due to a tail at high transverse momentum which we excluded from the fit. The tail is more pronounced in the C target data and is absent from the model.

The Fermi momenta obtained from the fit were 160 ± 11 MeV/c for the H

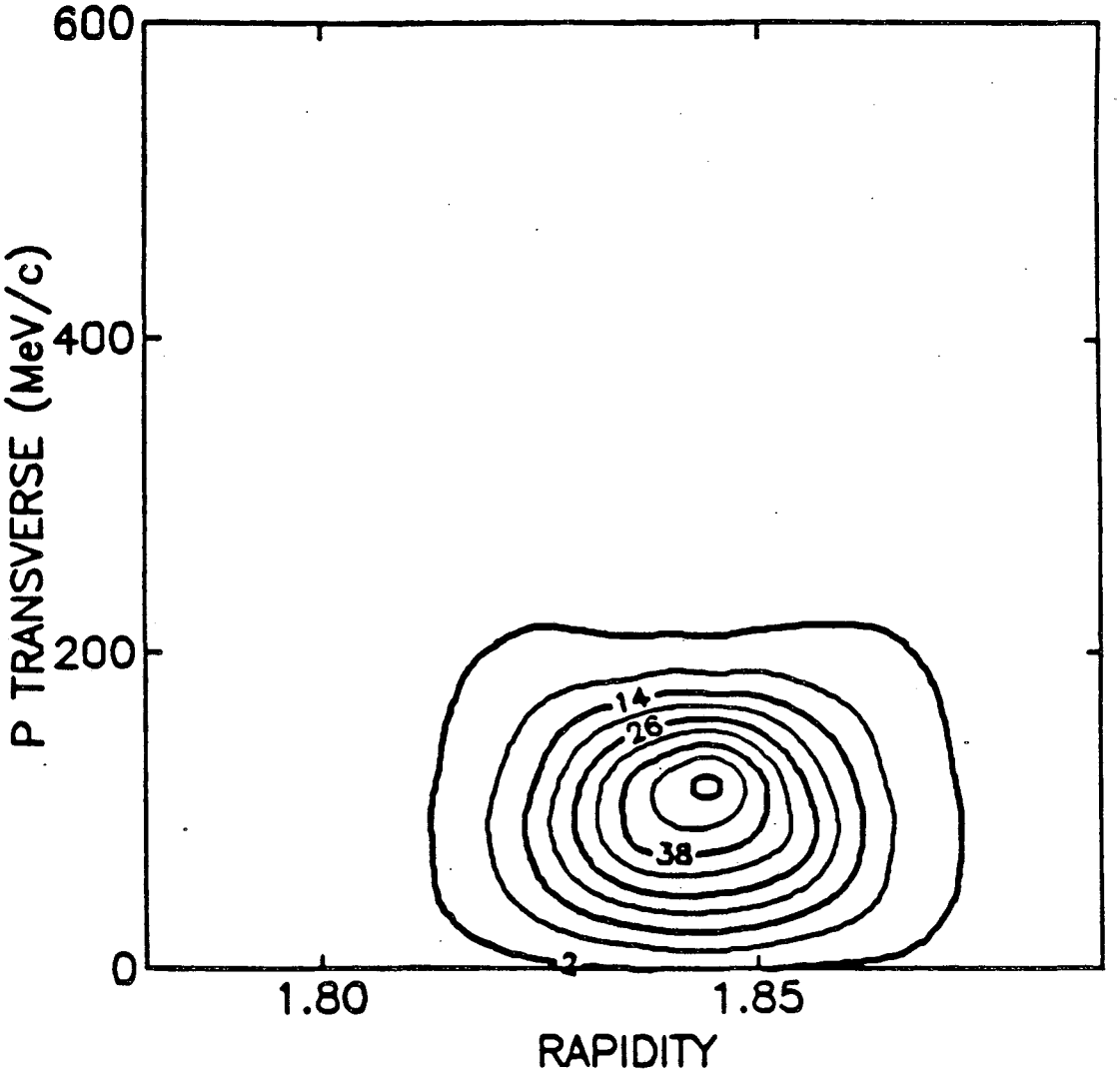

XBL 8611-4722

Figure 6.4: Rapidity versus transverse momentum for ^{11}B inclusive from the Monte Carlo cascade model for a H target. The data (Figure 6.2) has a high transverse momentum tail this model lacks. The contours are measured in units of 10^{-1}mb$\cdot$rapidity$^{-1}\cdot$(MeV/c)$^{-1}$.

target and 160 ± 17 MeV/c for the C target. This differs from previous measurements of 221 MeV/c, derived from electron scattering [46] and 182 ± 5 MeV/c derived from fragment momentum distributions[16]. The difference between the latter value and our measurements is surprising since both use momentum distributions to derive the Fermi momentum. However our measurement is derived from the transverse momentum distribution, while the other is derived from the longitudinal momentum distribution. Detector resolution made it meaningless to use our ^{11}B longitudinal momentum for comparison. However it is possible to extract the Fermi momentum from the proton longitudinal momentum (Section 6.4) and get a result that is consistent with the 182 ± 5 MeV/c measurement. This difference between the Fermi momenta determined from longitudinal and transverse momenta is inconsistent with the usual model of the nucleus as a free Fermi gas. It has been suggested[47] that this difference is due to the peripheral nature of the reaction, but no quantitative predictions have been made.

Another model[48] employs the sudden approximation and shell model wave functions. The result quoted, $\sigma = 80.2$ Mev/c, is the standard deviation of an exponential momentum distribution along any one of the three spatial axes. To compare to this value, we use the statistical relation[49] $\sigma^2 = p_F^2/5$ to obtain a comparable Fermi momentum, $p_F = 179$ MeV/c. Note that this model predicts an isotropic momentum in contradiction to the data.

6.4 Proton Exclusive Spectra

The cascade model proton spectra (Figure 6.5) display two of the features that are in the proton data, the ridge and plateau. The ridge is due to nucleon-nucleon quasi-elastic scattering. The width of the ridge is dependent on the initial Fermi momentum. This is a longitudinal momentum measurement and should be equal to the previously measured 182 MeV/c[16]. The Fermi momenta fits were 190 ± 11 MeV/c for the H target and 190 ± 25 MeV/c for the C target. The low rapidity plateau is populated by inelastic scattering associated with π production. The peaks at 100 MeV/c transverse momentum do not appear, and the plateau shape is not duplicated well. These will be discussed later (Section 6.5). These spectra have been fit to the data, and we discuss the fit and its implications next.

Having corrected the cascade model for charge exchange effects (Section 6.2) we can now compare the model prediction for (^{12}C,^{11}B+p) in the detector aperture with the exclusive data. As with the ^{11}B inclusive data, scaling was required to get a good χ^2 fit. We found it necessary to vary both the quasi-elastic and inelastic cross sections as well as the Fermi momentum in fitting the cascade model proton spectra to the data. It was necessary to multiply the quasi-elastic components by 0.34 ± 0.10 % for the H target and by 0.34 ± 0.07 % for the C target. The inelastic components were scaled by 0.70 ± 0.16 % for the H target and by 0.95 ± 0.15 % for the C target. Thus the quasi-elastic component is smaller

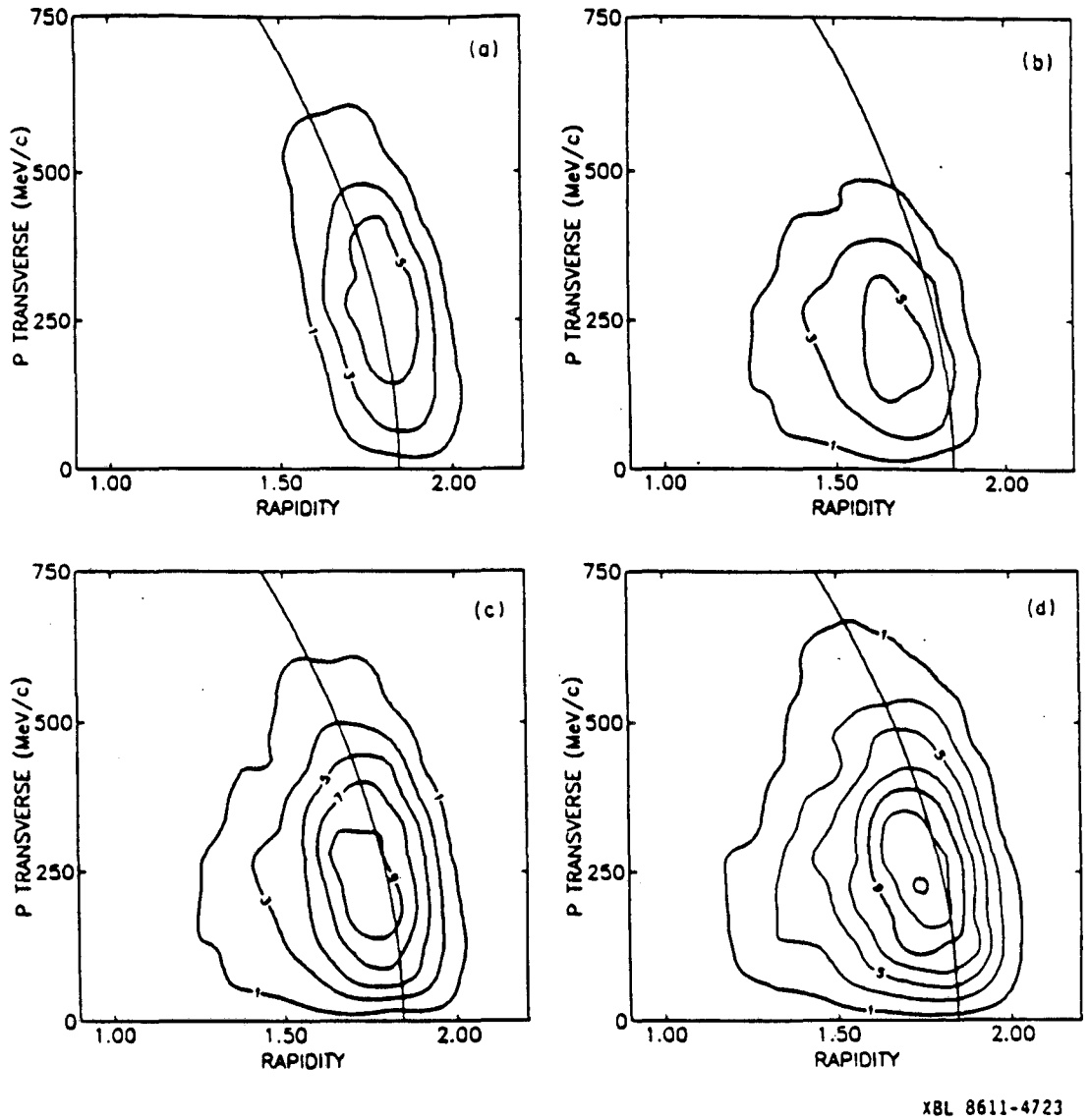

Figure 6.5: Rapidity versus transverse momentum for protons from the Monte Carlo cascade model for (a) quasi-elastic scattering and (b) inelastic scattering with π production from the H target. Also shown are plots summing both processes from (c) H and (d) C targets. These should be compared with the data (Figure 6.2). The contours are measured in units of 10^{-2}mb·rapidity^{-1}·(MeV/c)$^{-1}$.

by a factor of three than what would be expected from free nucleon-nucleon scattering, while the inelastic component is consistent with the prediction. This suppression of the quasi-elastic component shows clearly that the cascade model is not a valid microscopic description of the interaction process.

The fits were to the $-t$ distribution excluding the low momentum transfer peak (Figure 6.6). Here t is a modified Mandelstam $t = (\mathbf{p}_1 - \mathbf{p}_3)^2$, where $\mathbf{p}_1 = \mathbf{p}_{beam}/12$ before the reaction, and $\mathbf{p}_3 = \mathbf{p}_{proton}$ after the reaction. The reduced mass of a nucleon within a ^{12}C nucleus is accounted for by using $\mathbf{p}_{beam}/12$. All $\mathbf{p}$ are four-vectors. The modified Mandelstam t allows comparison to (p,p) scattering data. A general check of the fit can be made by comparing the cascade model cross sections for (^{12}C,^{11}B+p) in the aperture with the measured total cross section excluding the cross section in the peak (Section 6.5). This is done in Table 6.2.

Having fit the (^{12}C,^{11}B+p) spectra in the aperture we can estimate the aperture corrected (^{12}C,^{11}B+p) cross sections by using the scaled cascade model values and the measured peak cross section. We can also determine the cascade model (^{12}C,^{11}B+x) cross section. This latter cross section must be consistent with the ^{11}B inclusive data which was not used in the fit. The scaled cascade model plus peak underpredicts by $14 \pm 18\,\%$ for the H target and overpredicts by $12 \pm 15\,\%$ for the C target. These results are summarized in Table 6.3.

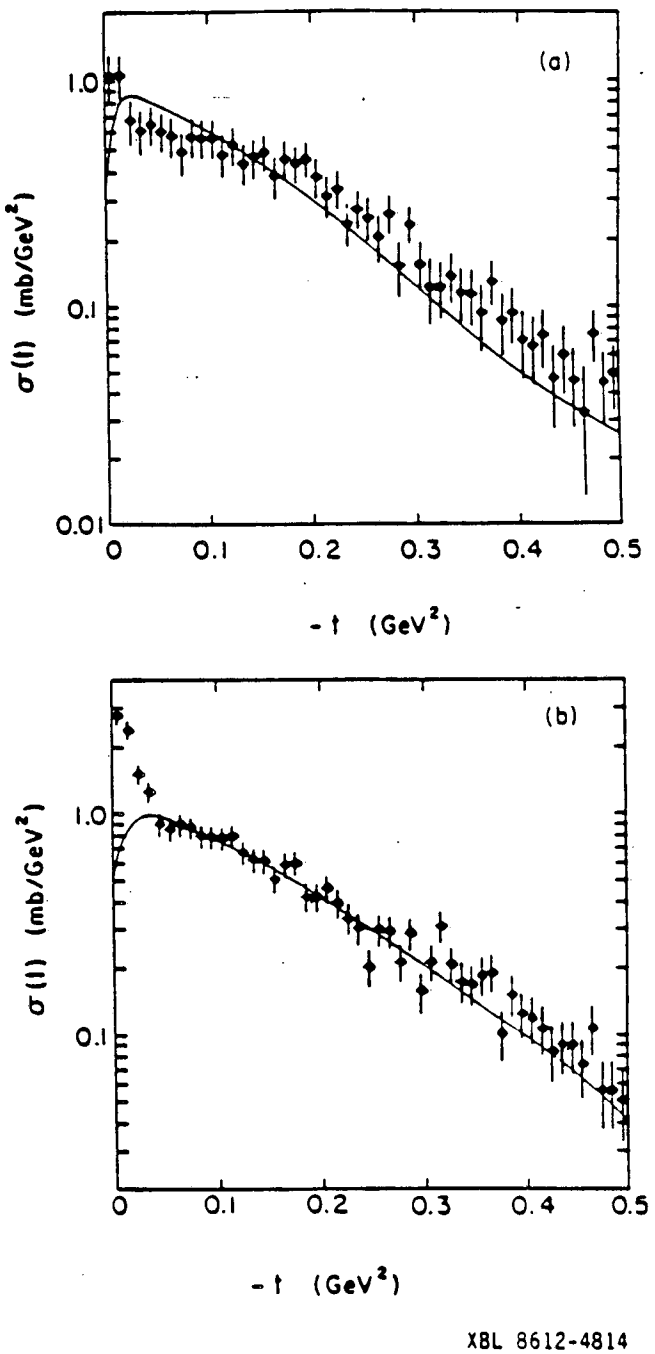

Figure 6.6: Monte Carlo cascade model normalized to the data as a function of $-t$ for (a) H and (b) C targets. Here t is a modified Mandelstam $t = (\mathbf{p}_1 - \mathbf{p}_3)^2$, where $\mathbf{p}_1 = \mathbf{p}_{beam}/12$ before the reaction, and $\mathbf{p}_3 = \mathbf{p}_{proton}$ after the reaction. The reduced mass of a nucleon within a ^{12}C nucleus is accounted for by using $\mathbf{p}_{beam}/12$. All $\mathbf{p}$ are four-vectors. The lines are natural spline fits to the normalized Monte Carlo cascade model.

Table 6.2: Monte Carlo cascade model[19] cross section predictions for $^{11}B+p$ production in the proton aperture from H and C targets. These are compared to the data with the low momentum and energy transfer peak removed.

Monte Carlo cascade model process cross sections in aperture	H Target (mb)		^{12}C Target (mb)	
	Unscaled	Scaled	Unscaled	Scaled
Nucleon-nucleon elastic scattering	21.16±0.88	7.3±2.1	26.02±0.75	8.7±1.9
Δ production in the projectile	8.98±0.39	6.3±1.4	7.76±0.25	7.3±1.4
Δ production in the target	2.53±0.11	1.77±0.40	4.70±0.15	4.45±0.84
Model total	32.7±1.3	15.3±2.7	38.5±1.0	20.5±2.9
Measured total - peak	—	15.8±3.4	—	21.4±2.0

Table 6.3: Aperture corrected cross section for ^{11}B+x and ^{11}B+p production from H and C targets. The peak cross section is measured. The quasi-elastic and inelastic cross sections are cascade model values scaled to fit the data inside the proton aperture.

Aperture corrected process cross sections	H Target (mb)		^{12}C Target (mb)	
	^{11}B+x	^{11}B+p	^{11}B+x	^{11}B+p
Low momentum transfer peak	0.81±0.45	0.81±0.45	4.50±0.67	4.50±0.67
Nucleon-nucleon elastic scattering	8.8±2.5	8.8±2.5	11.4±2.5	11.1±2.4
Δ production in the projectile	8.6±1.9	7.9±1.8	22.2±3.4	15.7±2.4
Δ production in the target	8.6±1.9	2.16±0.48	22.2±3.4	8.3±1.3
Aperture corrected total	26.7±4.6	19.7±3.4	60.3±7.3	39.7±4.5
Measured total	30.9±3.4	—	53.8±2.7	—

6.5 Residual Peak and Inelastic Cross Section

Having normalized the cascade model we now focus on the unexplained regions of the data by subtracting the cascade model. The subtracted spectra (Figure 6.7) show two features: residual inelastic cross section in the low rapidity region and the low momentum transfer peaks. The large rapidity loss of the residual inelastic cross section indicates that other more highly inelastic processes must contribute to the inelastic region, such as $pp \rightarrow pp\pi^+\pi^-$. This is 6 % of the free proton-proton total cross section[32].

The low momentum transfer peaks that remain are 0.81 ± 0.45 mb for the H target and 4.50 ± 0.67 mb for the C target. These cross sections were determined by subtracting the normalized cascade model t spectra from the data t spectra (Figure 6.6). Here t is the previously defined modified Mandelstam t (Section 6.4).

Such peaks do appear in p-nucleus scattering. The C(p,p)X cross section (Figure 6.8)[50] is shown as a function of the Mandelstam t. This plot can be fit by the sum of two exponentials, e^{86t} and $e^{5.2t}$. These can be interpreted as diffraction[51] from objects of radii 3.66 fm and 0.90 fm respectively, i.e. the C target nucleus and a target nucleon. Alternatively in the Glauber model[52] the low t peak is explained as the proton diffracting elastically off the target, while the rest of the cross section is due to excitations of the target. To allow such

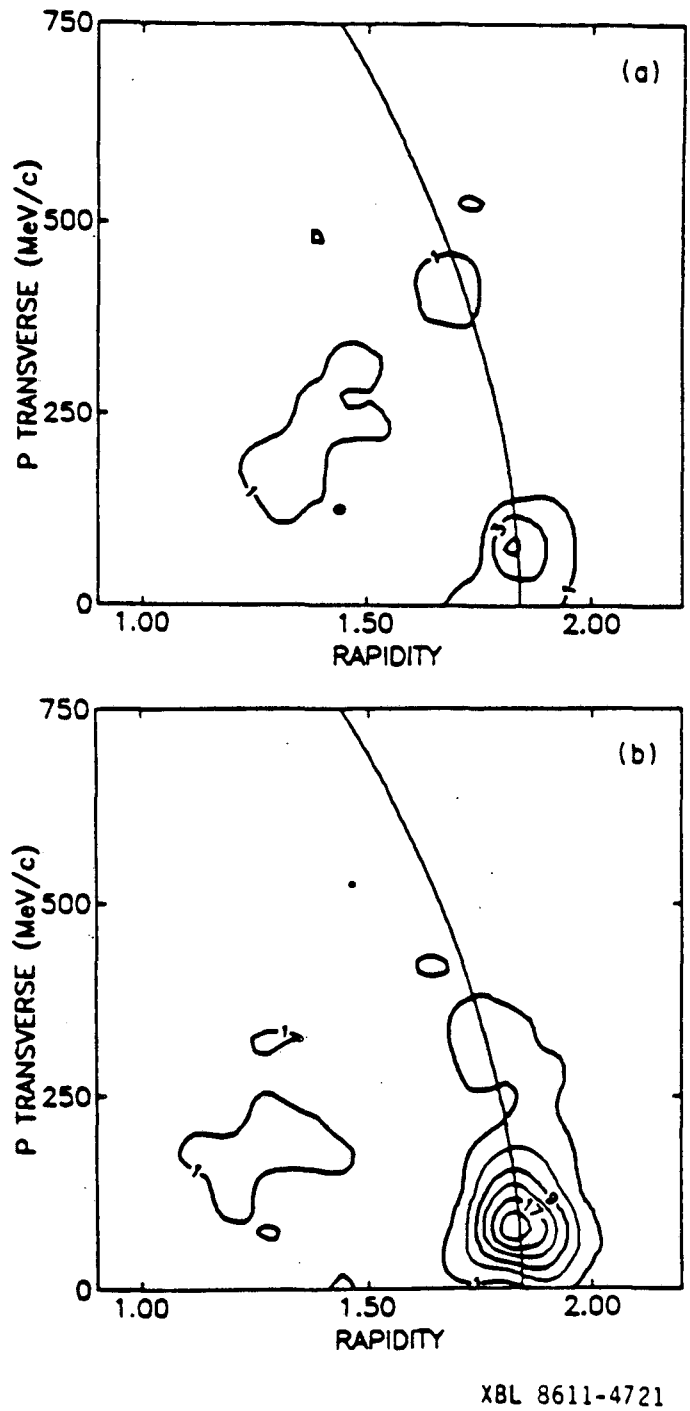

Figure 6.7: Rapidity versus transverse momentum for protons from the data with the Monte Carlo cascade model subtracted for (a) H and (b) C targets. The main features are: residual inelastic cross section in the low rapidity region and the low momentum transfer peaks. The contours are measured in units of 10^{-2}mb·rapidity^{-1}·(MeV/c)$^{-1}$.

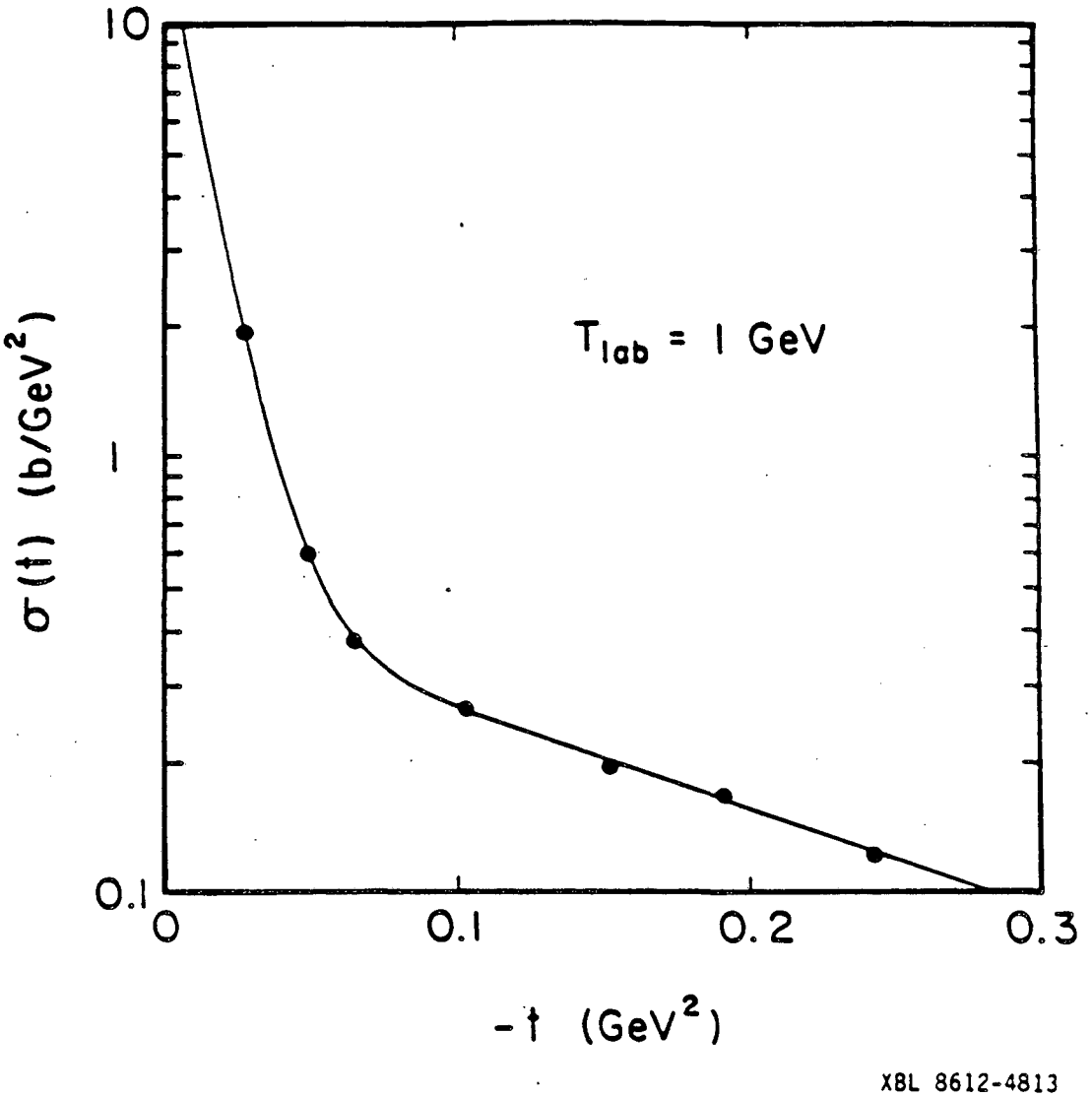

Figure 6.8: C(p,p)X cross section versus Mandelstam $-t$[50] at 1 GeV beam kinetic energy. The line, $\sigma(t) = 17.22e^{86t} + 0.44e^{5.2t}$, is a fit to the data points.

a process to occur in our case we follow the argument of Good and Walker[53]. Since the time of the interaction is short, the ^{12}C ground state and the low excitation energy ^{11}B+p states are essentially degenerate in energy. Thus it is possible for the proton to diffract elastically off the target, while the ^{11}B is not affected. The cross section for this diffractive process has been calculated to be 10 %[54] of the ^{12}C(^{16}O,^{15}O+x)X reaction at 2 GeV/nucleon.

To compare the p-nucleus data to our data, we show the proton cross section from the C target (Figure 6.9a) as a function of the previously defined modified Mandelstam t. Both diffractive peaks can be fit by e^{86t}. However our peak is 29 % or 4.50 $\pm$ 0.67 mb of the 15.6 $\pm$ 2.5 mb cross section excluding particle production, whereas the p-nucleus peak is 70 % or 200 mb of the 285 mb cross section. This comparison ignores the Pauli blocking of low momentum transfers to ^{12}C projectile nucleons. We must remove the same low momentum transfers from the (p,p) cross section for a valid comparison. To achieve the same 29 % ratio as the (^{12}C,^{11}B+p) cross section we use only the (p,p) cross section with $|t| < 0.022\,\mathrm{GeV}^2$. This reduces the (p,p) peak to 30.6 mb of the remaining 106 mb cross section, and is equivalent to requiring that the scattered proton have a kinetic energy of at least 11.6 MeV in the projectile frame. This value was expected to equal 15.96 MeV, the Q value of the (^{12}C,^{11}B+p) reaction.

Finally we show the proton cross section for an H target(Figure 6.9b). Here, if the proton were independent, we would expect to see only an $e^{5.2t}$ compo-

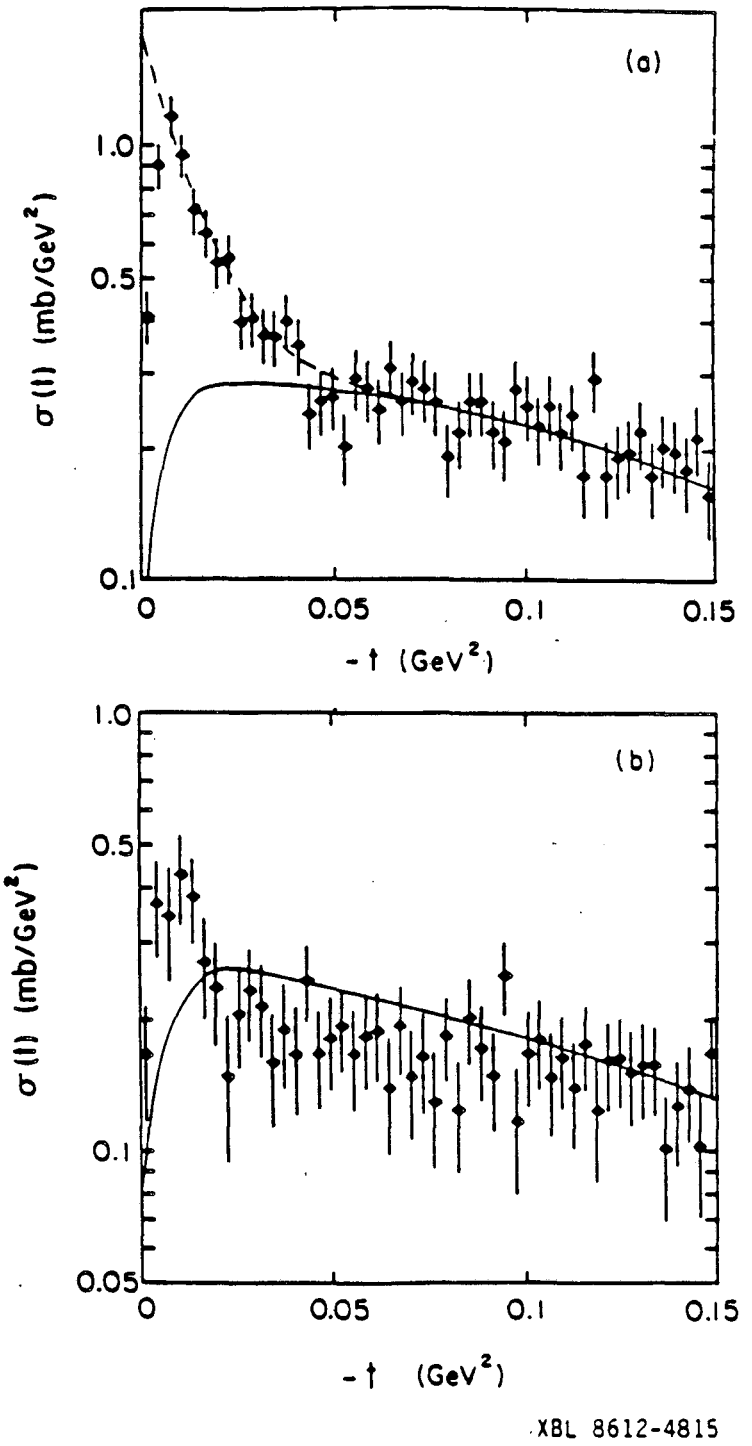

Figure 6.9: Data cross section versus modified $-t$ for (a) C and (b) H targets. The solid lines are natural spline fits to the normalized Monte Carlo cascade model. The dashed line shows the effect of adding an e^{36t} component to the Monte Carlo cascade model results.

nent. Instead there is an additional small peak which can not be fit by e^{86t}. So, while diffractive scattering can explain the C target low momentum transfer peak another mechanism is needed for the H target.

Such a mechanism could be excitation and decay via proton emission of the ^{12}C projectile, as in the nuclear Weiszäcker-Williams model[18] of Feshbach and Zabek. In this model the strong force "fringing field" of the target generates a "phonon" that is absorbed by the projectile which subsequently decays by emitting a nucleon pair to preserve momentum and energy balance. In our case the ^{12}C projectile decays into a proton and a ^{11}B. In this prescription the momenta of the proton and the ^{11}B are expected to be anticorrelated in the projectile rest frame(Figure 6.10a). The data (Figure 6.10b) show no obvious trend. The largest energy γ known to be emitted from an excited ^{11}B is 26.5 MeV[55] and would not materially effect the anticorrelation.

The momentum transferred to the projectile has to be small compared with the separation momenta of the decay fragments or the anticorrelation is not observable. In the nuclear Weiszäcker-Williams model, energy transfers under 20 MeV would show no anticorrelation in our experiment. Perhaps the ^{11}B cannot survive intact at these energy transfers, making the model inapplicable here. However the anticorrelation should be visible in the (^{12}C,p+p+^{10}Be) reaction and it is not seen[56].

It should be noted that other forms of excitation and decay have not been

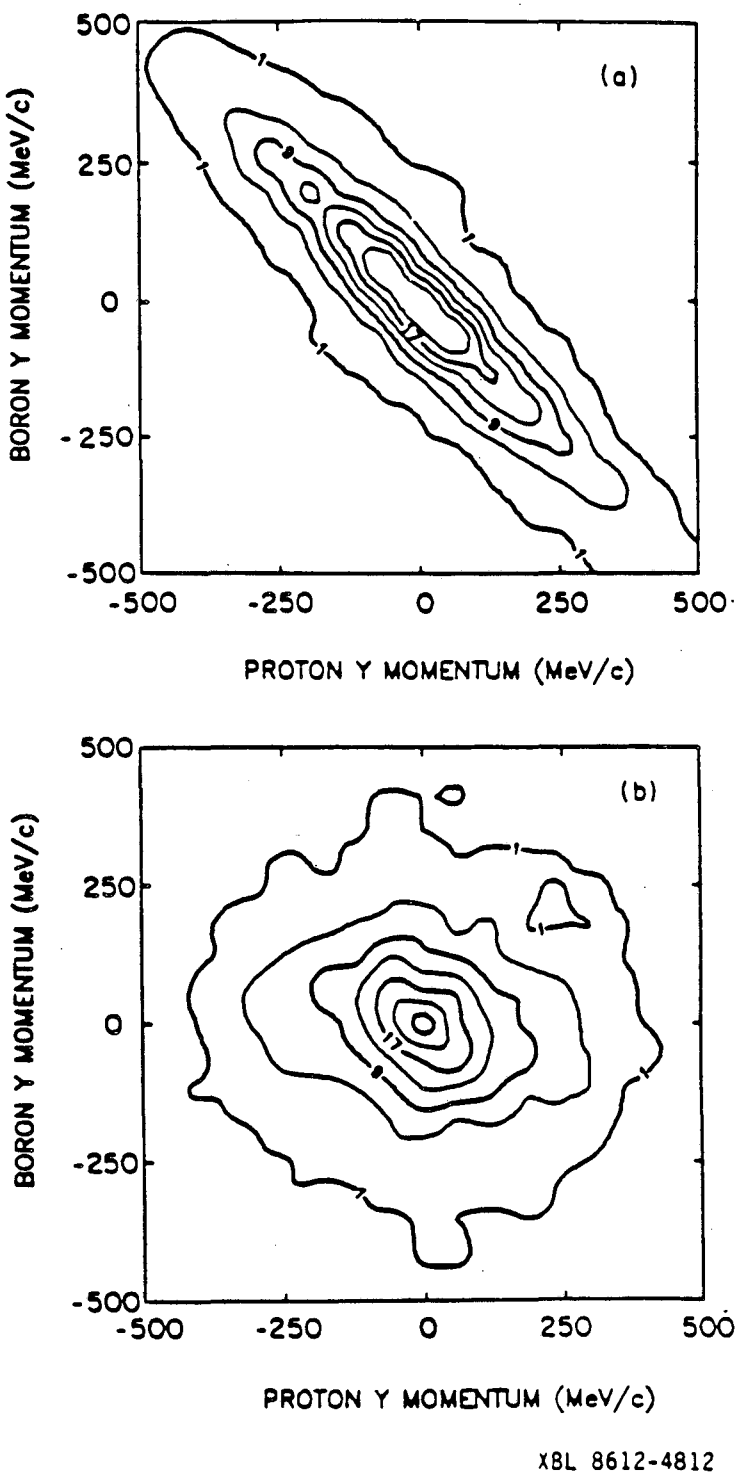

Figure 6.10: Perpendicular momenta, ^{11}B versus proton, parallel to the dipole field to maximize resolution. (a) Nuclear Weiszäcker-Williams model. (b) Carbon target. The contours are measured in units of 10^{-5}mb$\cdot$(MeV/c)$^{-2}$.

ruled out, if they are associated with momentum transfers larger than that of the nuclear Weiszäcker-Williams model. Presumably, the 0.81 ± 0.45 mb peak in the H target data is due to such an excitation and decay. If this scales as the sum of the radii[15], then the 4.50 ± 0.67 mb peak in the C target is $27 \pm 16\,\%$ excitation and decay and $73 \pm 16\,\%$ diffractive scattering. This would make the Pauli blocking kinetic energy 14.4 MeV, considerably closer to the 15.96 MeV Q value it is expected to equal.

Chapter 7

Conclusion

We find that the direct step of a peripheral relativistic heavy ion collision involves at least four mechanisms: (1) quasi-elastic nucleon-nucleon scattering, (2) inelastic nucleon-nucleon scattering with π production, (3) diffractive scattering, and (4) excitation and decay. The cross sections for the (^{12}C,^{11}B+p) reaction are 19.7 ± 3.4 mb for the H target and 39.7 ± 4.5 mb for the C target.

The free nucleon-nucleon prediction of the cascade model for quasi-elastic scattering between projectile and target nucleons is significantly different from the data. Although the model reproduces the shape of the data spectra we must multiply its cross section by 0.34 to obtain agreement. This suppression of the quasi-elastic component shows clearly that the cascade model is not a valid microscopic description of the interaction process. Also, a Fermi momentum of 190 MeV is needed. This reproduces the longitudinal momentum distribution of the proton spectra. However the transverse momentum distribution of the ^{11}B implies a Fermi momentum of 160 MeV. This discrepancy indicates that the

usual assumption of the nucleus being a free Fermi gas of nucleons is inappropriate in this reaction. It has been suggested[47] that this discrepancy is due to the peripheral nature of the reaction, but no quantitative predictions have been made. The cross sections for the quasi-elastic component are 8.8 ± 2.5 mb for the H(^{12}C,^{11}B+p)X reaction and 11.1 ± 2.4 mb for the C(^{12}C,^{11}B+p)X reaction.

The free nucleon-nucleon prediction of the cascade model for the π production process does not reproduce the shape of spectra. However the cross section predicted for this inelastic process is much closer than the factor of three in the quasi-elastic fit. This inelastic component of the cascade model had to be multiplied by 0.70 for the H target data and by 0.95 for the C target data. Since the cross section shapes of the data and the model are different for this process, a comparison shows that the data has residual unexplained cross section at high rapidity loss, indicating that other more highly inelastic processes must contribute to the inelastic region. The cross sections for this inelastic component are 10.1 ± 2.2 mb for the H(^{12}C,^{11}B+p)X reaction, and 24.1 ± 3.7 mb for the C(^{12}C,^{11}B+p)X reaction.

Diffractive scattering and excitation and decay are not independently resolvable for the C target since both produce a peak at low momentum and energy transfer. Excitation and decay is 0.81 ± 0.45 mb of 19.7 ± 3.4 mb in the H(^{12}C,^{11}B+p)X reaction. Assuming the process scales as the sum of the projectile and target radii, it is 1.21 ± 0.68 mb of the C(^{12}C,^{11}B+p)X reaction. This

leaves 3.29 ± 0.96 mb of the reaction due to a proton in the ^{12}C projectile scattering diffractively from the C target.

Appendix A

Relativistic Kinematics[58]

At a kinetic energy of 2.1 GeV/nucleon the velocity of the projectile in the laboratory frame is 0.95c. Thus, relativistic effects become important. It is useful to perform data analysis in terms of relativistic invariants, because such analysis is independent of the Lorentz frame chosen. It is then possible to easily calculate these invariants in any Lorentz frame, and to conceptualize each invariant in that particular Lorentz frame that makes comprehension easiest.

The energy, E, and three-momentum, $\vec{p}$, of a particle form a four-vector, $p = (E, \vec{p})$. It is useful to express the velocity, $\vec{v}$, as a fraction, $\vec{\beta} \equiv \vec{v}/c$, of the speed of light, c. If we adopt units where $c = 1$ then viewed from a second frame with a velocity $\beta\hat{z}$ relative to the original frame, the components of p are Lorentz transformed to

$$\begin{aligned} E' &= \gamma E - \beta\gamma p_z, \\ p'_z &= \gamma p_z - \beta\gamma E, \end{aligned}$$

$$p'_x = p_x,$$

$$p'_y = p_y,$$

where $\gamma = (1-\beta^2)^{-1/2}$. From this it follows that the scalar product of two four-momenta, $p_1 \cdot p_2 \equiv E_1 E_2 - \vec{p_1} \cdot \vec{p_2}$, is invariant, that is, the same value in all Lorentz frames. This is a property of all four-vectors.

The relativistic kinematics needed for our analysis can most easily be understood from the viewpoint of two body scattering (Figure A.1). Ostensibly there are 16 parameters, but various symmetries reduce them to 6. Translational and rotational invariance each remove 3 degrees of freedom, and conservation of four-momentum removes 4 more. Typically, four of the parameters used to characterize a two body scatter are the 4 rest masses, m_i, which can be derived from the invariants $p_i^2 = E_i^2 - \vec{p_i}^2 = m_i^2$. In non-relativistic cases the other 2 parameters are usually scattering angle and energy. In our case it is more convenient to use 2 more invariants, E_{cm} and t.

These last 2 parameters are derived from the Mandelstam invariants,

$$\begin{aligned} s &= (p_1 + p_2)^2 = (p_3 + p_4)^2 \\ &= (E_1 + E_2)^2 - (\vec{p_1} + \vec{p_2})^2, \\ t &= (p_1 - p_3)^2 = (p_2 - p_4)^2 \\ &= (E_1 - E_3)^2 - (\vec{p_1} - \vec{p_3})^2, \end{aligned}$$

$$\begin{aligned} u &= (p_1 - p_4)^2 = (p_2 - p_3)^2 \\ &= (E_1 - E_4)^2 - (\vec{p_1} - \vec{p_4})^2. \end{aligned}$$

These variables satisfy

$$s + t + u = m_1^2 + m_2^2 + m_3^2 + m_4^2.$$

In the center of mass frame, where $\vec{p_1} = -\vec{p_2}$, it is easy to see that the total center of mass energy $E_{cm} = \sqrt{s}$. In the frame where $E_1 = E_3$, which is the center of mass frame for elastic collisions, t is the square of the momentum transfer. More formally, using $p_{cm} = |\vec{p_{cm}}|$,

$$t = (E_{1cm} - E_{3cm})^2 - (p_{1cm} - p_{3cm})^2 - 4p_{1cm}p_{3cm}\sin^2\left(\frac{\theta_{cm}}{2}\right),$$

where θ_{cm} is the center of mass scattering angle. For $\theta_{cm} = 0$, $-t$ is at a minimum. The third Mandelstam variable, u, is conjugate to t and is included here for completeness.

The cross section as a function of t can be expressed simply in terms of the Lorentz invariant scattering matrix, $\mathcal{M}$, as follows:

$$\sigma(t) = \frac{1}{64\pi s}\frac{|\mathcal{M}|^2}{p_{1cm}^2}.$$

The connection to the cross section as a function of center of mass scattering angle is also simple :

$$\sigma(\theta_{cm}) = \frac{p_{1cm}p_{3cm}}{\pi}\sigma(t).$$

When examining cross sections as functions of two variables it is convenient to use the variables $p_\perp$ and y. Transverse momentum, $p_\perp = (p_x^2 + p_y^2)^{1/2}$, is invariant under a Lorentz transformation in the $\hat{z}$ direction. The rapidity,

$$y = \frac{1}{2}\ln\left[\frac{E+p_z}{E-p_z}\right] = \tanh^{-1}\left[\frac{p_z}{E}\right],$$

is additive under a Lorentz transformation in the $\hat{z}$ direction. That is, $y' = y + \delta$ where $\tanh\delta = \beta$. The shape of this cross section, $\sigma(y, p_\perp)$, is invariant under this Lorentz transformation. In terms of laboratory parameters

$$\frac{1}{\pi}\sigma(y, p_\perp) = \frac{E_{lab}}{p_{lab}^2}\sigma(p_{lab}, \Omega_{lab}).$$

Finally, for the process where the ^{12}C projectile is excited and then decays into a ^{11}B and a proton, we can express the ^{12}C excitation energy, E^*, in terms of relativistic invariants:

$$E^* = M^* - m_C = |p_1 + p_2| - m_C.$$

The invariant mass, M^*, of the ^{11}B and proton is found from

$$(M^*)^2 = (p_1 + p_2)^2,$$

where p_1 and p_2 are the four-momenta of the ^{11}B and proton. In the rest frame of the excited ^{12}C, where $\vec{p_1} = -\vec{p_2}$, it is evident that the invariant mass M^* is the total energy of the excited ^{12}C. After subtracting the ^{12}C rest mass, m_C, we have the excitation energy expressed in relativistic invariants.

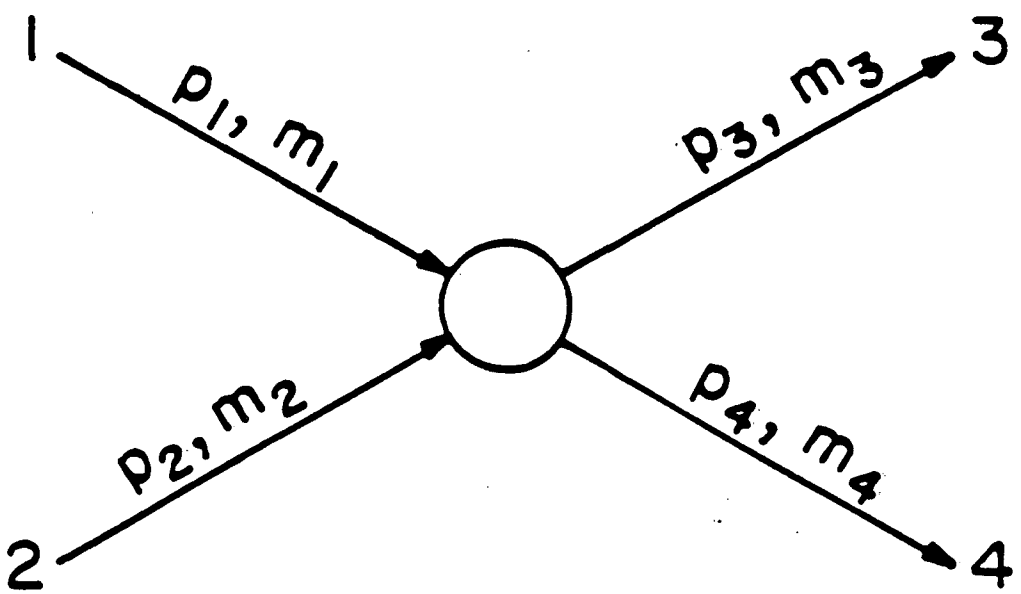

Figure A.1: Two body scattering. Typically, particle 1 is the projectile and particle 2 is the target before scattering. After scattering particle 3 is detected and particle 4 is the residual.

Appendix B

Isospin Corrections[57]

The predominant reaction mechanism of the inelastic NN interaction is Δ production with the subsequent decay of the Δ via π emission. Let σ_Δ designate the $NN \rightarrow \Delta N$, and $NN \rightarrow N\Delta$ production cross sections. The cross section for $NN \rightarrow \Delta N \rightarrow (N\pi)N$, where the parentheses contain the Δ decay products, involves Clebsch-Gordon coefficients as follows:

$$\begin{aligned}
\sigma\left(NN \rightarrow (N\pi)\,N\right) &= \sigma\left(NN \rightarrow N\left(\pi N\right)\right) \\
&\propto \left|\left\langle \pi\left(1, T_z'\right) N\left(\frac{1}{2}, \tau_z'\right) \middle| \Delta\left(\frac{3}{2}, \bar{T}_z\right)\right\rangle\right. \\
&\quad \times \left\langle N\left(\frac{1}{2}, \tau_z\right) \Delta\left(\frac{3}{2}, \bar{T}_z\right) \middle| NN\left(T, T_z\right)\right\rangle \\
&\quad \times \left.\left\langle NN\left(T, T_z\right) \middle| N\left(\frac{1}{2}, t_z\right) N\left(\frac{1}{2}, t_z'\right)\right\rangle\right|^2 \sigma_\Delta,
\end{aligned}$$

where t_z, t_z' are the isospin projections for the initial state nucleons, T, T_z are the total isospin of the NN system, τ_z, τ_z' are the isospin projections for the final state nucleons, and $\bar{T}_z, T_z'$ are the isospin projections of the Δ and π.

For the H(^{12}C,^{11}B+p)X reaction the inelastic nucleon-nucleon interactions of

interest are $pp \rightarrow \Delta N \rightarrow (p\pi)N$ and $pp \rightarrow p\Delta \rightarrow p(\pi N)$. The first reaction, projectile Δ production, produces a projectile proton 11/12 of the time, while the second reaction, target Δ production, produces a projectile proton 1/4 of the time (Table B.1).

For the C target 3/8 of the proton-nucleon collisions resulting in a target Δ leave a proton in the projectile, while 17/24 of the projectile Δ's decay into a proton. Also quasi-elastic charge exchange is $2.86 \pm 0.65\,\%$[32] of quasi-elastic scattering from the C target. The cross sections have been normalized to total fragmentation cross sections of 250 ± 10 mb for a H target and 810 ± 20 mb for a C target[45].

Table B.1: Isobar model cross sections for $NN \rightarrow N\pi N$.

Pion Production Cross Sections			
Projectile Δ		Target Δ	
Reaction	Isobar Model	Reaction	Isobar Model
$\sigma\,[pp \rightarrow (p\pi^+)\,n]$	$\frac{3}{4}\sigma_\Delta$	$\sigma\,[pp \rightarrow n\,(\pi^+p)]$	$\frac{3}{4}\sigma_\Delta$
$\sigma\,[pp \rightarrow (p\pi^\circ)\,p]$	$\frac{1}{6}\sigma_\Delta$	$\sigma\,[pp \rightarrow p\,(\pi^\circ p)]$	$\frac{1}{6}\sigma_\Delta$
$\sigma\,[pp \rightarrow (n\pi^+)\,p]$	$\frac{1}{12}\sigma_\Delta$	$\sigma\,[pp \rightarrow p\,(\pi^+n)]$	$\frac{1}{12}\sigma_\Delta$
$\sigma\,[pp \rightarrow (n\pi)\,N]$	$\frac{1}{12}\sigma_\Delta$	$\sigma\,[pp \rightarrow n\,(\pi N)]$	$\frac{3}{4}\sigma_\Delta$
$\sigma\,[pp \rightarrow (p\pi)\,N]$	$\frac{11}{12}\sigma_\Delta$	$\sigma\,[pp \rightarrow p\,(\pi N)]$	$\frac{1}{4}\sigma_\Delta$
$\sigma\,[pn \rightarrow (p\pi^-)\,p]$	$\frac{1}{3}\sigma_\Delta$	$\sigma\,[pn \rightarrow p\,(\pi^-p)]$	$\frac{1}{3}\sigma_\Delta$
$\sigma\,[pn \rightarrow (p\pi^\circ)\,n]$	$\frac{1}{6}\sigma_\Delta$	$\sigma\,[pn \rightarrow n\,(\pi^\circ p)]$	$\frac{1}{6}\sigma_\Delta$
$\sigma\,[pn \rightarrow (n\pi^+)\,n]$	$\frac{1}{3}\sigma_\Delta$	$\sigma\,[pn \rightarrow n\,(\pi^+n)]$	$\frac{1}{3}\sigma_\Delta$
$\sigma\,[pn \rightarrow (n\pi^\circ)\,p]$	$\frac{1}{6}\sigma_\Delta$	$\sigma\,[pn \rightarrow p\,(\pi^\circ n)]$	$\frac{1}{6}\sigma_\Delta$
$\sigma\,[pn \rightarrow (n\pi)\,N]$	$\frac{1}{2}\sigma_\Delta$	$\sigma\,[pn \rightarrow n\,(\pi N)]$	$\frac{1}{2}\sigma_\Delta$
$\sigma\,[pn \rightarrow (p\pi)\,N]$	$\frac{1}{2}\sigma_\Delta$	$\sigma\,[pn \rightarrow p\,(\pi N)]$	$\frac{1}{2}\sigma_\Delta$
$\sigma\,[pN \rightarrow (n\pi)\,N]$	$\frac{7}{24}\sigma_\Delta$	$\sigma\,[pN \rightarrow n\,(\pi N)]$	$\frac{5}{8}\sigma_\Delta$
$\sigma\,[pN \rightarrow (p\pi)\,N]$	$\frac{17}{24}\sigma_\Delta$	$\sigma\,[pN \rightarrow p\,(\pi N)]$	$\frac{3}{8}\sigma_\Delta$

Bibliography

[1] P. Freier, E. J. Lofgren, E. P. Ney, F. Oppenheimer, H. L. Bradt, and B. Peters, *Physical Review* **74**, 213 (1948).

P. Freier, E. J. Lofgren, E. P. Ney, F. Oppenheimer, *Physical Review* **74**, 1818 (1948).

[2] H. L. Bradt and B. Peters, *Physical Review* **74**, 1828 (1948).

H. L. Bradt and B. Peters, *Physical Review* **77**, 54 (1950).

H. L. Bradt and B. Peters, *Physical Review* **80**, 943 (1950).

M. F. Kaplon, B. Peters, H. L. Reynolds, and D. M. Ritson, *Physical Review* **85**, 295 (1952).

[3] H. L. Bradt and B. Peters, *Physical Review* **75**, 1779 (1949).

[4] Y. Eisenberg, *Physical Review* **96**, 1378 (1954).

[5] E. M. Friedlander and H. H. Heckman, *Treatise on Heavy-Ion Science* **4**, D. A. Bromley ed., 403 (Plenum Press, New York 1985).

[6] R. Serber, *Physical Review* **72**, 1114 (1947).

J. D. Bowman, W. J. Swiatecki, and C. F. Tsang, *Lawrence Berkeley Laboratory Report* **LBL-2908** (1973).

[7] D. J. Morrissey, W. R. Marsh, R. J. Otto, W. Loveland, and G. T. Seaborg, *Physical Review C* **18**, 1267 (1978).

L. F. Oliveira, R. Donangelo, and J. O. Rasmussen, *Physical Review C* **19**, 826 (1979).

[8] A. S. Goldhaber and H. H. Heckman, *Annual Review of Nuclear Science* **28**, 161 (1978).

[9] M. G. White, M. Isaila, K. Prelec, and H. L. Allen, *Science* **174**, 1121 (1971).

[10] H. A. Grunder, W. D. Hartsough and E. J. Lofgren, *Science* **174**, 1128 (1971).

[11] S. Nagamiya and M. Gyulassy, *Advances in Nuclear Physics* **13**, 201 (1984).

S. Nagamiya, J. Randrup and T. J. M. Symons, *Annual Review of Nuclear and Particle Science* **34**, 155 (1984).

J. Hüfner *Physics Reports* **125**, 129 (1985).

[12] J. A. Maruhn and W. Greiner, *Treatise on Heavy-Ion Science* **4**, D. A. Bromley ed., 565 (Plenum Press, New York 1985).

[13] S. Nagamiya, M. C. Lemaire, E. Moeller, S. Schnetzer, G. Shapiro, et al., *Physical Review C* **24**, 971 (1981).

[14] J. Papp, J. Jaros, L. Schroeder, J. Staples, H. Steiner, A. Wagner and J. Wiss, *Physical Review Letters* **34**, 601 (1975).

J. Papp, *Thesis, Lawrence Berkeley Laboratory Report* **LBL-3633** (1975).

H. H. Heckman and P. J. Lindstrom, *Physical Review Letters* **37**, 56 (1976).

L. Anderson, *Thesis, Lawrence Berkeley Laboratory Report* **LBL-6767** (1977).

M. M. Gazzaly, J. B. Carroll, J. V. Geaga, G. Igo, J. B. McClelland, M. A. Nasser and H. Spinka, *Physics Letters* **79B**, 325 (1978).

S. Nagamiya, M. -C. Lemaire, S. Schnetzer, H. Steiner and I. Tanihata, *Physical Review Letters* **45**, 602 (1980).

R. Stock, H. H. Gutbrod, W. G. Meyer, A. M. Poskanzer, A. Sandoval, J. Gosset, C. H. King, G. King, Ch. Lukner, Nguyen Van Sen, G. D. Westfall and K. L. Wolf, *Physical Review Letters* **44**, 1243 (1980).

I. Tanihata, M. -C. Lemaire, S. Nagamiya and S. Schnetzer, *Physics Letters* **97B**, 363 (1980).

I. Tanihata, S. Nagamiya, S. Schnetzer and H. Steiner, *Physics Letters* **100B**, 121 (1981).

Z. Zarbakhsh, A. L. Sagle, F. Brochard, T. A. Mulera, V. Perez-Mendez, R. Talaga and I. Tanihata, *Physical Review Letters* **46**, 1268 (1981).

L. M. Anderson, Jr., W. Brückner, E. Moeller, S. Nagamiya, S. Nissen-Meyer, L. Schroeder, G. Shapiro and H. Steiner, *Lawrence Berkeley Laboratory Report* **LBL-14328** (1982).

L. Anderson, W. Brückner, E. Moeller, S. Nagamiya, S. Nissen-Meyer, L. Schroeder, G. Shapiro and H. Steiner, *Physical Review C* **28**, 1224 (1983).

[15] P. J. Lindstrom, D. E. Greiner, H. H. Heckman, Bruce Cork and F. S. Bieser, *Lawrence Berkeley Laboratory Report* **LBL-3650** (1975).

D. L. Olson, B. L. Berman, D. E. Greiner, H. H. Heckman, P. J. Lindstrom and H. J. Crawford, *Physical Review C* **28**, 1602 (1983).

[16] D. E. Greiner, P. J. Lindstrom, H. H. Heckman, Bruce cork and F. S. Bieser, *Physical Review Letters* **35**, 152 (1974).

J. Engelage, H. J. Crawford, I. Flores, O. Hashimoto, S. Nagamiya, I Tanihata, M. E. Baumgartner, E. Beleal, F. Bieser, M. Bronson, D. E. Greiner, L. Greiner, P. J. Lindstrom, C. McParland, R. Wada, B. Berman, D. L. Olson, P. N. Kirk, C. L. Ruiz, F. P. Brady, J. L. Romero, M. L. Webb, *Nuclear Instruments and Methods in Physics Research*, to be submitted.

[17] J. Hüfner, K. Schäfer and B. Schürmann, *Physical Review C* **12**, 1888 (1975).

[18] H. Feshbach and M. Zabek, *Annals of Physics* **107**, 110 (1977).

H. Feshbach, *Progress in Particle and Nuclear Physics* **4**, 451 (1980).

[19] J. Cugnon, *Physical Review C* **22**, 1885 (1980).

J. Cugnon, T. Mizutani, and J. Vandermeulen, *Lettere al Nuovo Cimento* **28**, 55 (1980).

J. Cugnon, T. Mizutani, and J. Vandermeulen, *Nuclear Physics* **A352**, 505 (1980).

[20] J. Engelage, M. Baumgartner, D. E. Greiner, P. J. Lindstrom, D. L. Olson, R. Wada, H. J. Crawford and M. L. Webb, *Physics Letters B* **173**, 34 (1986).

[21] G. M. Chernov, K. G. Gulamov, U. G. Gulyamov, S. Z. Nasyrov and L. N. Svechnikova, *Nuclear Physics* **A280**, 478 (1977).

H. H. Heckman, H. J. Crawford, D. E. Greiner, P. J. Lindstrom and Lance W. Wilson, *Physical Review C* **17**, 1651 (1978).

H. H. Heckman, D. E. Greiner, P. J. Lindstrom and H. Shwe, *Physical Review C* **17**, 1735 (1978).

B. Jacobsson, *Physica Scripta* **17**, 491 (1978).

[22] A. Sandoval, R. Bock, R. Brockman, A. Dacal, J. W. Harris, M. Maier, M. E. Ortiz, H. G. Pugh, W. Rauch, R. E. Renfordt, L. S. Schroeder, R. Stock, H. Ströbele and K. L. Wolf, *Nuclear Physics* **A400** 365 (1983).

[23] H. J. Crawford, *Lecture Notes in Physics* **178**, 92 (1983).

D. E. Greiner, *Nuclear Physics* **A400**, 325c (1983).

[24] G. D. Westfall, J. Gosset, P. J. Johansen, A. M. Poskanzer, W. G. Meyer, H. H. Gutbrod, A. Sandoval, and R. Stock, *Physical Review Letters* **37**, 1202 (1976).

J. Gosset, H. H. Gutbrod, W. G. Meyer, A. M. Poskanzer, A. Sandoval, R. Stock, and G. D. Westfall, *Physical Review C* **16**, 629 (1977).

G. Mantzouranis, *Physical Review C* **18**, 2227 (1978).

[25] W. D. Myers, *Nuclear Physics* **A296**, 177 (1978).

[26] A. A. Amsden, G. F. Bertsch, F. H. Harlow, and J. R. Nix, *Physical Review Letters* **35**, 905 (1975).

F. H. Harlow, A. A. Amsden, and J. R. Nix, *Journal of Computational Physics* **20**, 119 (1976).

A. A. Amsden, F. H. Harlow, and J. R. Nix, *Physical Review C* **15**, 2059 (1977).

A. A. Amsden, A. S. Goldhaber, F. H. Harlow, and J. R. Nix, *Physical Review C* **17**, 2080 (1978).

P. Danielewicz, *Nuclear Physics* **A314**, 465 (1979).

J. R. Nix, A. J. Sierk, and D. J. Strottmann, *Los Alamos National Laboratory Report* **La-UR-80-1280**, (1980).

A. J. Sierk and J. R. Nix, *Los Alamos National Laboratory Report* **La-UR-80-1909**, (1980).

J. R. Nix and D. J. Strottmann, *Physical Review C* **23**, 2548 (1981).

[27] H. Stöcker, W. Greiner, and W. Scheid, *Zeitschrift für Physik A Atoms and Nuclei* **286**, 121 (1978).

H. Stöcker, J. A. Maruhn, and W. Greiner, *Zeitschrift für Physik A Atoms and Nuclei* **290**, 297 (1979).

H. Stöcker, J. A. Maruhn, and W. Greiner, *Zeitschrift für Physik A Atoms and Nuclei* **293**, 173 (1979).

H. Stöcker, J. A. Maruhn, and W. Greiner, *Physics Letters* **81B**, 303 (1979).

H. Stöcker, R. Y. Cusson, J. A. Maruhn, and W. Greiner, *Zeitschrift für Physik A Atoms and Nuclei* **294**, 125 (1980).

H. Stöcker, G. Graebner, J. A. Maruhn, and W. Greiner, *Zeitschrift für Physik A Atoms and Nuclei* **295**, 401 (1980).

H. Stöcker, J. Hofmann, J. A. Maruhn, and W. Greiner, *Progress in Particle and Nuclear Physics* **4**, 133 (1980).

H. Stöcker, G. Graebner, J. A. Maruhn, and W. Greiner, *Physics Letters* **95B**, 192 (1980).

G. Buchwald, L. P. Csernai, G. Graebner, J. A. Maruhn, W. Greiner, and H. Stöcker, *University of Frankfurt Report* **UFTP 53/1981**, (1981).

G. Buchwald, L. P. Csernai, G. Graebner, J. A. Maruhn, W. Greiner, and H. Stöcker, *Physical Review C* **24**, 135 (1981).

[28] H. Stöcker, J. A. Maruhn, and W. Greiner, *Physical Review Letters* **44**, 725 (1980).

[29] A. A. Amsden, *Los Alamos Scientific Laboratory Report* **LA-3466**, (1966).

[30] J. P. Boris and D. L. Brook, *Journal of Computational Physics* **11**, 38 (1973).

[31] K. Chen, Z. Fraenkel, G. Friedlander, J. R. Grover, J. M. Miller, and Y. Shimamoto, *Physical Review* **166**, 949 (1968).

Y. Yariv and Z. Fraenkel, *Physical Review C 20*, 2227 (1979).

Y. Yariv and Z. Fraenkel, *Weizmann Institute Preprint* **WIS-79/15-Ph**, (1979).

Y. Yariv and Z. Fraenkel, *Weizmann Institute Preprint* **WIS 18/80**, (1980).

[32] Particle Data Group, *Lawrence Berkeley Laboratory Report* **UCRL-20000 NN** (1970).

[33] V. K. Lukyanov and A. I. Titov, *Physics Letters* **57**, 10 (1975).

[34] J. D. Jackson, *Classical Electrodynamics* 2nd ed., 719, (Wiley, New York 1975).

R. Jäckle and H. Pilkuhn, *Nuclear Physics* **A247**, 521 (1975).

X. Artru and G. B. Yodh, *Physics Letters* **40B**, 43, (1972).

[35] D. L. Olson, B. L. Berman, D. E. Greiner, H. H. Heckman, P. J. Lindstrom, G. D. Westfall, and H. J. Crawford, *Physical Review C* **24**, 1529 (1981).

[36] H. H. Heckman and Peter J. Lindstrom, *Physical Review Letters* **37**, 56, (1976).

[37] *Bevatron/Bevalac User's Handbook, Lawrence Berkeley Laboratory Report* **PUB-101** (1980).

[38] R. C. Wolgast et al., *Lawrence Berkeley Laboratory Report* **LBL-11579** (1980).

[39] J. Porter, *private communication.*

[40] F. Bieser and C. McParland, *Lawrence Berkeley Laboratory Report* **LBL-13366** 220, (1982).

[41] C. McParland, *IEEE Transactions on Nuclear Science* **NS-30** 3953, (1983).

[42] H. J. Crawford and P. J. Lindstrom, *IEEE Transactions on Nuclear Science* **NS-30** 3842, (1983).

[43] P. J. Lindstrom, *private communication.*

[44] J. W. Harris, *personal communication.*

[45] P. J. Lindstrom, D. E. Greiner, H. H. Heckman, Bruce Cork and F. S. Bieser, *14th International Cosmic Ray Conference* **7**, 2315 (1975).

[46] E. J. Moniz, I. Sick, R. R. Whitney, J. R. Ficenec, R. D. Kephart and W. P. Trower, *Physical Review Letters* **26**, 445 (1971).

[47] W. A. Friedman, *Physical Review C* **27**, 569 (1983).

[48] J. V. Lepore and R. J. Riddell, Jr., *Lawrence Berkeley Laboratory Report* **LBL-3086** (1973).

[49] A. S. Goldhaber, *Physics Letters* **53B**, 306 (1974).

[50] J. L. Friedes, H. Palevsky, R. J. Sutter, G. W. Bennett, G. J. Igo, W. D. Simpson and D. M. Corley, *Nuclear Physics* **A104**, 294 (1967). Original measurement.
W. Czyż, L. Leśniak and H. Wołek, *Nuclear Physics* **B19**, 125 (1970). Data plotted in more convenient form.

[51] K. Goulianos, *Physics Reports* **101**, 169 (1983).

[52] W. Czyż, *Advances in Nuclear Physics* **4**, 61 (1971).

[53] M. L. Good and W. D. Walker, *Physical Review* **120**, 1857 (1960).

[54] J. Hüfner and M. C. Nemes, *Physical Review C* **23**, 2538 (1981).
B. Hiller and J. Hüfner, *Nuclear Physics* **A382** 542 (1982).

[55] F. Ajzenberg-Selove and C. L. Busch, *Nuclear Physics* **A336**, 1 (1980).

[56] H. J. Crawford, *personal communication.*

[57] S. J. Wallace, *Advances in Nuclear Physics* **12**, 135 (1981).

[58] M. Aguilar-Benitez, F. C. Porter, J. J. Hernandez, L. Montanet, R. L. Crawford, K. R. Schubert, M. Roos, N. A. Törnqvist, G. Höhler, R. M. Barnett, I. Hinchliffe, G. R. Lynch, A. Rittenberg, T. G. Trippe, C. G. Wohl, G. P. Yost, B. Armstrong, G. S. Wagman, D. M. Manley, T. Shimada, G. P. Gopal, J. Primack, K. G. Hayes, R. H. Schindler, R. E. Shrock, R. A. Eichler, R. Frosch, L. D. Roper and W. P. Trower, *Physics Letters* **170B** 1, (1986).

LAWRENCE BERKELEY LABORATORY
TECHNICAL INFORMATION DEPARTMENT
UNIVERSITY OF CALIFORNIA
BERKELEY, CALIFORNIA 94720